ICES REPORT 12-15

April 2012

Isogeometric Divergence-conforming B-splines for the Steady Navier-Stokes Equations

by

John A. Evans and Thomas J.R. Hughes

The Institute for Computational Engineering and Sciences
The University of Texas at Austin
Austin, Texas 78712

Reference: John A. Evans and Thomas J.R. Hughes, Isogeometric Divergence-conforming B-splines for the Steady Navier-Stokes Equations, ICES REPORT 12-15, The Institute for Computational Engineering and Sciences, The University of Texas at Austin, April 2012.

Isogeometric Divergence-conforming B-splines for the Steady Navier-Stokes Equations

John A. Evans [a,*] and Thomas J.R. Hughes [a]

[a] *Institute for Computational Engineering and Sciences, The University of Texas at Austin,*

[*] Corresponding author. *E-mail address:* evans@ices.utexas.edu

Abstract

We develop divergence-conforming B-spline discretizations for the numerical solution of the steady Navier-Stokes equations. These discretizations are motivated by the recent theory of isogeometric discrete differential forms and may be interpreted as smooth generalizations of Raviart-Thomas elements. They are (at least) patch-wise C^0 and can be directly utilized in the Galerkin solution of steady Navier-Stokes flow for single-patch configurations. When applied to incompressible flows, these discretizations produce pointwise divergence-free velocity fields and hence exactly satisfy mass conservation. Consequently, discrete variational formulations employing the new discretization scheme are automatically momentum-conservative and energy-stable. In the presence of no-slip boundary conditions and multi-patch geometries, the discontinuous Galerkin framework is invoked to enforce tangential continuity without upsetting the conservation or stability properties of the method across patch boundaries. Furthermore, as no-slip boundary conditions are enforced weakly, the method automatically defaults to a compatible discretization of Euler flow in the limit of vanishing viscosity. The proposed discretizations are extended to general mapped geometries using divergence-preserving transformations. For sufficiently regular single-patch solutions subject to a smallness condition, we prove *a priori* error estimates which are optimal for the discrete velocity field and suboptimal, by one order, for the discrete pressure field. We present a comprehensive suite of numerical experiments which indicate optimal convergence rates for both the discrete velocity and pressure fields for general configurations, suggesting that our *a priori* estimates may be conservative. These numerical experiments also suggest our discretization methodology is robust with respect to Reynolds number and more accurate than classical numerical methods for the steady Navier-Stokes equations.

Keywords: Steady Navier-Stokes equations, B-splines, Isogeometric analysis, Divergence-conforming discretizations

1 Introduction

Steady Navier-Stokes flow is an important simplification of fully unsteady Navier-Stokes flow. Many low speed, laminar fluid flows may be accurately described by the steady Navier-Stokes equations. Additionally, one arrives at a steady Navier-Stokes problem by conducting a Reynolds time-averaging of statistically stationary Navier-Stokes flows (see Chapters 3 and 4 of [31]). Despite its simple appearance, the steady Navier-Stokes problem has presented considerable difficulty in its numerical approximation. It is subject to the Babuška-Brezzi inf-sup condition, and when the convection operator is expressed in conservation form and the incompressibility constraint is not met exactly, terms corresponding to convection can actually accrete energy. This ultimately leads to unstable numerical formulations, and alternative representations of the convection operator have been devised to bypass this instability. The most popular of these in the finite element community is the skew-symmetric representation [40]. Discretizations of the convection term using the skew-symmetric representation neither produce nor dissipate energy and hence lead to stable numerical methods. Unfortunately, these discretizations do not inherit the conservation structure of the Navier-Stokes equations. Alternatively, provably stable, convergent, and locally-conservative discontinuous Galerkin discretizations have been devised for the steady Navier-Stokes equations in [11, 12], but these discretizations are encumbered with a proliferation of degrees of freedom and are thus largely limited to two spatial dimensions. Hybrid technologies have recently been proposed with the aim of extending the applicability of discontinuous Galerkin methods to larger problem sizes [28, 29].

Another discretization procedure for the steady Navier-Stokes equations arises through the intelligent choice of weighting function in a Petrov-Galerkin method. A popular method of choice is the use of an advective formulation in conjunction with the Streamline-Upwind Petrov-Galerkin (SUPG) method [7] to handle convective instabilities and the Pressure-Stabilizing Petrov-Galerkin (PSPG) method [25, 37] to handle pressure instabilities. Unfortunately, the theoretical analysis of this method in the steady regime has been entirely restricted to linearized Oseen problems where the convection velocity is assumed fixed and divergence-free. These linearized model problems are ultimately insufficient as the discrete convection velocity is not, in general, divergence-free. To further control the divergence term, so-called grad-div stabilization techniques [33] have been proposed which add artificial dilatational stresses to the underlying variational formulation. Using a combination of an advective formulation, SUPG, PSPG, and grad-div stabilization, provably convergent numerical methods have been devised for the steady Navier-Stokes equations (see Chapter 3 of [33]), and such methods can be made to globally conserve momentum through a residual-based modification [26]. Still, a provably convergent $\mathbf{H}^1$-Galerkin finite element discretization of the three-dimensional steady Navier-Stokes equations written in conservation form has proved elusive.

In this paper, we present divergence-conforming B-spline discretizations for the steady Navier-Stokes problem. These discretizations are motivated by the theory of isogeometric discrete differential forms [9, 10] and extend the Darcy-Stokes-Brinkman discretizations presented in [19] to nonlinear Navier-Stokes flows. As our discretizations return pointwise divergence-free velocity fields, we can utilize a variational formulation written in conservation form without being susceptible to instability. We impose no-penetration boundary conditions strongly and no-slip boundary conditions weakly using Nitsche's method. This allows our discretization procedure to naturally default to a conforming approximation of Euler flow in the limit of vanishing viscosity. This also allows our method to capture boundary layers without resorting to stretched meshes [3, 4]. We prove stability and error estimates for single-patch discretizations under a smallness condition. Our error estimates are optimal for the discrete velocity field and suboptimal, by one order, for the discrete pressure field provided that that the exact solution is sufficiently regular. All of our estimates' dependencies on the viscosity and the penalty parameter of Nitsche's method are made explicit in our analysis. We utilize the methods of exact and manufactured solutions to verify our error estimates and find our discrete pressure fields converge at optimal order in contrast with our theoretical estimates. We further test the effectiveness of our method by considering the application of our discretization to the analysis of two benchmark problems: lid-driven cavity flow and confined jet impingement.

An outline of this paper is as follows. In the following section, we present some basic notation. In Section 3, we recall the steady Navier-Stokes problem subject to homogeneous Dirichlet boundary conditions. In Section 4, we briefly review B-splines, the basic building blocks of our new discretization technique, and in Section 5, we define the B-spline spaces which we will utilize to discretize velocity and pressure fields. In Section 6, we present our discrete variational formulation for the steady Navier-Stokes problem and prove continuity, stability, and *a priori* error estimates for the single-patch setting. In Section 7, we discuss the extension of our methodology to the multi-patch setting. In Sections 8 and 9, we present numerical results, and in Section 10, we draw conclusions. Before proceeding, note that one might say there is a fundamental issue concerning the fact that our analysis only covers flows subject to "small data". However, well-posedness of the continuous problem is subject to a similar constraint, and we believe the small data assumption is natural as medium- and large-Reynolds number flows are inherently unsteady in both laminar and turbulent regimes.

2 Notation

We begin this paper with some basic notation. For d a positive integer representing dimension, let $D \subset \mathbb{R}^d$ denote an arbitrary bounded Lipschitz domain with boundary ∂D. As usual, let $L^2(D)$ denote the space of square integrable functions on D and

define $\mathbf{L}^2(D) = (L^2(D))^d$. We will also utilize the more general Lebesgue spaces $L^p(D)$ where $1 \leq p \leq \infty$ and their vectorial counterparts $\mathbf{L}^p(D)$. Let $H^k(D)$ denote the space of functions in $L^2(D)$ whose k^{th}-order derivatives belong to $L^2(D)$ and define $\mathbf{H}^k(D) = \left(H^k(D)\right)^d$. We identify with $H^k(D)$ the standard Sobolev norm

$$\|v\|_{H^k(D)} = \left(\sum_{|\boldsymbol{\alpha}|<k} \|D^\alpha \mathbf{v}\|^2_{L^2(D)} \right)^{1/2}$$

where $\boldsymbol{\alpha} = (\alpha_1, \alpha_2, \ldots, \alpha_d)$ is a multi-index of non-negative integers, $|\boldsymbol{\alpha}| = \alpha_1 + \alpha_2 + \ldots + \alpha_d$, and

$$D^{\boldsymbol{\alpha}} = \frac{\partial^{|\boldsymbol{\alpha}|}}{\partial x_1^{\alpha_1} \partial x_2^{\alpha_2} \ldots \partial x_d^{\alpha_d}}.$$

We denote the Sobolev semi-norms as $|\cdot|_{H^k(D)}$, and we adopt the convention $H^0(D) = L^2(D)$. Throughout, Sobolev spaces of fractional order are defined using function space interpolation (see, e.g., Chapter 1 of [38]). We define $H^1_0(D) \subset H^1(D)$ to be the subspace of functions with homogeneous boundary conditions and define $\mathbf{H}^1_0(D)$ to be the vectorial counterpart of $H^1_0(D)$. We define $\mathbf{H}^s(\mathrm{div}; D)$ to be the Sobolev space of all functions in $\mathbf{H}^s(\Omega)$ whose divergence also belongs to $H^s(D)$. This space is equipped with the norm

$$\|\mathbf{v}\|_{\mathbf{H}^s(\mathrm{div};D)} = \left(\|\mathbf{v}\|^2_{\mathbf{H}^s(D)} + \|\mathrm{div}\, \mathbf{v}\|^2_{H^s(D)} \right)^{1/2}.$$

When $s = 0$, we omit the superscript. We also define

$$\mathbf{H}_0(\mathrm{div}; D) \quad = \quad \{\mathbf{v} \in \mathbf{H}(\mathrm{div}; D) : \mathbf{v} \cdot \mathbf{n} = 0 \text{ on } \partial D\}$$

where $\mathbf{n}$ denotes the outward pointing unit normal. Finally, we denote $L^2_0(D) \subset L^2(D)$ as the space of square-integrable functions with zero average on D.

3 The Steady Navier-Stokes Problem

In this section, we recall the steady Navier-Stokes problem subject to homogeneous Dirichlet boundary conditions. For d a positive integer, let Ω denote a Lipschitz bounded open set of $\mathbb{R}^d$. Throughout this paper, d will be either 2 or 3. The problem of interest is as follows.

(S) Given $\nu \in \mathbb{R}^+$ and $\mathbf{f} : \Omega \to \mathbb{R}^d$, find $\mathbf{u} : \bar{\Omega} \to \mathbb{R}^d$ and $p : \Omega \to \mathbb{R}$ such that

$$\nabla \cdot (\mathbf{u} \otimes \mathbf{u}) - \nabla \cdot (2\nu \nabla^s \mathbf{u}) + \mathbf{grad}\, p = \mathbf{f} \qquad \text{in } \Omega \qquad (1)$$

$$\mathrm{div}\, \mathbf{u} = 0 \qquad \text{in } \Omega \qquad (2)$$

$$\mathbf{u} = \mathbf{0} \qquad \text{on } \partial\Omega. \qquad (3)$$

Above, $\mathbf{u}$ denotes the flow velocity of a fluid moving through the domain Ω, p denotes the pressure acting on the fluid divided by the fluid density, ν denotes the kinematic viscosity of the fluid, $\mathbf{f}$ denotes a body force acting on the fluid divided by the density, and $\nabla^s\mathbf{u}$ denotes the symmetrized gradient of the velocity field defined by $\nabla^s\mathbf{u} = \frac{1}{2}\left(\nabla\mathbf{u} + (\nabla\mathbf{u})^T\right)$. Note that the pressure is only determined up to an arbitrary constant.

Assuming that $\mathbf{f} \in \mathbf{L}^2(\Omega)$, the weak form for the steady Navier-Stokes problem is written as follows:

$$(W)\begin{cases} \text{Find } \mathbf{u} \in \mathbf{H}_0^1(\Omega) \text{ and } p \in L_0^2(\Omega) \text{ such that} \\ \qquad k(\mathbf{u},\mathbf{v}) + c(\mathbf{u},\mathbf{u};\mathbf{v}) - b(p,\mathbf{v}) + b(q,\mathbf{u}) = (\mathbf{f},\mathbf{v})_{\mathbf{L}^2(\Omega)} \qquad (4) \\ \text{for all } \mathbf{v} \in \mathbf{H}_0^1(\Omega) \text{ and } q \in L_0^2(\Omega) \text{ where} \\ \qquad k(\mathbf{w},\mathbf{v}) = (2\nu\nabla^s\mathbf{w}, \nabla^s\mathbf{v})_{(L^2(\Omega))^{d\times d}}, \quad \forall \mathbf{w},\mathbf{v} \in \mathbf{H}_0^1(\Omega), \qquad (5) \\ \qquad b(q,\mathbf{v}) = (q, \operatorname{div}\mathbf{v})_{L^2(\Omega)}, \quad \forall q \in L_0^2(\Omega), \mathbf{v} \in \mathbf{H}_0^1(\Omega), \qquad (6) \\ \qquad c(\mathbf{w},\mathbf{x};\mathbf{v}) = -(\mathbf{w}\otimes\mathbf{x}, \nabla\mathbf{v})_{(L^2(\Omega))^{d\times d}}, \quad \forall \mathbf{w},\mathbf{x},\mathbf{v} \in \mathbf{H}_0^1(\Omega). \qquad (7) \end{cases}$$

Note that the trilinear form $c(\cdot,\cdot;\cdot) : \mathbf{H}_0^1(\Omega) \times \mathbf{H}_0^1(\Omega) \times \mathbf{H}_0^1(\Omega) \to \mathbb{R}$ makes sense due to the continuous Sobolev embedding

$$\mathbf{H}_0^1(\Omega) \hookrightarrow \mathbf{L}^4(\Omega). \tag{8}$$

In fact, as $\partial\Omega$ is Lipschitz, we have the stronger embedding $\mathbf{H}^1(\Omega) \hookrightarrow \mathbf{L}^4(\Omega)$.

We have the following existence and uniqueness theorem for flows subject to small data whose proof may be found in [22].

Theorem 3.1. *Problem (W) has a unique weak solution $(\mathbf{u},p) \in \mathbf{H}_0^1(\Omega) \times L_0^2(\Omega)$ provided the problem data satisfies an inequality of the form*

$$\frac{C_\Omega C_{Poin}}{\nu^2}\|\mathbf{f}\|_{\mathbf{L}^2(\Omega)} < 1 \tag{9}$$

where C_Ω is a constant which only depends on Ω and C_{Poin} is the positive constant appearing in Poincaré's inequality:

$$\|\mathbf{v}\|_{\mathbf{H}^1(\Omega)} \le C_{Poin}|\mathbf{v}|_{\mathbf{H}^1(\Omega)}, \quad \forall \mathbf{v} \in \mathbf{H}^1(\Omega) \cap \mathbf{H}_0(\operatorname{div};\Omega). \tag{10}$$

Furthermore, such a weak solution satisfies the inequality

$$|\mathbf{u}|_{\mathbf{H}^1(\Omega)} \le \frac{C_{Poin}}{\nu}\|\mathbf{f}\|_{\mathbf{L}^2(\Omega)}. \tag{11}$$

Remark 3.1. *Note that, since ν is constant and* $\operatorname{div}\mathbf{u} = 0$*,*

$$\nabla \cdot (2\nu\nabla^s\mathbf{u}) = \nu\Delta\mathbf{u}. \tag{12}$$

This inspires a different variational formulation than that presented here which is often the basis for numerical discretization (see, for example, [12]). However, such a formulation cannot easily accommodate traction boundary conditions. We have found that discrete formulations based on either of the diffusion operators given by (12) *yield qualitatively and quantitatively similar results.*

Remark 3.2. *In general, we may replace the constant-viscosity Newtonian stress tensor given here, $\mathbb{T} = 2\nu\nabla^s\mathbf{u}$, with more suitable choices of stress tensor. Our analysis does not cover this general setting.*

4 B-splines and Geometrical Mappings

In this section, we briefly introduce B-splines, the primary ingredient in our discretization technique for the steady Navier-Stokes equations. We also introduce mappings which will allow us to extend our discretization technique to general geometries of engineering interest. For an overview of B-splines, their properties, and robust algorithms for evaluating their values and derivatives, see de Boor [14] and Schumaker [35]. For the application of B-splines to finite element analysis, see Höllig [23] and Cottrell, Hughes, and Bazilevs [13].

4.1 Univariate B-splines

For two positive integers k and n, representing degree and dimensionality respectively, let us introduce the ordered knot vector

$$\Xi := \{0 = \xi_1, \xi_2, \ldots, \xi_{n+k+1} = 1\} \tag{13}$$

where

$$\xi_1 \leq \xi_2 \leq \ldots \xi_{n+k+1}.$$

Given Ξ and k, univariate B-spline basis functions are constructed recursively starting with piecewise constants ($k = 0$):

$$B_i^0(\xi) = \begin{cases} 1 & \text{if } \xi_i \leq \xi < \xi_{i+1} \\ 0 & \text{otherwise.} \end{cases} \tag{14}$$

For $k = 1, 2, 3, \ldots$, they are defined by

$$B_i^k(\xi) = \frac{\xi - \xi_i}{\xi_{i+k} - \xi_i} B_i^{k-1}(\xi) + \frac{\xi_{i+k+1} - \xi}{\xi_{i+k+1} - \xi_{i+1}} B_{i+1}^{k-1}(\xi). \tag{15}$$

When $\xi_{i+k} - \xi_i = 0$, $\frac{\xi - \xi_i}{\xi_{i+k} - \xi_i}$ is taken to be zero, and similarly, when $\xi_{i+k+1} - \xi_{i+1} = 0$, $\frac{\xi_{i+k+1} - \xi}{\xi_{i+k+1} - \xi_{i+1}}$ is taken to be zero. B-spline basis functions are piecewise polynomials of degree k, form a partition of unity, have local support, and are non-negative. We refer to linear combinations of B-spline basis functions as B-splines or simply splines.

Let us now introduce the vector $\boldsymbol{\zeta} = \{\zeta_1, \ldots, \zeta_m\}$ of knots without repetitions and a corresponding vector $\{r_1, \ldots, r_m\}$ of knot multiplicities. That is, r_i is defined to be the multiplicity of the knot ζ_i in Ξ. We assume that $r_i \leq k+1$. Let us further assume throughout that $r_1 = r_m = k+1$, *i.e*, that Ξ is an open knot vector. This allows us to easily prescribe Dirichlet boundary conditions. At the point ζ_i, B-spline basis functions have $\alpha_j := k - r_j$ continuous derivatives. We define the regularity vector $\boldsymbol{\alpha}$ by $\boldsymbol{\alpha} := \{\alpha_1, \ldots, \alpha_m\}$. By construction, $\alpha_1 = \alpha_m = -1$. In what follows, we utilize the notation

$$|\boldsymbol{\alpha}| = \min\{\alpha_i : 2 \leq i \leq m-1\} \tag{16}$$

and $\boldsymbol{\alpha} - 1 := \{-1, \alpha_2 - 1, \ldots, \alpha_{m-1} - 1, -1\}$ when $\alpha_i \geq 0$ for $2 \leq i \leq m-1$.

We denote the space of B-splines spanned by the basis functions B_i^k as

$$S_{\boldsymbol{\alpha}}^k := \operatorname{span}\left\{B_i^k\right\}_{i=1}^n. \tag{17}$$

When $k \geq 1$ and $\alpha_i \geq 0$ for $2 \leq i \leq m-1$, the derivatives of functions in $S_{\boldsymbol{\alpha}}^k$ are splines as well. In fact, we have the stronger relationship

$$\left\{\frac{d}{dx} v : v \in S_{\boldsymbol{\alpha}}^k\right\} \equiv S_{\boldsymbol{\alpha}-\mathbf{1}}^{k-1}. \tag{18}$$

One of the most important properties of univariate B-splines is refinement and, perhaps more importantly, nestedness of refinement. Knot insertion and degree elevation algorithms are described in detail in Chapter 2 of [13].

4.2 Multivariate B-splines

The definition of multivariate B-splines follows easily through a tensor-product construction. For d again a positive integer, let us consider the unit cube $\widehat{\Omega} = (0,1)^d \subset \mathbb{R}^d$, which we will henceforth refer to as the parametric domain. Mimicking the one-dimensional case, given integers k_l and n_l for $l = 1, \ldots, d$, let us introduce open knot vectors $\Xi_l = \{\xi_{1,l}, \ldots, \xi_{n_l+k_l+1,l}\}$ and the associated vectors $\boldsymbol{\zeta}_l = \{\zeta_{1,l}, \ldots, \zeta_{m_l,l}\}$, $\{r_{1,l}, \ldots, r_{m_l,l}\}$, and $\boldsymbol{\alpha}_l = \{\alpha_{1,l}, \ldots, \alpha_{m_l,l}\}$. There is a parametric Cartesian mesh $\mathcal{M}_h$ associated with these knot vectors partitioning the parametric domain into rectangular parallelepipeds. Visually,

$$\mathcal{M}_h = \left\{Q = \otimes_{l=1,\ldots,d} \left(\zeta_{i_l,l}, \zeta_{i_l+1,l}\right), 1 \leq i_l \leq m_l - 1\right\}. \tag{19}$$

For each element $Q \in \mathcal{M}_h$ we associate a parametric mesh size $h_Q = \operatorname{diam}(Q)$. We also define a shape regularity constant λ which satisfies the inequality

$$\lambda^{-1} \leq \frac{h_{Q,\min}}{h_Q} \leq \lambda, \quad \forall Q \in \mathcal{M}_h, \tag{20}$$

where $h_{Q,\min}$ denotes the length of the smallest edge of Q. A sequence of parametric meshes that satisfy the above inequality for an identical shape regularity constant is said to be locally quasi-uniform.

We associate with each knot vector Ξ_l $(l = 1, \ldots, d)$ univariate B-spline basis functions $B^{k_l}_{i_l,l}$ of degree k_l for $i_l = 1, \ldots, n_l$. On the mesh $\mathcal{M}_h$, we define the tensor-product B-spline basis functions as

$$B^{k_1,\ldots,k_d}_{i_1,\ldots,i_d} := B^{k_1}_{i_1,1} \otimes \ldots \otimes B^{k_d}_{i_d,d}, \quad i_1 = 1, \ldots, n_1, \ \ldots \ i_d = 1, \ldots, n_d. \tag{21}$$

We then accordingly define the tensor-product B-spline space as

$$S^{k_1,\ldots,k_d}_{\boldsymbol{\alpha}_1,\ldots,\boldsymbol{\alpha}_d} \equiv S^{k_1,\ldots,k_d}_{\boldsymbol{\alpha}_1,\ldots,\boldsymbol{\alpha}_d}(\mathcal{M}_h) := \operatorname{span}\left\{ B^{k_1,\ldots,k_d}_{i_1,\ldots,i_d} \right\}^{n_1,\ldots,n_d}_{i_1=1,\ldots,i_d=1}. \tag{22}$$

Like their univariate counterparts, multivariate B-spline basis functions are piecewise polynomial, form a partition of unity, have local support, and are non-negative. Defining the regularity constant

$$\alpha := \min_{l=1,\ldots,d} \min_{2 \le i_l \le m_l - 1} \{\alpha_{i_l,l}\} \tag{23}$$

we see that our B-splines are C^α-continuous throughout the domain $\widehat{\Omega}$. Refinement of multivariate B-spline bases is obtained by applying knot insertion and degree elevation in tensor-product fashion. In the remainder of the text, we consider a family of nested meshes $\{\mathcal{M}_h\}_{h \le h_0}$ and associated B-spline spaces $\left\{S^{k_1,\ldots,k_d}_{\boldsymbol{\alpha}_1,\ldots,\boldsymbol{\alpha}_d}(\mathcal{M}_h)\right\}_{h \le h_0}$ that have been obtained by successive applications of knot refinement. Furthermore, we assume throughout that the mesh family $\{\mathcal{M}_h\}_{h \le h_0}$ is locally quasi-uniform.

Note that each element $Q = \otimes_{l=1,\ldots,d} (\zeta_{i_l,l}, \zeta_{i_l+1,l})$ has the equivalent representation $Q = \otimes_{l=1,\ldots,d} (\xi_{j_l,l}, \xi_{j_l+1,l})$ for some index j_l. With this in mind, we associate with each element a support extension $\tilde{Q}$, defined as

$$\tilde{Q} := \otimes_{l=1,\ldots,d} (\xi_{j_l-k_l,l}, \xi_{j_l+k_l+1,l}). \tag{24}$$

The support extension is the interior of the set formed by the union of the supports of all B-spline basis functions whose support intersects Q. Note that each element belongs to the support extension of at most $\Pi_{l=1,\ldots,d}(2k_l + 1)$ elements.

4.3 Piecewise Smooth Functions, Geometrical Mappings, and Physical Mesh Entities

On the parametric mesh $\mathcal{M}_h$, we define the space of piecewise smooth functions with interelement regularity given by the vectors $\boldsymbol{\alpha}_1, \ldots, \boldsymbol{\alpha}_d$ as

$$C^\infty_{\boldsymbol{\alpha}_1,\ldots,\boldsymbol{\alpha}_d} = C^\infty_{\boldsymbol{\alpha}_1,\ldots,\boldsymbol{\alpha}_d}(\mathcal{M}_h). \tag{25}$$

Precisely, a function in $C^{\infty}_{\boldsymbol{\alpha}_1,\ldots,\boldsymbol{\alpha}_d}$ is a function whose restriction to an element $Q \in \mathcal{M}_h$ admits a C^{∞} extension in the closure of that element and which has $\alpha_{i_l,l}$ continuous derivatives with respect to the lth coordinate along the internal mesh faces $\{(x_1,\ldots,x_d) : x_l = \zeta_{i_l,l},\ \zeta_{j_{l'},l'} < x_{l'} < \zeta_{j_{l'+1},l'}, l' \neq l\}$ for all $i_l = 2,\ldots,m_l - 1$ and $j_{l'} = 1,\ldots,m_{l'} - 1$. Note immediately that any function lying in the B-spline space $S^{k_1,\ldots,k_d}_{\boldsymbol{\alpha}_1,\ldots,\boldsymbol{\alpha}_d}$ also lies in $C^{\infty}_{\boldsymbol{\alpha}_1,\ldots,\boldsymbol{\alpha}_d}$.

Unless specified otherwise, we assume throughout the rest of the paper that the physical domain $\Omega \subset \mathbb{R}^d$ can be exactly parametrized by a geometrical mapping $\mathbf{F} : \widehat{\Omega} \to \Omega$ belonging to $\left(C^{\infty}_{\boldsymbol{\alpha}_1,\ldots,\boldsymbol{\alpha}_d}\right)^d$ with piecewise smooth inverse. We further assume that the physical domain Ω is simply connected with connected boundary $\partial\Omega$ and the geometrical mapping is independent of the mesh family index h. A geometrical mapping meeting our criteria could be defined utilizing B-splines or Non-Uniform Rational B-Splines (NURBS) on the coarsest mesh $\mathcal{M}_{h_0}$. For examples of such mappings, see Chapter 2 of [13]. NURBS mappings are especially useful as they can represent many geometries of scientific and engineering interest and are the main tools employed in Computer Aided Design (CAD) software. Later in this paper, we will utilize a polar mapping to solve a flow problem on a cylindrical geometry. The geometrical mapping $\mathbf{F}$ naturally induces a mesh

$$\mathcal{K}_h = \{K : K = \mathbf{F}(Q), Q \in \mathcal{M}_h\} \tag{26}$$

on the physical domain Ω. We define for each element $K \in \mathcal{K}_h$ a physical mesh size

$$h_K = \|D\mathbf{F}\|_{L^{\infty}(Q)} h_Q \tag{27}$$

where Q is the pre-image of K, and we also define the support extension $\tilde{K} = \mathbf{F}(\tilde{Q})$. We define for a given mesh the global mesh size

$$h = \max\{h_K, K \in \mathcal{K}_h\}.$$

Note that as the parametric mesh family $\{\mathcal{M}_h\}_{h \leq h_0}$ is locally quasi-uniform and the geometrical mapping $\mathbf{F}$ is independent of the mesh family index h, the physical mesh family $\{\mathcal{K}_h\}_{h \leq h_0}$ is also locally quasi-uniform. We refer to the physical domain Ω and its pre-image $\widehat{\Omega}$ interchangeably as the patch. It should be noted that, in general, the domain Ω cannot be represented using just a single patch. Instead, multiple patches must be employed. We will discuss further the multi-patch setting in Section 7.

We define on the parametric mesh a set of mesh faces $\widehat{\mathcal{F}}_h = \{\widehat{F}\}$ where $\widehat{F}$ is a face of one or more elements in $\mathcal{M}_h$. We define the physical set of mesh faces as

$$\mathcal{F}_h = \{F = \mathbf{F}(\widehat{F}) : \widehat{F} \in \widehat{\mathcal{F}}_h\}$$

and we define the boundary mesh to be

$$\Gamma_h = \{F \in \mathcal{F}_h : F \subset \partial\Omega\}.$$

By construction,

$$\partial\Omega = \cup_{F\in\Gamma_h}\overline{F}.$$

Note that for each face $F \in \Gamma_h$ there is a unique $K \in \mathcal{K}_h$ such that F is a "face" of K (in the sense that F is the image of a face of Q, the pre-image of K). We hence define for such a face the mesh size

$$h_F := h_K.$$

One may also define h_F to be the wall-normal mesh-size as is done in [3]. Such a definition is more appropriate when stretched meshes are utilized in the presence of layers.

Throughout the paper, we will utilize the terminology "a constant independent of h". When we employ such terminology, we simply indicate that the constant will not depend on the given mesh and, in particular, its size. The constant may, however, depend on the domain, the shape regularity of the parametric mesh family, the polynomial degree and smoothness of the employed B-spline spaces, and global, mesh-invariant measures of the parametric mapping.

5 Discretization of Velocity and Pressure Fields

In this section, we define the B-spline spaces which we will utilize to discretize the velocity and pressure fields appearing in the steady Navier-Stokes problem. These spaces are motivated by the recent theory of isogeometric discrete differential forms [9, 10] and may be interpreted as smooth generalizations of Raviart-Thomas elements [32]. We first define our discrete velocity and pressure spaces on the parametric domain $\widehat{\Omega} = (0,1)^d$ and then define discrete spaces on the physical domain Ω using divergence- and integral-preserving transformations. We finish this section with a presentation of local approximation estimates and trace inequalities for our discrete velocity and pressure spaces. For a more in-depth discussion of the discrete velocity and pressure spaces used in this paper, see Section 5 of [19].

5.1 Discrete Spaces on the Parametric Domain

Using the notation of the previous section and assuming that

$$\alpha := \min\{|\boldsymbol{\alpha}_l| : l = 1, \dots, d\} \geq 1,$$

we define the following two spaces:

$$\widehat{\mathcal{V}}_h := \begin{cases} S^{k_1,k_2-1}_{\boldsymbol{\alpha}_1,\boldsymbol{\alpha}_2-1} \times S^{k_1-1,k_2}_{\boldsymbol{\alpha}_1-1,\boldsymbol{\alpha}_2} & \text{if } d = 2, \\ S^{k_1,k_2-1,k_3-1}_{\boldsymbol{\alpha}_1,\boldsymbol{\alpha}_2-1,\boldsymbol{\alpha}_3-1} \times S^{k_1-1,k_2,k_3-1}_{\boldsymbol{\alpha}_1-1,\boldsymbol{\alpha}_2,\boldsymbol{\alpha}_3-1} \times S^{k_1-1,k_2-1,k_3}_{\boldsymbol{\alpha}_1-1,\boldsymbol{\alpha}_2-1,\boldsymbol{\alpha}_3} & \text{if } d = 3, \end{cases}$$

$$\widehat{\mathcal{Q}}_h := \begin{cases} S^{k_1-1,k_2-1}_{\boldsymbol{\alpha}_1-1,\boldsymbol{\alpha}_2-1} & \text{if } d=2, \\ S^{k_1-1,k_2-1,k_3-1}_{\boldsymbol{\alpha}_1-1,\boldsymbol{\alpha}_2-1,\boldsymbol{\alpha}_3-1} & \text{if } d=3. \end{cases}$$

The space $\widehat{\mathcal{V}}_h$ comprises our set of discrete velocity fields while $\widehat{\mathcal{Q}}_h$ comprises our set of discrete pressure fields. Note that as $\alpha \geq 1$, our discrete velocity fields are $\mathbf{H}^1$-conforming. If we allow $\alpha = 0$, our spaces collapse to standard Raviart-Thomas mixed finite elements [32]. In order to deal with no-penetration boundary conditions, we make use of the following constrained discrete spaces:

$$\widehat{\mathcal{V}}_{0,h} := \left\{ \widehat{\mathbf{v}}_h \in \widehat{\mathcal{V}}_h : \widehat{\mathbf{v}}_h \cdot \widehat{\mathbf{n}} = 0 \text{ on } \partial\widehat{\Omega} \right\},$$

$$\widehat{\mathcal{Q}}_{0,h} := \left\{ \widehat{q}_h \in \mathcal{Q}_h : \int_{\widehat{\Omega}} \widehat{q}_h d\widehat{\mathbf{x}} = 0 \right\}.$$

Above, $\widehat{\mathbf{n}}$ denotes the outward-facing normal to $\partial\widehat{\Omega}$. As specified in the introduction, we choose to enforce no-slip boundary conditions weakly using Nitsche's method [30]. Due to the special relationship given by (18), the spaces $\widehat{\mathcal{V}}_{0,h}$ and $\widehat{\mathcal{Q}}_{0,h}$ along with the parametric divergence operator form the bounded discrete cochain complex

$$\widehat{\mathcal{V}}_{0,h} \xrightarrow{\widehat{\text{div}}} \widehat{\mathcal{Q}}_{0,h}$$

where $\widehat{\text{div}}$ is the divergence operator on the unit cube $\widehat{\Omega}$. In fact, we have a much stronger result due to the results of [9].

Proposition 5.1. *There exist L^2-stable projection operators $\widehat{\Pi}^0_{\widehat{\mathcal{V}}_h} : \mathbf{H}_0(\widehat{\text{div}};\widehat{\Omega}) \to \widehat{\mathcal{V}}_{0,h}$ and $\widehat{\Pi}^0_{\widehat{\mathcal{Q}}_h} : L^2_0(\widehat{\Omega}) \to \widehat{\mathcal{Q}}_{0,h}$ such that the following diagram commutes:*

$$\begin{array}{ccc} \mathbf{H}_0(\widehat{\text{div}};\widehat{\Omega}) & \xrightarrow{\widehat{\text{div}}} & L^2_0(\widehat{\Omega}) \\ \widehat{\Pi}^0_{\widehat{\mathcal{V}}_h}\downarrow & & \widehat{\Pi}^0_{\widehat{\mathcal{Q}}_h}\downarrow \\ \widehat{\mathcal{V}}_{0,h} & \xrightarrow{\widehat{\text{div}}} & \widehat{\mathcal{Q}}_{0,h}. \end{array} \tag{28}$$

Furthermore, there exists a positive constant $\widehat{C}_u$ independent of h such that

$$\|\widehat{\Pi}^0_{\widehat{\mathcal{V}}_h}\widehat{\mathbf{v}}\|_{\mathbf{H}^1(\widehat{\Omega})} \leq \widehat{C}_u \|\widehat{\mathbf{v}}\|_{\mathbf{H}^1(\widehat{\Omega})}, \quad \forall \widehat{\mathbf{v}} \in \mathbf{H}_0(\widehat{\text{div}};\widehat{\Omega}) \cap \mathbf{H}^1(\widehat{\Omega}). \tag{29}$$

5.2 Discrete Spaces on the Physical Domain

To define our discrete velocity and pressure spaces on the physical domain, we introduce the following pullback operators:

$$\iota_u(\mathbf{v}) := \det(D\mathbf{F})(D\mathbf{F})^{-1}(\mathbf{v}\circ\mathbf{F}), \quad \mathbf{v} \in \mathbf{H}_0(\text{div};\Omega) \tag{30}$$

$$\iota_p(q) := \det(D\mathbf{F})(q\circ\mathbf{F}), \quad q \in L^2_0(\Omega) \tag{31}$$

where $D\mathbf{F}$ is the Jacobian matrix of the parametric mapping $\mathbf{F}$. The push-forward given by (30), popularly known as the Piola transform, has two important properties: (i) it preserves the nullity of normal components, (ii) it maps divergences to divergences. On the other hand, the push-forward given by (31) has the property that it preserves the nullity of the integral operator. Due to these properties, we have the following commuting diagram:

$$\begin{array}{ccc} \mathbf{H}_0(\widehat{\mathrm{div}};\widehat{\Omega}) & \xrightarrow{\widehat{\mathrm{div}}} & L^2_0(\widehat{\Omega}) \\ {\scriptstyle \iota_u}\uparrow & & {\scriptstyle \iota_p}\uparrow \\ \mathbf{H}_0(\mathrm{div};\Omega) & \xrightarrow{\mathrm{div}} & L^2_0(\Omega). \end{array} \tag{32}$$

This motivates the use of the following discrete velocity and pressure spaces in the physical domain:

$$\mathcal{V}_{0,h} := \left\{ \mathbf{v} \in \mathbf{H}_0(\mathrm{div};\Omega) : \iota_u(\mathbf{v}) \in \widehat{\mathcal{V}}_{0,h} \right\},$$

$$\mathcal{Q}_{0,h} := \left\{ q \in L^2_0(\Omega) : \iota_p(q) \in \widehat{\mathcal{Q}}_{0,h} \right\}.$$

Furthermore, we define the projectors $\Pi^0_{\mathcal{V}_h} : \mathbf{H}_0(\mathrm{div};\Omega) \to \mathcal{V}_{0,h}$ and $\Pi^0_{\mathcal{Q}_h} : L^2(\Omega) \to \mathcal{Q}_{0,h}$ via the compositions

$$\Pi^0_{\mathcal{Q}_h} := \iota_u^{-1} \circ \widehat{\Pi}^0_{\widehat{\mathcal{Q}}_h} \circ \iota_u, \quad \Pi^0_{\mathcal{Q}_h} := \iota_p^{-1} \circ \widehat{\Pi}^0_{\widehat{\mathcal{Q}}_h} \circ \iota_p.$$

Employing the preceding results and terminology as well as the smoothness properties of the parametric mapping $\mathbf{F}$, we arrive at the following proposition.

Proposition 5.2. *The following diagram commutes:*

$$\begin{array}{ccc} \mathbf{H}_0(\mathrm{div};\Omega) & \xrightarrow{\mathrm{div}} & L^2_0(\Omega) \\ {\scriptstyle \Pi^0_{\mathcal{V}_h}}\downarrow & & {\scriptstyle \widehat{\Pi}^0_{\widehat{\mathcal{Q}}_h}}\downarrow \\ \mathcal{V}_{0,h} & \xrightarrow{\mathrm{div}} & \mathcal{Q}_{0,h}. \end{array} \tag{33}$$

Furthermore, there exists a positive constant C_u independent of h such that

$$\|\Pi^0_{\mathcal{V}_h}\mathbf{v}\|_{\mathbf{H}^1(\Omega)} \leq C_u \|\mathbf{v}\|_{\mathbf{H}^1(\Omega)}, \quad \forall \mathbf{v} \in \mathbf{H}_0(\mathrm{div};\Omega) \cap \mathbf{H}^1(\Omega). \tag{34}$$

We immediately have an inf-sup condition for our discrete velocity/pressure pair.

Proposition 5.3. *There exists a positive constant $\mathring{\beta}$ independent of h such that the following holds: for every $q_h \in \mathcal{Q}_{0,h}$, there exists a $\mathbf{v}_h \in \mathcal{V}_{0,h}$ such that:*

$$\mathrm{div}\,\mathbf{v}_h = q_h \tag{35}$$

and

$$\|\mathbf{v}_h\|_{\mathbf{H}^1(\Omega)} \leq \mathring{\beta}^{-1}\|q_h\|_{L^2(\Omega)}. \tag{36}$$

Hence,

$$\inf_{\substack{q_h\in\mathcal{Q}_{0,h}\\ q_h\neq 0}} \sup_{\mathbf{v}_h\in\mathcal{V}_{0,h}} \frac{(\operatorname{div}\mathbf{v}_h, q_h)_{L^2(\Omega)}}{\|\mathbf{v}_h\|_{\mathbf{H}^1(\Omega)}\|q_h\|_{L^2(\Omega)}} \geq \mathring{\beta}. \tag{37}$$

Proof. See the proof of Proposition 5.3 in [19]. □

We also have the following result.

Proposition 5.4. *If* $\mathbf{v}_h \in \mathcal{V}_{0,h}$ *satisfies*

$$(\operatorname{div}\mathbf{v}_h, q_h)_{L^2(\Omega)} = 0, \quad \forall q_h \in \mathcal{Q}_{0,h}, \tag{38}$$

then $\operatorname{div}\mathbf{v}_h \equiv 0$.

Proof. The proof holds trivially as div maps $\mathcal{V}_{0,h}$ onto $\mathcal{Q}_{0,h}$. □

Hence, by choosing $\mathcal{V}_{0,h}$ and $\mathcal{Q}_{0,h}$ as discrete velocity and pressure spaces, we arrive at a discretization that automatically returns velocity fields that are pointwise divergence-free.

5.3 Approximation Results and Trace Inequalities

Let us define

$$k' = \min_{l=1,\ldots,d} |k_l - 1|. \tag{39}$$

Note that the discrete velocity and pressure spaces $\mathcal{V}_{0,h}$ and $\mathcal{Q}_{0,h}$ consist of mapped piecewise polynomials which are complete up to degree k'. Hence, k' may be thought of as the polynomial degree of our discretization technique. The following result details the local approximation properties of our discrete spaces. Its proof may be found in [9].

Proposition 5.5. *Let* $K \in \mathcal{K}_h$ *and* $\tilde{K}$ *denote the support extension of* K. *For* $0 \leq j \leq s \leq k' + 1$, *we have*

$$|\mathbf{v} - \Pi^0_{\mathcal{V}_h}\mathbf{v}|_{\mathbf{H}^j(K)} \leq Ch_K^{s-j}\|\mathbf{v}\|_{\mathbf{H}^s(\tilde{K})}, \qquad \forall \mathbf{v} \in \mathbf{H}^s(\tilde{K}) \cap \mathbf{H}_0(\operatorname{div};\Omega) \tag{40}$$

$$|q - \Pi^0_{\mathcal{Q}_h}q|_{H^j(K)} \leq Ch_K^{s-j}\|q\|_{H^s(\tilde{K})}, \qquad \forall q \in H^s(\tilde{K}) \cap L^2_0(\Omega) \tag{41}$$

where C *denotes a positive constant, possibly different at each appearance, independent of* h.

Hence, our discrete spaces deliver optimal rates of convergence from an approximation point of view. We will also need the following trace estimate in our ensuing mathematical analysis. Its proof can be found in [16].

Proposition 5.6. *Let $K \in \mathcal{K}_h$ and $Q = \mathbf{F}^{-1}(K)$. Then we have*

$$\| (\nabla^s \mathbf{v}_h)\, \mathbf{n}\|_{(L^2(\partial K))^d} \leq C_{trace} h_K^{-1} \|\mathbf{v}_h\|_{\mathbf{H}^1(K)}, \qquad \forall \mathbf{v}_h \in \mathcal{V}_{0,h} \tag{42}$$

where C_{trace} denotes a positive constant independent of h.

In [18], it was shown that Proposition 5.6 holds for B-splines and parametric finite elements with $C_{trace} \sim (k')^2$. However, our numerical experience has indicated that a corresponding global trace inequality holds with $C_{trace} \sim k'$ if B-splines of maximal continuity are utilized. This allows us to select a smaller penalty parameter when employing Nitsche's method. As we will see in the next section, our convergence estimates scale inversely with the square root of Nitsche's penalty parameter. Hence, we want to select Nitsche's penalty parameter as small as possible.

6 The Discretized Problem

In this section, we approximate the homogeneous steady Navier-Stokes problem using the discrete velocity and pressure spaces introduced in the previous section. We prove continuity, stability, and *a priori* estimates for our discretization scheme in the single patch setting under a smallness condition, and we explicitly track all of our estimates' dependencies on the viscosity and Nitsche's penalty parameter.

6.1 Variational Formulation

We begin this section by presenting a discrete variational formulation for the steady Navier-Stokes problem. Since members of $\mathcal{V}_{0,h}$ do not satisfy homogeneous tangential Dirichlet boundary conditions, we resort to Nitsche's method to weakly enforce no-slip boundary conditions. Defining the bilinear form

$$k_h(\mathbf{w}, \mathbf{v}) = k(\mathbf{w}, \mathbf{v}) - \sum_{F \in \Gamma_h} \int_F 2\nu \left(((\nabla^s \mathbf{v})\, \mathbf{n}) \cdot \mathbf{w} + ((\nabla^s \mathbf{w})\, \mathbf{n}) \cdot \mathbf{v} - \frac{C_{pen}}{h_F} \mathbf{w} \cdot \mathbf{v} \right) d\mathbf{s} \tag{43}$$

where $C_{pen} \geq 1$ is a chosen positive penalty constant, our discrete formulation is written as follows.

$$(G) \begin{cases} \text{Find } \mathbf{u}_h \in \mathcal{V}_{0,h} \text{ and } p_h \in \mathcal{Q}_{0,h} \text{ such that} \\ \\ \quad k_h(\mathbf{u}_h, \mathbf{v}_h) + c(\mathbf{u}_h, \mathbf{u}_h; \mathbf{v}_h) - b(p_h, \mathbf{v}_h) + b(q_h, \mathbf{u}_h) = (\mathbf{f}, \mathbf{v}_h)_{\mathbf{L}^2(\Omega)} \\ \\ \text{for all } \mathbf{v}_h \in \mathcal{V}_{0,h},\ q_h \in \mathcal{Q}_{0,h}. \end{cases} \tag{44}$$

We have the following lemma detailing the consistency of our numerical method.

Lemma 6.1. *Suppose that* $(\mathbf{u}, p)$ *is a solution of* (W) *satisfying the regularity condition* $\mathbf{u} \in \mathbf{H}^{3/2+\epsilon}(\Omega)$ *for some* $\epsilon > 0$*. Then:*

$$k_h(\mathbf{u}, \mathbf{v}_h) + c(\mathbf{u}, \mathbf{u}; \mathbf{v}_h) - b(p, \mathbf{v}_h) + b(q_h, \mathbf{u}) = (\mathbf{f}, \mathbf{v}_h)_{\mathbf{L}^2(\Omega)} \tag{45}$$

for all $\mathbf{v}_h \in \mathcal{V}_{0,h}$ *and* $q_h \in \mathcal{Q}_{0,h}$*.*

Proof. We trivially have

$$b(q_h, \mathbf{u}) = 0, \quad \forall q_h \in \mathcal{Q}_{0,h}.$$

Now let $\mathbf{v}_h \in \mathcal{V}_{0,h}$. By the Sobolev trace theorem, the assumption $\mathbf{u} \in \mathbf{H}^{3/2+\epsilon}(\Omega)$ guarantees that $(\nabla^s \mathbf{u})\,\mathbf{n}$ is well-defined along $\partial\Omega$ and $(\nabla^s \mathbf{u})\,\mathbf{n} \in (L^2(\partial\Omega))^d$. Hence, the quantity $k_h(\mathbf{u}, \mathbf{v}_h)$ is well-defined. Utilizing integration by parts and the fact that $\mathbf{u}$ satisfies homogeneous Dirichlet boundary conditions and $\mathbf{v}_h$ satisfies homogeneous normal Dirichlet boundary conditions, we have

$$\begin{aligned} k_h(\mathbf{u}, \mathbf{v}_h) + c(\mathbf{u}, \mathbf{u}; \mathbf{v}_h) - b(p, \mathbf{v}_h) &= \int_\Omega (\nabla \cdot (\mathbf{u} \otimes \mathbf{u}) - \nabla \cdot (2\nu \nabla^s \mathbf{u}) + \mathbf{grad}\, p) \cdot \mathbf{v}_h \\ &= \int_\Omega \mathbf{f} \cdot \mathbf{v}_h \\ &= (\mathbf{f}, \mathbf{v}_h)_{\mathbf{L}^2(\Omega)}. \end{aligned}$$

This completes the proof of the lemma. □

We have the following relationship between the exact solution and a numerical solution.

Corollary 6.1. *Let* $(\mathbf{u}_h, p_h)$ *denote a solution of* (G)*, and let* $(\mathbf{u}, p)$ *denote a solution of* (W) *satisfying the regularity condition* $\mathbf{u} \in \mathbf{H}^{3/2+\epsilon}(\Omega)$ *for some* $\epsilon > 0$*. Then:*

$$\begin{aligned} k_h(\mathbf{u} - \mathbf{u}_h, \mathbf{v}_h) + c(\mathbf{u}, \mathbf{u}, \mathbf{v}_h) - c(\mathbf{u}_h, \mathbf{u}_h, \mathbf{v}_h) \\ -b(p - p_h, \mathbf{v}_h) + b(q_h, \mathbf{u} - \mathbf{u}_h) = 0 \end{aligned} \tag{46}$$

for all $\mathbf{v}_h \in \mathcal{V}_{0,h}$ *and* $q_h \in \mathcal{Q}_{0,h}$*.*

Finally, by Proposition 5.4, we have the following lemma.

Lemma 6.2. *Let* $(\mathbf{u}_h, p_h)$ *denote a solution of* (G)*. Then:*

$$\operatorname{div} \mathbf{u}_h \equiv 0 \tag{47}$$

Weak imposition of no-slip boundary conditions allows our methodology to default automatically to a compatible discretization of Euler flow in the setting of vanishing viscosity. Moreover, for large Reynolds number flows, there is a sharp boundary layer

in the vicinity of walls. Utilzing Nitsche's method allows us to account for these layers in a stable and consistent manner without having to directly resolve them [2, 3, 4]. In fact, Nitsche's method can be interpreted as a variationally consistent wall model. To better see this interpretation, let us formally rewrite our discrete variational equations as

$$\int_\Omega \mathbb{T} : \nabla^s \mathbf{v}_h d\mathbf{x} - \sum_{F\in\Gamma_h} \int_F \mathbb{Q}\cdot\mathbf{v}_h d\mathbf{s} + c(\mathbf{u}_h,\mathbf{u}_h;\mathbf{v}_h) - b(p_h,\mathbf{v}_h) + b(q_h,\mathbf{u}_h) = (\mathbf{f},\mathbf{v}_h)_{\mathbf{L}^2(\Omega)} \tag{48}$$

where $\mathbb{T}$ is a symmetric tensor satisfying

$$\begin{aligned}\int_\Omega \mathbb{T} : \mathbb{W} d\mathbf{x} &= \int_\Omega 2\nu\nabla^s\mathbf{u}_h : \mathbb{W} d\mathbf{x} - \sum_{F\in\Gamma_h}\int_F 2\nu\mathbf{u}_h\cdot(\mathbb{W}\mathbf{n})\, d\mathbf{s} \\ &= \int_\Omega 2\nu\mathbf{u}_h\cdot \operatorname{div}\mathbb{W} d\mathbf{x} \qquad \text{(in the sense of distributions)}\end{aligned} \tag{49}$$

for symmetric tensors $\mathbb{W}$ with well-defined normal trace and $\mathbb{Q}$ a vector satisfying

$$\mathbb{Q} = 2\nu\left((\nabla^s\mathbf{u}_h)\,\mathbf{n} - \frac{C_{pen}}{h}\mathbf{u}_h\right). \tag{50}$$

Above, $\mathbb{T}$ is a weakly defined viscous stress tensor and $\mathbb{Q}$ is the resultant viscous boundary traction vector. In the event that the no-slip boundary condition is met exactly, we recover $\mathbb{T} \equiv 2\nu\nabla^s\mathbf{u}_h$ and $\mathbb{Q} \equiv 2\nu\,(\nabla^s\mathbf{u}_h)\,\mathbf{n}$. Otherwise, the definitions of $\mathbb{T}$ and $\mathbb{Q}$ are changed accordingly. The tangential component of $\mathbb{Q}$ given by (50), denoted $\mathbb{Q}_{tang}$, and calculated as

$$\mathbb{Q}_{tang} = \mathbb{Q} - (\mathbb{Q}\cdot\mathbf{n})\,\mathbf{n}, \tag{51}$$

is the *effective wall shear stress vector*.

As the discrete velocity field satisfies the no-penetration boundary condition strongly, the vector $\mathbb{Q}$ is equal to the discrete shear stress $2\nu\,(\nabla^s\mathbf{u}_h)\,\mathbf{n}$ plus an additional wall shear stress term $\mathbb{Q}^+$ in the direction tangent to the wall. Specifically, we have

$$\mathbb{Q}^+ = -u^{*2}\frac{\mathbf{u}_h}{\|\mathbf{u}_h\|} \tag{52}$$

where

$$u^{*2} = \frac{2\nu C_{pen}\|\mathbf{u}_h\|}{h}. \tag{53}$$

For under-resolved flow simulations, the magnitude of $(\nabla^s\mathbf{u}_h)\,\mathbf{n}$ in the direction tangent to the wall is relatively small and, as such, the tangential component of $\mathbb{Q}$ is dominated by $\mathbb{Q}^+$. In this sense, $\mathbb{Q}^+$ becomes a model for the wall shear stress. As the mesh is refined and the flow is resolved, $\mathbb{Q}^+ \to 0$. The above interpretation allows

us to design physically motivated penalty values for Nitsche's penalty parameter. Notably, u^* may be interpreted as the friction velocity. By specifying the value of u^* using Spalding's law of the wall [36], we recover a standard wall model for under-resolved flow simulations. For more on this approach, see Section 3 of [3]. We recall, however, that the numerically inspired (53) produced results of the same quality as the u^* given by Spalding's physically inspired law of the wall.

Remark 6.1. *If we wish to impose non-homogeneous tangential Dirichlet (e.g., prescribed slip) boundary conditions, we must add the following expression to the right hand side of our discrete formulation:*

$$f_N(\mathbf{v}_h) = \sum_{F \in \Gamma_h} \int_F 2\nu \left(- \left(\left(\nabla^s \mathbf{v}_h \right) \mathbf{n} \right) \cdot \mathbf{u}_{BC} + \frac{C_{pen}}{h_F} \mathbf{u}_{BC} \cdot \mathbf{v}_h \right) d\mathbf{s} \tag{54}$$

where $\mathbf{u}_{BC}$ is a prescribed vector function defined on $\partial\Omega$. If we also wish to impose non-homogeneous normal Dirichlet (e.g., prescribed penetration) boundary conditions, we must impose these strongly and add the following expression to the left hand side of our discrete formulation:

$$c_{UW}(\mathbf{u}_h, \mathbf{v}_h) = \sum_{F \in \Gamma_h} \int_F \left(\mathbf{u}_{BC} \cdot \mathbf{n} \right)_+ \mathbf{u}_h \cdot \mathbf{v}_h d\mathbf{s} \tag{55}$$

and the following expression to the right hand side of our discrete formulation:

$$f_{UW}(\mathbf{v}_h) = - \sum_{F \in \Gamma_h} \int_F \left(\mathbf{u}_{BC} \cdot \mathbf{n} \right)_- \mathbf{u}_{BC} \cdot \mathbf{v}_h d\mathbf{s} \tag{56}$$

where

$$\left(\mathbf{u}_{BC} \cdot \mathbf{n} \right)_+ = \begin{cases} \mathbf{u}_{BC} \cdot \mathbf{n} & \text{if } \mathbf{u}_{BC} \cdot \mathbf{n} > 0 \\ 0 & \text{otherwise} \end{cases}$$

and

$$\left(\mathbf{u}_{BC} \cdot \mathbf{n} \right)_- = \begin{cases} \mathbf{u}_{BC} \cdot \mathbf{n} & \text{if } \mathbf{u}_{BC} \cdot \mathbf{n} \leq 0 \\ 0 & \text{otherwise.} \end{cases}$$

These additional terms correspond to upwinding.

6.2 Well-Posedness for Small Data

We now prove that our discrete formulation is well-posed under a smallness condition. Our method of proof mimics that of the continuous problem (see Theorem 10.1.1 of [22]). To begin, let us define the following mesh-dependent norm:

$$\|\mathbf{v}\|_h^2 := |\mathbf{v}|_{\mathbf{H}^1(\Omega)}^2 + \sum_{F \in \Gamma_h} h_F \| \left(\nabla^s \mathbf{v} \right) \mathbf{n} \|_{(L^2(F))^d}^2 + \sum_{F \in \Gamma_h} \frac{C_{pen}}{h_F} \|\mathbf{v}\|_{(L^2(F))^d}^2. \tag{57}$$

We will also denote

$$\mathring{\mathcal{V}}_{0,h} := \{\mathbf{v}_h \in \mathcal{V}_{0,h} : \operatorname{div} \mathbf{v}_h = 0\} = \{\mathbf{v}_h \in \mathcal{V}_{0,h} : b(q_h, \mathbf{v}_h) = 0,\ \forall q_h \in \mathcal{Q}_{0,h}\}\,.$$

To proceed, we need to call upon stability and continuity results that were proven in [19] for divergence-conforming B-spline discretizations of the Darcy-Stokes-Brinkman equations. These results hinge upon two assumptions regarding the size of C_{pen}. First, in light of Proposition 5.6, we assume that

$$C_{pen} \geq 4h_K C_{Poin}^2 C_{Korn} \frac{\| \left(\nabla^s \mathbf{v}_h\right) \mathbf{n}\|^2_{(L^2(\partial K))^d}}{\|\mathbf{v}_h\|^2_{\mathbf{H}^1(K)}}, \quad \forall K \in \mathcal{K}_h,\ \mathbf{v}_h \in \mathcal{V}_{0,h} \tag{58}$$

where C_{Poin} is the Poincaré constant appearing in (10) and C_{Korn} is the positive constant associated with the following Korn's inequality [6]:

$$|\mathbf{w}|^2_{\mathbf{H}^1(\Omega)} \leq C_{Korn}\left(\|\nabla^s \mathbf{w}\|^2_{(L^2(\Omega))^{d\times d}} + |\partial\Omega|^{-1/(d-1)}\|\mathbf{w}\|^2_{(L^2(\partial\Omega))^d}\right), \quad \forall \mathbf{w} \in \mathbf{H}^1(\Omega).$$

Second, we assume that

$$C_{pen} \geq 4h_0|\partial\Omega|^{-1/(d-1)} \tag{59}$$

where h_0 is the mesh size of the coarsest mesh $\mathcal{K}_0$ and $|\partial\Omega|$ denotes the length of $\partial\Omega$ for $d = 2$ and the area of $\partial\Omega$ for $d = 3$. This second assumption is necessary as rotation modes carry zero energy. Hence, weak boundary conditions are needed to control these modes in rotationally symmetric (or near rotationally symmetric) configurations. As such configurations are of significant engineering interest, we believe that any analysis results should cover these situations. Note that a constant C_{pen} satisfying the above assumption need not depend on h or ν. Rather, it only needs to depend on the size of the domain, the polynomial degree and smoothness of the discretization, the parametric shape regularity, and global, mesh-invariant measures of the parametric mapping.

Corollary 6.2. *Assume* (58) *and* (59) *are satisfied. Then we have*

$$k_h(\mathbf{w}, \mathbf{v}) \leq 2\nu C_{cont}\|\mathbf{w}\|_h\|\mathbf{v}\|_h, \quad \forall \mathbf{w}, \mathbf{v} \in \mathcal{V}_{0,h} \oplus \left(\mathbf{H}^1_0(\Omega) \cap \mathbf{H}^{3/2+\epsilon}(\Omega)\right) \tag{60}$$

$$b(p, \mathbf{v}) \leq \|p\|_{L^2(\Omega)}\|\mathbf{v}\|_h \qquad \forall p \in L^2_0(\Omega), \mathbf{v} \in \mathcal{V}_{0,h} \oplus \left(\mathbf{H}^1_0(\Omega) \cap \mathbf{H}^{3/2+\epsilon}(\Omega)\right) \tag{61}$$

$$k_h(\mathbf{w}_h, \mathbf{w}_h) \geq 2\nu C_{coerc}\|\mathbf{w}_h\|^2_h, \qquad \forall \mathbf{w}_h \in \mathring{\mathcal{V}}_{0,h} \tag{62}$$

where $\epsilon > 0$ is an arbitrary positive number and C_{cont} and C_{coerc} are positive constants which are independent of h, ν, C_{pen}, and ϵ. Furthermore, we have

$$\inf_{q_h \in \mathcal{Q}_{0,h}, q_h \neq 0} \sup_{\mathbf{v}_h \in \mathcal{V}_{0,h}} \frac{(\operatorname{div} \mathbf{v}_h, q_h)}{\|\mathbf{v}_h\|_{\mathcal{V}(h)}\|q_h\|_{\mathcal{Q}}} \geq \tilde{\beta}. \tag{63}$$

where $\tilde{\beta}$ is a positive constant independent of h and ν which asymptotically scales inversely with the square root of C_{pen}.

We will also need the following two lemmas. The first lemma gives a Lipschitz continuity result for the trilinear form $c(\cdot,\cdot;\cdot)$. This result hinges upon Sobolev embeddings which exist because our domain is Lipschitz. The second lemma gives a semi-coercivity result for the trilinear form $c(\cdot,\cdot;\cdot)$.

Lemma 6.3. *There exists a constant C_0 only dependent on Ω such that*

$$c(\mathbf{w}_1,\mathbf{x};\mathbf{v}) - c(\mathbf{w}_2,\mathbf{x};\mathbf{v}) \leq C_0|\mathbf{w}_1-\mathbf{w}_2|_{\mathbf{H}^1(\Omega)}|\mathbf{x}|_{\mathbf{H}^1(\Omega)}|\mathbf{v}|_{\mathbf{H}^1(\Omega)} \tag{64}$$

for all $\mathbf{w}_1,\mathbf{w}_2,\mathbf{x},\mathbf{v} \in \mathbf{H}^1(\Omega)\cap\mathbf{H}_0(\mathrm{div};\Omega)$.

Proof. Let $\mathbf{w}_1,\mathbf{w}_2,\mathbf{x},\mathbf{v} \in \mathbf{H}^1(\Omega)\cap\mathbf{H}_0(\mathrm{div};\Omega)$ be arbitrary. Note that since $\partial\Omega$ is Lipschitz, we have the continuous embedding

$$H^1(\Omega) \hookrightarrow L^4(\Omega).$$

By linearity and the Cauchy-Schwarz inequality, we can then write

$$\begin{aligned} c(\mathbf{w}_1,\mathbf{x};\mathbf{v}) - c(\mathbf{w}_2,\mathbf{x};\mathbf{v}) &= -\left((\mathbf{w}_1-\mathbf{w}_2)\otimes\mathbf{x},\nabla\mathbf{v}\right)_{(L^2(\Omega))^{d\times d}} \\ &\leq \|\mathbf{w}_1-\mathbf{w}_2\|_{\mathbf{L}^4(\Omega)}\|\mathbf{x}\|_{\mathbf{L}^4(\Omega)}\|\nabla\mathbf{v}\|_{(L^2(\Omega))^{d\times d}}. \end{aligned}$$

Let C_{embed} denote the positive embedding constant dependent only on the domain Ω such that

$$\|\mathbf{y}\|_{\mathbf{L}^4(\Omega)} \leq C_{embed}\|\mathbf{y}\|_{\mathbf{H}^1(\Omega)}, \quad \forall \mathbf{y}\in\mathbf{H}^1(\Omega).$$

Then we have

$$c(\mathbf{w}_1,\mathbf{x};\mathbf{v}) - c(\mathbf{w}_2,\mathbf{x};\mathbf{v}) \leq C_{embed}^2\|\mathbf{w}_1-\mathbf{w}_2\|_{\mathbf{H}^1(\Omega)}\|\mathbf{x}\|_{\mathbf{H}^1(\Omega)}\|\nabla\mathbf{v}\|_{(L^2(\Omega))^{d\times d}}.$$

The lemma follows with $C_0 = C_{embed}^2 C_{poin}^2$ where C_{Poin} is the Poincaré constant appearing in (10). □

Lemma 6.4. *Suppose $\mathbf{w},\mathbf{v}\in\mathbf{H}^1(\Omega)\cap\mathbf{H}_0(\mathrm{div};\Omega)$ such that $\mathrm{div}\,\mathbf{w}=0$. Then*

$$c(\mathbf{w},\mathbf{v};\mathbf{v}) = 0. \tag{65}$$

Proof. We write

$$c(\mathbf{w},\mathbf{v};\mathbf{v}) = -\int_\Omega (\mathbf{w}\otimes\mathbf{v}) : \nabla\mathbf{v}\, d\mathbf{x}.$$

Since $\mathrm{div}\,\mathbf{w}=0$, we have

$$c(\mathbf{w},\mathbf{v};\mathbf{v}) = -\frac{1}{2}\int_\Omega \mathrm{div}\left(\mathbf{w}|\mathbf{v}|^2\right) d\mathbf{x}.$$

The lemma is then simply a result of the divergence theorem. □

With Corollary 6.2 and Lemmata 6.3 and 6.4, we can prove the following proposition which gives the well-posedness of the linearized Oseen problem.

Proposition 6.1. *Let* $\mathbf{w} \in \mathbf{H}^1(\Omega) \cap \mathbf{H}_0(\mathrm{div};\Omega)$ *such that* $\mathrm{div}\,\mathbf{w} = 0$*, and assume* (58) *and* (59) *are satisfied. Then the following problem has a unique solution: find* $(\mathbf{x}_h, r_h) \in \mathcal{V}_{0,h} \times \mathcal{Q}_{0,h}$ *such that*

$$k_h(\mathbf{x}_h, \mathbf{v}_h) + c(\mathbf{w}, \mathbf{x}_h; \mathbf{v}_h) - b(r_h, \mathbf{v}_h) + b(q_h, \mathbf{x}_h) = (\mathbf{f}, \mathbf{v}_h)_{\mathbf{L}^2(\Omega)} \tag{66}$$

for all $\mathbf{v}_h \in \mathcal{V}_{0,h}$, $q_h \in \mathcal{Q}_{0,h}$*. Furthermore, the unique solution of the linearized Oseen problem satisfies* $\mathrm{div}\,\mathbf{x}_h = 0$ *and the bound*

$$\|\mathbf{x}_h\|_h \leq \frac{C_{Poin}}{2\nu C_{coerc}} \|\mathbf{f}\|_{\mathbf{L}^2(\Omega)} \tag{67}$$

where C_{Poin} *is the Poincaré constant appearing in (10) and* C_{coerc} *is the coercivity constant appearing in Corollary 6.2.*

Proof. Existence and uniqueness are a direct result of Brezzi's theorem, Corollary 6.2, and Lemmata 6.3 and 6.4. Since $\mathrm{div}\,\mathcal{V}_{0,h} = \mathcal{Q}_{0,h}$, we automatically have $\mathrm{div}\,\mathbf{x}_h = 0$. To prove the *a priori* bound, we write using (66) and the coercivity of $k_h(\cdot,\cdot)$

$$\begin{aligned}
\|\mathbf{x}_h\|_h^2 &\leq \frac{1}{2\nu C_{coerc}} k_h(\mathbf{x}_h, \mathbf{x}_h) \\
&= \frac{1}{2\nu C_{coerc}} \left((\mathbf{f}, \mathbf{x}_h)_{\mathbf{L}^2(\Omega)} - c(\mathbf{w}, \mathbf{x}_h; \mathbf{x}_h) - b(r_h, \mathbf{x}_h) \right).
\end{aligned}$$

Using Lemma 6.4 to set $c(\mathbf{w}, \mathbf{x}_h; \mathbf{x}_h) = 0$ and $\mathrm{div}\,\mathbf{x}_h = 0$ to set $b(r_h, \mathbf{x}_h) = 0$, we can complete the proof:

$$\begin{aligned}
\|\mathbf{x}_h\|_h^2 &\leq \frac{1}{2\nu C_{coerc}} (\mathbf{f}, \mathbf{x}_h)_{\mathbf{L}^2(\Omega)} \\
&\leq \frac{1}{2\nu C_{coerc}} \|\mathbf{f}\|_{\mathbf{L}^2(\Omega)} \|\mathbf{x}_h\|_{\mathbf{L}^2(\Omega)} \\
&\leq \frac{C_{Poin}}{2\nu C_{coerc}} \|\mathbf{f}\|_{\mathbf{L}^2(\Omega)} |\mathbf{x}_h|_{\mathbf{H}^1(\Omega)}.
\end{aligned}$$

□

We are now ready to establish well-posedness results for the full Navier-Stokes problem. To do so, we will attempt to obtain the solution to the discrete Navier-Stokes problem through the iterative solution of a sequence of Oseen problems. Notably, given $\mathbf{u}_0 \in \mathring{\mathcal{V}}_{0,h}$, we seek the limit of the following iterative solution process: for $i = 1, 2, 3, \ldots$ find $(\mathbf{u}_i, p_i) \in \mathcal{V}_{0,h} \times \mathcal{Q}_{0,h}$ such that

$$k_h(\mathbf{u}_i, \mathbf{v}_h) + c(\mathbf{u}_{i-1}, \mathbf{u}_i; \mathbf{v}_h) - b(p_i, \mathbf{v}_h) + b(q_h, \mathbf{u}_i) = (\mathbf{f}, \mathbf{v}_h)_{\mathbf{L}^2(\Omega)} \tag{68}$$

for all $\mathbf{v}_h \in \mathcal{V}_{0,h}$, $q_h \in \mathcal{Q}_{0,h}$. Well-posedness hinges upon the convergence of this iterative solution process, and convergence of this process is further contingent upon a small data constraint.

Theorem 6.1. *Assume* (58) *and* (59) *are satisfied, and further assume that*

$$\frac{C_0 C_{Poin}}{(2\nu)^2 C_{coerc}^2} \|\mathbf{f}\|_{\mathbf{L}^2(\Omega)} < 1 \tag{69}$$

where C_0 is the continuity constant appearing in Lemma 6.3, C_{Poin} is the Poincaré constant appearing in (10), and C_{coerc} is the coercivity constant appearing in Corollary 6.2. Then Problem (G) has a unique solution $(\mathbf{u}_h, p_h) \in \mathcal{V}_{0,h} \times \mathcal{Q}_{0,h}$. Furthermore, the unique solution satisfies

$$\|\mathbf{u}_h\|_h \leq \frac{C_{Poin}}{2\nu C_{coerc}} \|\mathbf{f}\|_{\mathbf{L}^2(\Omega)} \tag{70}$$

$$\|p_h\|_{\mathbf{L}^2(\Omega)} \leq \tilde{\beta}^{-1} \left(\frac{C_0 C_{Poin}}{(2\nu)^2 C_{coerc}^2} + \frac{C_{cont}}{C_{coerc}} + 1 \right) C_{Poin} \|\mathbf{f}\|_{\mathbf{L}^2(\Omega)} \tag{71}$$

where $\tilde{\beta}$ and C_{cont} are the inf-sup and continuity constants appearing in Corollary 6.2.

Proof. Begin by defining $S : \mathring{\mathcal{V}}_{0,h} \to \mathring{\mathcal{V}}_{0,h}$ to be the nonlinear operator which returns the divergence-free velocity solution of (66) given a divergence-free velocity field $\mathbf{w}_h \in \mathring{\mathcal{V}}_{0,h}$. Note that by Proposition 6.1

$$\|S(\mathbf{w}_h)\|_h \leq \frac{C_{Poin}}{2\nu C_{coerc}} \|\mathbf{f}\|_{\mathbf{L}^2(\Omega)}.$$

Therefore, the nonlinear operator S maps $\mathring{\mathcal{V}}_{0,h}$ into

$$\mathcal{B}_h := \left\{ \mathbf{w}_h \in \mathring{\mathcal{V}}_{0,h} : \|\mathbf{w}_h\|_h \leq \frac{C_{Poin}}{2\nu C_{coerc}} \|\mathbf{f}\|_{\mathbf{L}^2(\Omega)} \right\}.$$

Now, let $\mathbf{w}_1, \mathbf{w}_2 \in \mathring{\mathcal{V}}_{0,h}$ and $\overline{\mathbf{w}}_1 = S(\mathbf{w}_1)$, $\overline{\mathbf{w}}_2 = S(\mathbf{w}_2)$. By using the coercivity of $k_h(\cdot,\cdot)$ given by Corollary 6.2 we have

$$2\nu C_{coerc} \|\overline{\mathbf{w}}_1 - \overline{\mathbf{w}}_2\|_h^2 \leq k_h(\overline{\mathbf{w}}_1 - \overline{\mathbf{w}}_2, \overline{\mathbf{w}}_1 - \overline{\mathbf{w}}_2). \tag{72}$$

By (66), we have

$$k_h(\overline{\mathbf{w}}_1, \overline{\mathbf{w}}_1 - \overline{\mathbf{w}}_2) = -c(\mathbf{w}_1, \overline{\mathbf{w}}_1, \overline{\mathbf{w}}_1 - \overline{\mathbf{w}}_2) + (\mathbf{f}, \overline{\mathbf{w}}_1 - \overline{\mathbf{w}}_2)_{\mathbf{L}^2(\Omega)}$$

and

$$k_h(\overline{\mathbf{w}}_2, \overline{\mathbf{w}}_1 - \overline{\mathbf{w}}_2) = -c(\mathbf{w}_2, \overline{\mathbf{w}}_2, \overline{\mathbf{w}}_1 - \overline{\mathbf{w}}_2) + (\mathbf{f}, \overline{\mathbf{w}}_1 - \overline{\mathbf{w}}_2)_{\mathbf{L}^2(\Omega)}$$

since div $(\overline{\mathbf{w}}_1 - \overline{\mathbf{w}}_2) = 0$. Hence,

$$\begin{aligned} 2\nu C_{coerc}\|\overline{\mathbf{w}}_1 - \overline{\mathbf{w}}_2\|_h^2 &\leq c(\mathbf{w}_2, \overline{\mathbf{w}}_2, \overline{\mathbf{w}}_1 - \overline{\mathbf{w}}_2) - c(\mathbf{w}_1, \overline{\mathbf{w}}_1, \overline{\mathbf{w}}_1 - \overline{\mathbf{w}}_2) \\ &= -c(\mathbf{w}_2, \overline{\mathbf{w}}_1 - \overline{\mathbf{w}}_2, \overline{\mathbf{w}}_1 - \overline{\mathbf{w}}_2) \\ &\quad + c(\mathbf{w}_2, \overline{\mathbf{w}}_1, \overline{\mathbf{w}}_1 - \overline{\mathbf{w}}_2) - c(\mathbf{w}_1, \overline{\mathbf{w}}_1, \overline{\mathbf{w}}_1 - \overline{\mathbf{w}}_2). \end{aligned}$$

By the continuity and coercivity properties given in Lemmata 6.3 and 6.4, we can write

$$2\nu C_{coerc}\|\overline{\mathbf{w}}_1 - \overline{\mathbf{w}}_2\|_h^2 \leq C_0\|\mathbf{w}_2 - \mathbf{w}_1\|_h\|\overline{\mathbf{w}}_1\|_h\|\overline{\mathbf{w}}_1 - \overline{\mathbf{w}}_2\|_h.$$

Since $\overline{\mathbf{w}}_1 \in \mathcal{B}_h$, we thus have

$$\|\overline{\mathbf{w}}_1 - \overline{\mathbf{w}}_2\|_h \leq \mu\|\mathbf{w}_2 - \mathbf{w}_1\|_h$$

where μ is precisely

$$\mu = \frac{C_0 C_{Poin}}{(2\nu)^2 C_{coerc}^2}\|\mathbf{f}\|_{\mathbf{L}^2(\Omega)}.$$

By assumption $\mu < 1$, and we therefore have proved S is a contractive map. By the Banach fixed point theorem, the nonlinear problem

$$\mathbf{u}_h = S(\mathbf{u}_h)$$

has a unique solution which lies in $\mathcal{B}_h$ and is precisely the discrete velocity solution (now proven unique) of Problem (G). Given $\mathbf{u}_h$, uniqueness of the discrete pressure solution p_h is a direct result of the inf-sup condition.

We now prove the stability bounds. The bound for $\mathbf{u}_h$ is straight-forward since $\mathbf{u}_h \in \mathcal{B}_h$. To prove the bound for p_h, we utilize the inf-sup condition, the continuity of $k_h(\cdot,\cdot)$, the continuity of $c(\cdot,\cdot;\cdot)$, and Poincaré's inequality:

$$\begin{aligned} \tilde{\beta}\|p_h\|_{\mathbf{L}^2(\Omega)} &\leq \sup_{\mathbf{v}_h \in \mathcal{V}_{0,h}} \frac{b(p_h, \mathbf{v}_h)}{\|\mathbf{v}_h\|_h} \\ &= \sup_{\mathbf{v}_h \in \mathcal{V}_{0,h}} \frac{-(\mathbf{f}, \mathbf{v}_h)_{\mathbf{L}^2(\Omega)} + k_h(\mathbf{u}_h, \mathbf{v}_h) + c(\mathbf{u}_h, \mathbf{u}_h; \mathbf{v}_h)}{\|\mathbf{v}_h\|_h} \\ &\leq \sup_{\mathbf{v}_h \in \mathcal{V}_{0,h}} \frac{\|\mathbf{f}\|_{\mathbf{L}^2(\Omega)}\|\mathbf{v}_h\|_{\mathbf{L}^2(\Omega)} + 2\nu C_{cont}\|\mathbf{u}_h\|_h\|\mathbf{v}_h\|_h + C_0\|\mathbf{u}_h\|_h^2\|\mathbf{v}_h\|_h}{\|\mathbf{v}_h\|_h} \\ &\leq \sup_{\mathbf{v}_h \in \mathcal{V}_{0,h}} \frac{C_{Poin}\|\mathbf{f}\|_{\mathbf{L}^2(\Omega)}\|\mathbf{v}_h\|_h + 2\nu C_{cont}\|\mathbf{u}_h\|_h\|\mathbf{v}_h\|_h + C_0\|\mathbf{u}_h\|_h^2\|\mathbf{v}_h\|_h}{\|\mathbf{v}_h\|_h}. \end{aligned}$$

The result then follows by invoking the bound for $\mathbf{u}_h$. □

To the best of our knowledge, the above theorem is the first of its kind for $\mathbf{H}^1$ quadrilateral- and hexahedral-based spline finite element discretizations written in divergence-form. Such a result also hypothetically exists for Scott-Vogelius discretizations on tetrahedra [41], but these discretizations are limited to an extremely restrictive class of macro-element meshes. Well-posedness gives us the confidence that, at the very least, our formulation gives a unique solution under a smallness condition not unlike that for the continuous problem. In the next section, we will show that our discrete solution converges to the exact solution under a slightly more restrictive smallness condition.

It is interesting to note that the proof of Theorem 6.1 guarantees that the fixed point iteration given by (68) converges to the exact solution for *any* initial divergence-free velocity field. Furthermore, the iterates exhibit the linear convergence rate

$$\|\mathbf{u}_{n+1} - \mathbf{u}_n\|_h \leq \mu^n \|\mathbf{u}_1 - \mathbf{u}_0\|_h$$

for

$$\mu = \frac{C_0 C_{Poin}}{(2\nu)^2 C_{coerc}^2} \|\mathbf{f}\|_{\mathbf{L}^2(\Omega)} < 1.$$

This fixed-point scheme can be accelerated using a Newton-Raphson procedure.

6.3 *A Priori* Error Estimates for Small Data

We are now ready to show that our discrete solution fields converge to the exact solution fields under smallness and regularity conditions. Our method of proof largely mimics that of Theorem 4.8 in [11] for the two-dimensional Navier-Stokes equations. However, our proof is more straight-forward, primarily due to four facts: (1) we employ natively divergence-free discretizations, (2) we employ smooth approximation spaces, (3) we have a simpler treatment of the convection operator, and (4) we do not include stress as an auxiliary variable.

Our first error estimate reads as follows. Note that it is explicit in the mesh-size h, the diffusivity ν, and the penalty parameter C_{pen}.

Theorem 6.2. *Assume* (58) *and* (59) *are satisfied, and further assume that*

$$\max\left\{\frac{C_0 C_{Poin}}{(2\nu)^2 C_{coerc}^2}, \frac{C_\Omega C_{Poin}}{\nu^2}, \frac{C_0 C_{Poin}}{\nu^2 C_{coerc}}\right\} \|\mathbf{f}\|_{\mathbf{L}^2(\Omega)} < 1 \tag{73}$$

where C_0 is the continuity constant appearing in Lemma 6.3, C_{Poin} is the Poincaré constant appearing in (10), C_Ω is the domain-dependent constant appearing in Theorem 3.1, and C_{coerc} is the coercivity constant appearing in Corollary 6.2. Let $(\mathbf{u}, p)$ and $(\mathbf{u}_h, p_h)$ denote the solutions of Problems (W) and (G) respectively. Under the assumption that $\mathbf{u} \in \mathbf{H}^{3/2+\epsilon}(\Omega)$ for some $\epsilon > 0$, we have

$$\|\mathbf{u} - \mathbf{u}_h\|_h \leq (1 + 2\kappa\gamma) \inf_{\mathbf{v}_h \in \mathring{\mathcal{V}}_{0,h}} \|\mathbf{u} - \mathbf{v}_h\|_h \tag{74}$$

and

$$\|p - p_h\|_{L^2(\Omega)} \leq \left(1 + \frac{1}{\tilde{\beta}}\right) \inf_{q_h \in \mathcal{Q}_{0,h}} \|p - q_h\|_{L^2(\Omega)} + \frac{\kappa}{\tilde{\beta}} \|\mathbf{u} - \mathbf{u}_h\|_h \tag{75}$$

where

$$\kappa = 2\nu C_{cont} + \left(1 + \frac{1}{2C_{coerc}}\right) \frac{C_0 C_{Poin}}{\nu} \|\mathbf{f}\|_{\mathbf{L}^2(\Omega)} < 2\nu \left(C_{cont} + 2C_{coerc}^2 + C_{coerc}\right), \tag{76}$$

$$\gamma = \frac{1}{2\nu C_{coerc}}, \tag{77}$$

and $\tilde{\beta}$ and C_{cont} are the inf-sup and continuity constants appearing in Corollary 6.2.

Proof. We begin by proving the estimate for the velocity error. Let $\mathbf{v}_h \in \mathring{\mathcal{V}}_{0,h}$ such that $\operatorname{div} \mathbf{v}_h = 0$. By the coercivity of $k_h(\cdot,\cdot)$ over $\mathring{\mathcal{V}}_{0,h}$, we have

$$2\nu C_{coerc} \|\mathbf{v}_h - \mathbf{u}_h\|_h^2 \leq k_h(\mathbf{v}_h - \mathbf{u}_h, \mathbf{v}_h - \mathbf{u}_h).$$

By the consistency given by Corollary 6.1 and the divergence-free condition $\operatorname{div}(\mathbf{v}_h - \mathbf{u}_h) = 0$, we have

$$\begin{aligned} k_h(\mathbf{v}_h - \mathbf{u}_h, \mathbf{v}_h - \mathbf{u}_h) = {} & k_h(\mathbf{v}_h - \mathbf{u}, \mathbf{v}_h - \mathbf{u}_h) \\ & - c(\mathbf{u}, \mathbf{u}; \mathbf{v}_h - \mathbf{u}_h) + c(\mathbf{u}_h, \mathbf{u}_h; \mathbf{v}_h - \mathbf{u}_h). \end{aligned}$$

Then, by using the continuity of $k_h(\cdot,\cdot)$, we can write

$$\begin{aligned} 2\nu C_{coerc} \|\mathbf{v}_h - \mathbf{u}_h\|_h^2 &\leq k_h(\mathbf{v}_h - \mathbf{u}, \mathbf{v}_h - \mathbf{u}_h) \\ &\quad - c(\mathbf{u}, \mathbf{u}; \mathbf{v}_h - \mathbf{u}_h) + c(\mathbf{u}_h, \mathbf{u}_h; \mathbf{v}_h - \mathbf{u}_h) \\ &\leq 2\nu C_{cont} \|\mathbf{v}_h - \mathbf{u}\|_h \|\mathbf{v}_h - \mathbf{u}_h\|_h + T \end{aligned} \tag{78}$$

where

$$T := -c(\mathbf{u}, \mathbf{u}; \mathbf{v}_h - \mathbf{u}_h) + c(\mathbf{u}_h, \mathbf{u}_h; \mathbf{v}_h - \mathbf{u}_h).$$

We now utilize a splitting. Let us decompose

$$T = T_1 + T_2 + T_3 + T_4 \tag{79}$$

where

$$\begin{aligned} T_1 &= -c(\mathbf{v}_h, \mathbf{u}; \mathbf{v}_h - \mathbf{u}_h) + c(\mathbf{u}_h, \mathbf{u}; \mathbf{v}_h - \mathbf{u}_h) \\ T_2 &= -c(\mathbf{u}_h, \mathbf{v}_h - \mathbf{u}_h; \mathbf{v}_h - \mathbf{u}_h) \\ T_3 &= c(\mathbf{v}_h, \mathbf{u}; \mathbf{v}_h - \mathbf{u}_h) - c(\mathbf{u}, \mathbf{u}; \mathbf{v}_h - \mathbf{u}_h) \\ T_4 &= c(\mathbf{u}_h, \mathbf{v}_h - \mathbf{u}; \mathbf{v}_h - \mathbf{u}_h). \end{aligned}$$

By Lemma 6.3, we can write

$$
\begin{aligned}
T_1 &\leq C_0 |\mathbf{u}|_{\mathbf{H}^1(\Omega)} \|\mathbf{v}_h - \mathbf{u}_h\|_h^2 \\
T_3 &\leq C_0 |\mathbf{u}|_{\mathbf{H}^1(\Omega)} \|\mathbf{v}_h - \mathbf{u}_h\|_h \|\mathbf{v}_h - \mathbf{u}\|_h \\
T_4 &\leq C_0 \|\mathbf{u}_h\|_h \|\mathbf{v}_h - \mathbf{u}_h\|_h \|\mathbf{v}_h - \mathbf{u}\|_h
\end{aligned}
$$

and by Lemma 6.4, we have

$$
T_2 = 0. \tag{80}
$$

Theorems 3.1 and 6.1 immediately give the bounds

$$
T_1 \leq \frac{C_0 C_{Poin}}{\nu} \|\mathbf{f}\|_{\mathbf{L}^2(\Omega)} \|\mathbf{v}_h - \mathbf{u}_h\|_h^2. \tag{81}
$$

$$
T_3 \leq \frac{C_0 C_{Poin}}{\nu} \|\mathbf{f}\|_{\mathbf{L}^2(\Omega)} \|\mathbf{v}_h - \mathbf{u}_h\|_h \|\mathbf{v}_h - \mathbf{u}\|_h \tag{82}
$$

$$
T_4 \leq \frac{C_0 C_{Poin}}{2\nu C_{coerc}} \|\mathbf{f}_h\|_{\mathbf{L}^2(\Omega)} \|\mathbf{v}_h - \mathbf{u}_h\|_h \|\mathbf{v}_h - \mathbf{u}\|_h \tag{83}
$$

Substituting (79), (80), (81), (82), and (83) into (78), we obtain

$$
(1 - \alpha) \|\mathbf{v}_h - \mathbf{u}_h\|_h \leq \kappa\gamma \|\mathbf{v}_h - \mathbf{u}\|_h
$$

where

$$
\alpha = \frac{C_0 C_{Poin}}{2\nu^2 C_{coerc}} \|\mathbf{f}\|_{\mathbf{L}^2(\Omega)},
$$

$$
\gamma = \frac{1}{2\nu C_{coerc}},
$$

and

$$
\kappa = 2\nu C_{cont} + \left(1 + \frac{1}{2C_{coerc}}\right) \frac{C_0 C_{Poin}}{\nu} \|\mathbf{f}\|_{\mathbf{L}^2(\Omega)}.
$$

By assumption, $\alpha < 1/2$ and hence

$$
\|\mathbf{v}_h - \mathbf{u}_h\|_h \leq 2\kappa\gamma \|\mathbf{v}_h - \mathbf{u}\|_h.
$$

To finish the proof for the velocity error, we perform a sum decomposition as follows:

$$
\begin{aligned}
\|\mathbf{u} - \mathbf{u}_h\|_h &\leq \inf_{\mathbf{v}_h \in \mathring{\mathcal{V}}_{0,h}} \left(\|\mathbf{u} - \mathbf{v}_h\|_h + \|\mathbf{v}_h - \mathbf{u}_h\|_h\right) \\
&\leq (1 + 2\kappa\gamma) \inf_{\mathbf{v}_h \in \mathring{\mathcal{V}}_{0,h}} \|\mathbf{u} - \mathbf{v}_h\|_h.
\end{aligned}
$$

We now proceed to the estimate for the pressure error. Let $q_h \in \mathcal{Q}_{0,h}$. By the inf-sup condition, we have

$$
\|q_h - p_h\|_{L^2(\Omega)} \leq \frac{1}{\widetilde{\beta}} \sup_{\mathbf{v}_h \in \mathcal{V}_{0,h}} \frac{b(q_h - p_h, \mathbf{v}_h)}{\|\mathbf{v}_h\|_h}. \tag{84}
$$

By the consistency given by Corollary 6.1, we have, for any $\mathbf{v}_h \in \mathcal{V}_{0,h}$,

$$\begin{aligned} b(q_h - p_h, \mathbf{v}_h) &= b(q_h - p, \mathbf{v}_h) + k_h(\mathbf{u} - \mathbf{u}_h, \mathbf{v}_h) \\ &\quad + c(\mathbf{u}, \mathbf{u}; \mathbf{v}_h) - c(\mathbf{u}_h, \mathbf{u}_h; \mathbf{v}_h) \\ &= b(q_h - p, \mathbf{v}_h) + k_h(\mathbf{u} - \mathbf{u}_h, \mathbf{v}_h) \\ &\quad + c(\mathbf{u}, \mathbf{u} - \mathbf{u}_h; \mathbf{v}_h) + c(\mathbf{u} - \mathbf{u}_h, \mathbf{u}_h; \mathbf{v}_h). \end{aligned}$$

Our continuity estimates from Corollary 6.2 and Lemma 6.3 then give the bound

$$\begin{aligned} &b(q_h - p_h, \mathbf{v}_h) \leq \\ &\left(\|q_h - p\|_{L^2(\Omega)} + \left(2\nu C_{cont} + C_0\left(|\mathbf{u}|_{\mathbf{H}^1(\Omega)} + \|\mathbf{u}_h\|_h\right)\right)\|\mathbf{u} - \mathbf{u}_h\|_h\right)\|\mathbf{v}_h\|_h. \end{aligned}$$

Theorems 3.1 and 6.1 give

$$2\nu C_{cont} + C_0\left(|\mathbf{u}|_{\mathbf{H}^1(\Omega)} + \|\mathbf{u}_h\|_h\right) \leq \kappa,$$

so we can write

$$b(q_h - p_h, \mathbf{v}_h) \leq \left(\|q_h - p\|_{L^2(\Omega)} + \kappa\|\mathbf{u} - \mathbf{u}_h\|_h\right)\|\mathbf{v}_h\|_h.$$

Substituting the above expression into (84), we acquire the estimate

$$\|q_h - p_h\|_{L^2(\Omega)} \leq \frac{1}{\tilde{\beta}}\|q_h - p\|_{L^2(\Omega)} + \frac{\kappa}{\tilde{\beta}}\|\mathbf{u} - \mathbf{u}_h\|_h.$$

To finish the proof for the pressure error, we again perform a sum decomposition as follows:

$$\begin{aligned} \|p - p_h\|_{L^2(\Omega)} &\leq \inf_{q_h \in \mathcal{Q}_{0,h}} \left(\|p - q_h\|_{L^2(\Omega)} + \|q_h - p_h\|_{L^2(\Omega)}\right) \\ &\leq \left(1 + \frac{1}{\tilde{\beta}}\right) \inf_{q_h \in \mathcal{Q}_{0,h}} \|p - q_h\|_{L^2(\Omega)} + \frac{\kappa}{\tilde{\beta}}\|\mathbf{u} - \mathbf{u}_h\|_h. \end{aligned}$$

□

Our next error estimate gives us *a priori* convergence estimates that are optimal for the discrete velocity field and suboptimal, by one order, for the discrete pressure field.

Theorem 6.3. *Let the assumptions of Theorem 6.2 hold true. Furthermore, let* $(\mathbf{u}, p)$ *and* $(\mathbf{u}_h, p_h)$ *denote the solutions of Problems* (W) *and* (G)*, respectively. Under the assumption that* $\mathbf{u} \in \mathbf{H}^{j+1}(\Omega)$ *and* $p \in H^j(\Omega)$ *for some* $j > 1/2$*, we have*

$$\|\mathbf{u} - \mathbf{u}_h\|_h \leq C_{\mathbf{u}}\left(1 + 2\kappa\gamma\right) h^s \|\mathbf{u}\|_{\mathbf{H}^{s+1}(\Omega)} \tag{85}$$

and

$$\|p - p_h\|_{L^2(\Omega)} \leq C_p \left(1 + \frac{1}{\tilde{\beta}}\right) h^s \|p\|_{H^s(\Omega)} + \frac{\kappa}{\tilde{\beta}} \|\mathbf{u} - \mathbf{u}_h\|_h \tag{86}$$

for $s = \min\{k', j\}$ *where* κ *is defined by* (76), γ *is defined by* (77), $\tilde{\beta}$ *is the discrete inf-sup constant,* $C_{\mathbf{u}}$ *is a positive constant independent of* h *and* ν *which asymptotically scales with the square root of* C_{pen}*, and* C_p *is a positive constant independent of* h*,* ν*, and* C_{pen}*.*

Proof. We first prove (85). Recall the error estimate given by (74):

$$\|\mathbf{u} - \mathbf{u}_h\|_h \leq (1 + 2\kappa\gamma) \inf_{\mathbf{v}_h \in \mathring{\mathcal{V}}_{0,h}} \|\mathbf{u} - \mathbf{v}_h\|_h.$$

Noting $\operatorname{div} \Pi^0_{\mathcal{V}_h} \mathbf{u} = \Pi^0_{\mathcal{Q}_h} \operatorname{div} \mathbf{u} = 0$, we can choose $\mathbf{v}_h = \Pi^0_{\mathcal{V}_h} \mathbf{u}$ in the above expression to obtain

$$\|\mathbf{u} - \mathbf{u}_h\|_h \leq C_{co} \sqrt{T_1 + T_2 + T_3} \tag{87}$$

where we have assigned $C_{co} = (1 + 2\kappa\gamma)$ and

$$T_1 = |\mathbf{u} - \Pi^0_{\mathcal{V}_h} \mathbf{u}|^2_{\mathbf{H}^1(\Omega)} \tag{88}$$

$$T_2 = \sum_{F \in \Gamma_h} h_F \| \left(\nabla^s \left(\mathbf{u} - \Pi^0_{\mathcal{V}_h} \mathbf{u}\right)\right) \mathbf{n}\|^2_{(L^2(F))^d} \tag{89}$$

$$T_3 = \sum_{F \in \Gamma_h} C_{pen} h_F^{-1} \|\mathbf{u} - \Pi^0_{\mathcal{V}_h} \mathbf{u}\|^2_{(L^2(F))^d}. \tag{90}$$

To handle the face integral in (89), we recruit the multiplicative trace inequality for fractional Sobolev spaces [38] and Young's inequality element-wise to obtain the bound

$$\sum_{F \in \Gamma_h} h_F \| \left(\nabla^s \left(\mathbf{u} - \Pi^0_{\mathcal{V}_h} \mathbf{u}\right)\right) \mathbf{n}\|^2_{(L^2(F))^d} \leq$$
$$(C_{trc,1})^2 \sum_{K \in \mathcal{K}_h} \left(|\mathbf{u} - \Pi^0_{\mathcal{V}_h} \mathbf{u}|^2_{\mathbf{H}^1(K)} + h_K^{2q} |\mathbf{u} - \Pi^0_{\mathcal{V}_h} \mathbf{u}|^2_{\mathbf{H}^{q+1}(\Omega)} \right)$$

where $1/2 < q \leq s$ and $C_{trc,1}$ is a positive constant independent of h, ν, and C_{pen}. To handle the face integral in (90), we recruit the standard continuous trace inequality element-wise to obtain the bound

$$\sum_{F \in \Gamma_h} C_{pen} h_F^{-1} \|\mathbf{u} - \Pi^0_{\mathcal{V}_h} \mathbf{u}\|^2_{(L^2(F))^d} \leq$$
$$(C_{trc,2})^2 \sum_{K \in \mathcal{K}_h} \left(h_K^{-2} \|\mathbf{u} - \Pi^0_{\mathcal{V}_h} \mathbf{u}\|^2_{\mathbf{L}^2(K)} + |\mathbf{u} - \Pi^0_{\mathcal{V}_h} \mathbf{u}|^2_{\mathbf{H}^1(K)} \right)$$

where $C_{trc,2}$ is a positive constant independent of h and ν which varies linearly with the square root of C_{pen}. It should be noted the two constants $C_{trc,1}$ and $C_{trc,2}$ necessarily depend on the shape regularity of the mesh family $\{\mathcal{Q}\}_{h\leq h_0}$ and the parametric mapping which together give the shape regularity of the mesh family $\{\mathcal{K}\}_{h\leq h_0}$. See [18] for more details. Inserting the above two inequalities into (87) and then applying Proposition 5.5, we immediately acquire the bound

$$\|\mathbf{u} - \Pi^0_{\mathcal{V}_h}\mathbf{u}\|_h \leq C_{\mathbf{u}} C_{co} h^s \|\mathbf{u}\|_{\mathbf{H}^{s+1}(\Omega)}$$

for $C_{\mathbf{u}}$ a positive constant independent of h and ν with the same functional dependency on the penalty parameter as $C_{trc,2}$.

The proof for (86) is much more immediate. Choosing $q_h = \Pi^0_{\mathcal{Q}_h} p$ in the error estimate given by (75), one obtains

$$\|p - p_h\|_{L^2(\Omega)} \leq \left(1 + \frac{1}{\widetilde{\beta}}\right) \|p - \Pi^0_{\mathcal{Q}_h} p\|_{L^2(\Omega)} + \frac{\kappa}{\widetilde{\beta}} \|\mathbf{u} - \mathbf{u}_h\|_h \tag{91}$$

Inequality (86) follows by an application of Proposition 5.5 to bound the pressure interpolation error. □

Again, to the best of our knowledge, Theorems 6.2 and 6.3 are the first of their kind for $\mathbf{H}^1$ quadrilateral- and hexahedral-based spline finite element discretizations written in divergence-form. Note that we have obtained error estimates which are optimal for the velocity field and suboptimal, by one order, for the pressure field under a smallness condition not unlike that of the continuous problem. In Section 8, we will employ a selection of problems with known analytical solutions to confirm our theoretical convergence rates. Our numerical results will suggest our derived pressure error estimates may be conservative. The analysis presented here also covers singular solutions typically encountered in practice. We also numerically study the effectiveness of our method for a singular test problem, lid-driven cavity flow.

7 Extension to Multi-Patch Domains

As was mentioned previously, most geometries of scientific and engineering interest cannot be represented by a single patch. Instead, the multi-patch concept must be invoked. We assume that there exist n_p sufficiently smooth parametric mappings $\mathbf{F}_i : (0,1)^d \to \mathbb{R}^d$ such that the subdomains

$$\Omega_i = \mathbf{F}_i\left(\widehat{\Omega}\right),\ i = 1, \ldots, n_p$$

are non-overlapping and

$$\overline{\Omega} = \cup_{i=1}^{n_p} \overline{\Omega_i}.$$

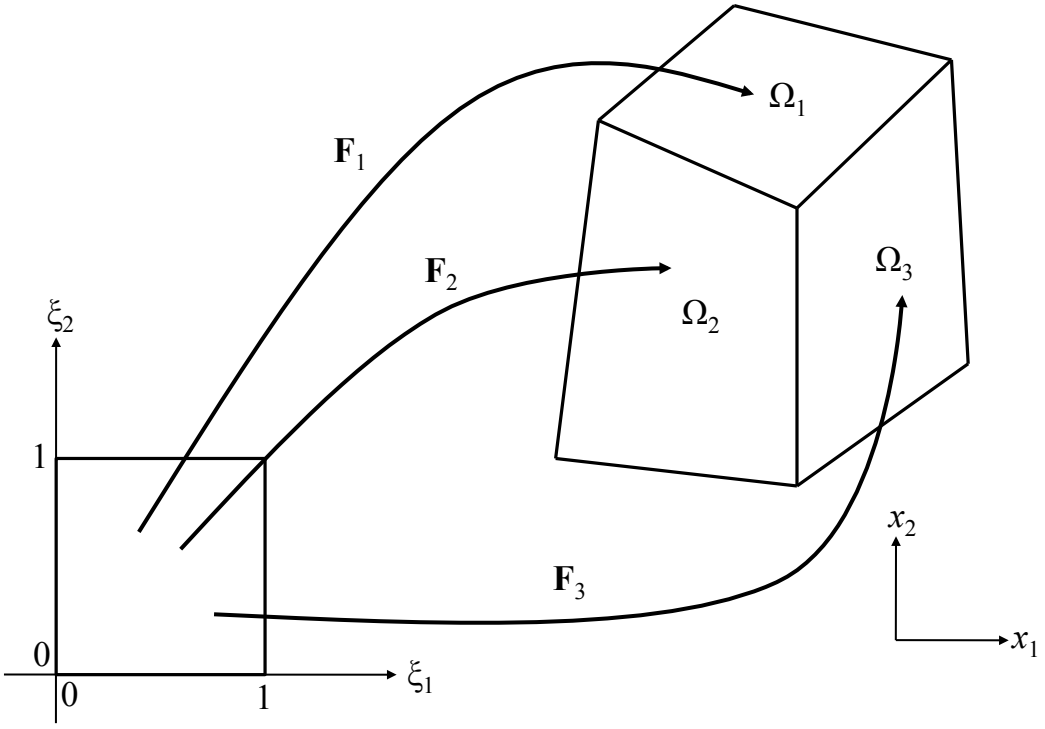

Figure 1: Example multi-patch construction in $\mathbb{R}^2$.

We refer to each subdomain Ω_i (and its pre-image) as a patch. For a visual depiction of a multi-patch construction in $\mathbb{R}^2$, see Figure 1. We build discrete velocity and pressure spaces over each patch Ω_i, $i = 1, \ldots, n_p$ in the same manner as in the previous sections except that we do not yet enforce boundary conditions, and we denote these spaces as $\mathcal{V}_h(\Omega_i)$ and $\mathcal{Q}_h(\Omega_i)$.

To proceed further, we must make some assumptions. First of all, we assume that if two disjoint patches Ω_i and Ω_j have the property that $\partial\Omega_i \cap \partial\Omega_j \neq \emptyset$, then this intersection consists strictly of patch faces, edges, and corners. More succinctly, two patches cannot intersect along an isolated portion of a face (or edge) interior. Second, we assume that the mappings $\{\mathbf{F}_i\}_{i=1}^{n_p}$ are compatible in the following sense: if two patches Ω_i and Ω_j share a face, then $\mathbf{F}_i$ and $\mathbf{F}_j$ parametrize that face identically up to changes in orientation. Third, we assume that if two patches Ω_i and Ω_j share a face, the B-spline meshes associated with the patches are identical along that face. This guarantees our mesh is conforming. Finally, we assume for simplicity that $k_1 = \ldots = k_d = k^*$ for all patches. The mixed polynomial degree case introduces additional complications that are beyond the scope of this work. We would like to note that all four assumptions hold if we employ a conforming NURBS multi-patch construction. See, for example, Chapter 2 of [13].

We define our global discrete velocity and pressure spaces as follows:

$$\mathcal{V}_{0,h} := \{\mathbf{v}_h \in \mathbf{H}_0(\operatorname{div};\Omega) : \mathbf{v}_h|_{\Omega_i} \in \mathcal{V}_h(\Omega_i),\ \forall i = 1,\dots,n_p\}, \tag{92}$$

$$\mathcal{Q}_{0,h} := \left\{q_h \in L_0^2(\Omega) : q_h|_{\Omega_i} \in \mathcal{Q}_h(\Omega_i),\ \forall i = 1,\dots,n_p\right\}. \tag{93}$$

The space $\mathcal{V}_{0,h}$ is easily constructed due to our preceding four assumptions and use of open knot vectors. Specifically, we set to zero the coefficient of any basis function whose normal component is nonzero along $\partial\Omega$, and along shared faces between patches we (i) equivalence the coefficients of any basis functions whose normal components are nonzero and equal in magnitude and direction and (ii) set the coefficient of one to minus the coefficient of another for any basis functions whose normal components are nonzero, equal in magnitude, and opposite in direction. We note that this is precisely the same procedure as is used to construct Raviart-Thomas spaces on conforming finite element meshes. We simply have patches instead of elements. It is easily shown that the spaces $\mathcal{V}_{0,h}$ and $\mathcal{Q}_{0,h}$, along with the divergence operator, form the bounded discrete cochain complex

$$\mathcal{V}_{0,h} \xrightarrow{\text{div}} \mathcal{Q}_{0,h}.$$

However, functions in $\mathcal{V}_{0,h}$ do not necessarily lie in $\mathbf{H}^1(\Omega)$ as tangential continuity is not enforced across patch interfaces. Hence, we need to account for this lack of continuity when designing a discretization scheme for the steady Navier-Stokes equations. We weakly enforce tangential continuity between adjacent patches using a combination of upwinding and the symmetric interior penalty method [1, 15, 39].

We now establish some preliminary notations. Let $\mathcal{K}_h(\Omega_i)$ and $\mathcal{F}_h(\Omega_i)$ denote the sets of physical mesh elements and faces associated with patch Ω_i. We denote the global set of mesh elements as $\mathcal{K}_h$ and the global set of mesh faces as $\mathcal{F}_h$. As in the single patch setting, we define the boundary mesh to be

$$\Gamma_h = \{F \in \mathcal{F}_h(\Omega_i), i = 1,\dots,n_p : F \subset \partial\Omega\}, \tag{94}$$

and we define the interface mesh to be

$$\mathcal{I}_h = \{F \in \mathcal{F}_h(\Omega_i), i = 1,\dots,n_p : F \in \mathcal{F}_h(\Omega_j), i \neq j \text{ and } F \notin \Gamma_h\}. \tag{95}$$

For each face $F \in \mathcal{I}_h$ belonging to the interface mesh, there exist two unique adjacent elements $K^+, K^- \in \mathcal{K}_h$ such that $F \in \partial K^+$ and $F \in \partial K^-$. We define for such a face the mesh size

$$h_F := \frac{1}{2}\left(h_{K^+} + h_{K^-}\right). \tag{96}$$

Let ϕ be an arbitrary scalar-, vector-, or matrix-valued piecewise smooth function, and let us denote by ϕ^+ and ϕ^- the traces of ϕ on F as taken from within the interior of K^+ and K^- respectively. We define the mean value of ϕ at $\mathbf{x} \in F$ as

$$\{\!\{\phi\}\!\} := \frac{1}{2}\left(\phi^+ + \phi^-\right). \tag{97}$$

Further, for a generic multiplication operator $\odot$, we define the jump of $\phi \odot \mathbf{n}$ at $\mathbf{x} \in F$ as

$$[\![\phi \odot \mathbf{n}]\!] := \phi^+ \odot \mathbf{n}_{K^+} + \phi^- \odot \mathbf{n}_{K^-} \tag{98}$$

where $\mathbf{n}_{K^{+/-}}$ denotes the outward facing normal on the boundary $\partial K^{+/-}$ of element $K^{+/-}$.

With the above notation established, let us define the following bilinear form:

$$\begin{aligned} k_h^*(\mathbf{w}, \mathbf{v}) = &\sum_{i=1}^{n_p} (2\nu \nabla^s \mathbf{w}, \nabla^s \mathbf{v})_{(L^2(\Omega_i))^{d\times d}} \\ &- \sum_{F \in \mathcal{I}_h} \int_F 2\nu \left(\{\!\{ \nabla^s \mathbf{v} \}\!\} : [\![\mathbf{w} \otimes \mathbf{n}]\!] + \{\!\{ \nabla^s \mathbf{w} \}\!\} : [\![\mathbf{v} \otimes \mathbf{n}]\!] \right) d\mathbf{s} \\ &+ \sum_{F \in \mathcal{I}_h} \int_F 2\nu \left(\frac{2C_{pen}}{h_F} [\![\mathbf{w} \otimes \mathbf{n}]\!] : [\![\mathbf{v} \otimes \mathbf{n}]\!] \right) d\mathbf{s} \\ &- \sum_{F \in \Gamma_h} \int_F 2\nu \left(((\nabla^s \mathbf{v})\, \mathbf{n}) \cdot \mathbf{w} + ((\nabla^s \mathbf{w})\, \mathbf{n}) \cdot \mathbf{v} - \frac{C_{pen}}{h_F} \mathbf{w} \cdot \mathbf{v} \right) d\mathbf{s}. \end{aligned} \tag{99}$$

Above, $C_{pen} > 0$ denotes the same positive penalty constant as before. We note that the above bilinear form is coercive. Now, for Ω_i an arbitrary patch, let $\mathbf{n}_i$ denote the outward-facing normal with respect to $\partial\Omega_i$. We define the upwind form

$$\begin{aligned} c_h^*(\mathbf{w}, \mathbf{x}; \mathbf{v}) = &\sum_{i=1}^{n_p} - (\mathbf{w} \otimes \mathbf{x}, \nabla \mathbf{v})_{(L^2(\Omega_i))^{d\times d}} \\ &+ \sum_{i=1}^{n_p} \int_{\partial\Omega_i \setminus \partial\Omega} \frac{1}{2} \left(\mathbf{w} \cdot \mathbf{n}_i + |\mathbf{w} \cdot \mathbf{n}_i| \right) \mathbf{u} \cdot \mathbf{v} d\mathbf{s} \\ &+ \sum_{i=1}^{n_p} \int_{\partial\Omega_i \setminus \partial\Omega} \frac{1}{2} \left(\mathbf{w} \cdot \mathbf{n}_i - |\mathbf{w} \cdot \mathbf{n}_i| \right) \mathbf{u}^e \cdot \mathbf{v} d\mathbf{s} \end{aligned}$$

for $\mathbf{w}, \mathbf{x}, \mathrm{v} \in \mathbf{H}_0(\mathrm{div}; \Omega)$ where $\mathbf{u}^e$ is the trace of $\mathbf{u}$ taken from the exterior of Ω_i. We would like to remark that the above form is nonlinear in $\mathbf{w}$. Furthermore, the form satisfies the semi-coercivity result $c_h^*(\mathbf{w}, \mathbf{v}; \mathbf{v}) \geq 0$, and $c_h^*(\mathbf{w}, \mathbf{x}; \mathbf{v}) = 0$ for constant vector-valued functions $\mathbf{v} : \Omega \to \mathbb{R}^d$. Hence, the upwind form is conservative.

With all the preceding terminology defined, our discrete multi-patch formulation reads as follows.

$$(MP) \begin{cases} \text{Find } \mathbf{u}_h \in \mathcal{V}_{0,h} \text{ and } p_h \in \mathcal{Q}_{0,h} \text{ such that} \\ \qquad k_h^*(\mathbf{u}_h, \mathbf{v}_h) + c^*(\mathbf{u}_h, \mathbf{u}_h; \mathbf{v}_h) - b(p_h, \mathbf{v}_h) + b(q_h, \mathbf{u}_h) = (\mathbf{f}, \mathbf{v}_h)_{\mathbf{L}^2(\Omega)} \\ \text{for all } \mathbf{v}_h \in \mathcal{V}_{0,h} \text{ and } q_h \in \mathcal{Q}_{0,h}. \end{cases} \tag{100}$$

As in the single patch setting, the discrete formulation detailed above returns a pointwise divergence-free velocity field. Furthermore, the discrete formulation is consistent. However, we do not yet have a convergence analysis available. We anticipate such a convergence analysis will take new theoretical developments. Nonetheless, we have utilized the above formulation in practice and observed it produces optimal convergence rates for both velocity and pressure fields.

8 Numerical Verification of Convergence Estimates

In this section, we numerically verify our convergence estimates using a collection of problems with exact solutions. Throughout, we choose Nitsche's penalty constant as

$$C_{pen} = 5(k' + 1)$$

which we have found to be sufficiently large in order to ensure numerical stability. Additionally, we employ uniform parametric meshes, linear parametric mappings, and B-spline spaces of maximal continuity.

8.1 Two-dimensional Manufactured Solution

As a first numerical experiment, we consider a two-dimensional manufactured vortex solution that was originally presented in [8]. Let

$$\Omega \equiv (0,1)^2$$

and

$$\mathbf{f} \equiv \nabla \cdot (\bar{\mathbf{u}} \otimes \bar{\mathbf{u}}) - \nabla \cdot (2\nu \nabla^s \bar{\mathbf{u}}) + \nabla \bar{p}$$

with

$$\bar{\mathbf{u}} = \begin{bmatrix} 2e^x(-1+x)^2x^2(y^2-y)(-1+2y) \\ (-e^x(-1+x)x(-2+x(3+x))(-1+y)^2y^2) \end{bmatrix}$$

and

$$\begin{aligned} \bar{p} \;=\; & (-424 + 156e + (y^2-y)(-456 + e^x(456 + x^2(228 - 5(y^2-y)) + \\ & 2x(-228 + (y^2-y)) + 2x^3(-36 + (y^2-y)) + x^4(12 + (y^2-y))))). \end{aligned}$$

Homogeneous boundary conditions are applied along the boundary $\partial\Omega$, and the condition $\int_\Omega p d\mathbf{x} = 0$ is enforced. A solution to the steady Navier-Stokes problem with the prescribed forcing is then clearly $(\mathbf{u}, p) = (\bar{\mathbf{u}}, \bar{p})$, and this solution is unique provided a smallness condition is satisfied. The streamlines and pressure contours associated with the solution are plotted in Figure 2.

To confirm our theoretically derived error estimates, we have computed convergence rates for divergence-conforming B-spline discretizations of varying mesh size and

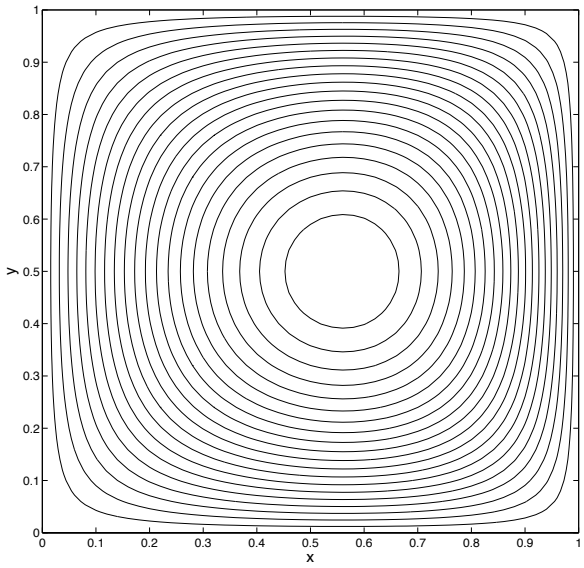

(a)

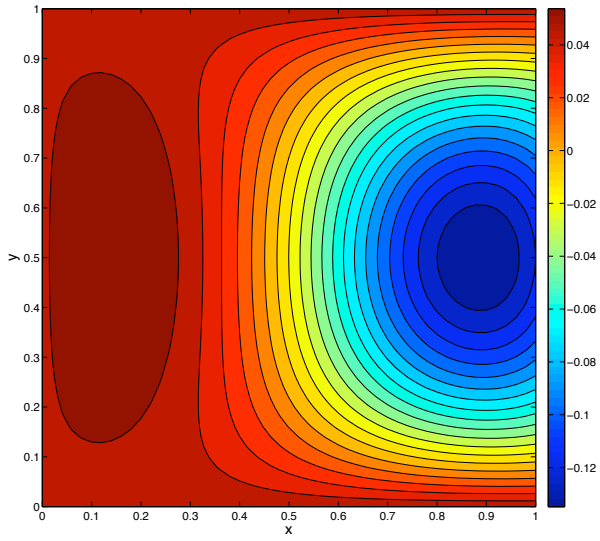

(b)

Figure 2: Vortex manufactured solution in 2-D: (a) Flow velocity streamlines, (b) Pressure contours.

Table 1: Steady vortex flow convergence rates in 2-D: $Re = 1$

Polynomial degree $k' = 1$

h	1/4	1/8	1/16	1/32	1/64
$\|\mathbf{u} - \mathbf{u}_h\|_h$	5.48e-2	2.80e-2	1.40e-2	7.00e-3	3.50e-3
order	-	0.97	1.00	1.00	1.00
$\|\mathbf{u} - \mathbf{u}_h\|_{\mathbf{H}^1(\Omega)}$	5.48e-2	2.80e-2	1.40e-2	7.00e-3	3.50e-3
order	-	0.97	1.00	1.00	1.00
$\|\mathbf{u} - \mathbf{u}_h\|_{\mathbf{L}^2(\Omega)}$	2.77e-3	8.16e-4	2.28e-4	6.10e-5	1.58e-5
order	-	1.76	1.84	1.90	1.95
$\|p - p_h\|_{L^2(\Omega)}$	5.04e-3	1.38e-3	3.49e-4	8.72e-5	2.18e-5
order	-	1.87	1.98	2.00	2.00

Polynomial degree $k' = 2$

h	1/4	1/8	1/16	1/32	1/64
$\|\mathbf{u} - \mathbf{u}_h\|_h$	9.71e-3	2.33e-3	5.68e-4	1.40e-4	3.48e-5
order	-	2.06	2.04	2.02	2.01
$\|\mathbf{u} - \mathbf{u}_h\|_{\mathbf{H}^1(\Omega)}$	9.70e-3	2.33e-3	5.68e-4	1.40e-4	3.48e-5
order	-	2.06	2.04	2.02	2.01
$\|\mathbf{u} - \mathbf{u}_h\|_{\mathbf{L}^2(\Omega)}$	2.94e-4	3.84e-5	5.03e-6	6.47e-7	8.21e-8
order	-	2.94	2.93	2.96	2.98
$\|p - p_h\|_{L^2(\Omega)}$	1.08e-3	1.12e-4	1.17e-5	1.19e-6	1.27e-7
order	-	3.40	3.26	3.30	3.23

Polynomial degree $k' = 3$

h	1/4	1/8	1/16	1/32	1/64
$\|\mathbf{u} - \mathbf{u}_h\|_h$	9.86e-4	1.28e-4	1.66e-5	2.13e-6	2.72e-7
order	-	2.95	2.95	2.96	2.97
$\|\mathbf{u} - \mathbf{u}_h\|_{\mathbf{H}^1(\Omega)}$	9.83e-4	1.28e-4	1.65e-5	2.10e-6	2.66e-7
order	-	2.94	2.96	2.97	2.98
$\|\mathbf{u} - \mathbf{u}_h\|_{\mathbf{L}^2(\Omega)}$	3.05e-5	2.34e-6	1.59e-7	1.03e-8	6.55e-10
order	-	3.70	3.88	3.95	3.98
$\|p - p_h\|_{L^2(\Omega)}$	1.10e-4	5.64e-6	3.45e-7	2.19e-8	1.39e-9
order	-	4.29	4.03	3.98	3.98

Table 2: Robustness of 2-D divergence-free B-spline discretizations for increasing Re

Polynomial degree $k' = 1$, $h = 1/16$

Re	0	1	10	100	1000	10000
$\|\mathbf{u} - \mathbf{u}_h\|_h$	1.40e-2	1.40e-2	1.40e-2	1.40e-2	1.40e-2	1.40e-2
$\|\mathbf{u} - \mathbf{u}_h\|_{\mathbf{H}^1(\Omega)}$	1.40e-2	1.40e-2	1.40e-2	1.40e-2	1.40e-2	1.40e-2
$\|\mathbf{u} - \mathbf{u}_h\|_{\mathbf{L}^2(\Omega)}$	2.28e-4	2.28e-4	2.28e-4	2.28e-4	2.28e-4	2.28e-4
$\|p - p_h\|_{L^2(\Omega)}$	3.49e-4	3.49e-4	1.98e-4	1.96e-4	1.96e-4	1.96e-4

Polynomial degree $k' = 2$, $h = 1/16$

Re	0	1	10	100	1000	10000
$\|\mathbf{u} - \mathbf{u}_h\|_h$	5.68e-4	5.68e-4	5.68e-4	5.68e-4	5.68e-4	5.68e-4
$\|\mathbf{u} - \mathbf{u}_h\|_{\mathbf{H}^1(\Omega)}$	5.68e-4	5.68e-4	5.68e-4	5.68e-4	5.68e-4	5.68e-4
$\|\mathbf{u} - \mathbf{u}_h\|_{\mathbf{L}^2(\Omega)}$	5.03e-6	5.03e-6	5.03e-6	5.03e-6	5.03e-6	5.03e-6
$\|p - p_h\|_{L^2(\Omega)}$	1.17e-5	1.17e-5	6.50e-6	6.42e-4	6.42e-6	6.42e-6

Polynomial degree $k' = 3$, $h = 1/16$

Re	0	1	10	100	1000	10000
$\|\mathbf{u} - \mathbf{u}_h\|_h$	1.66e-5	1.66e-5	1.66e-5	1.66e-5	1.66e-5	1.66e-5
$\|\mathbf{u} - \mathbf{u}_h\|_{\mathbf{H}^1(\Omega)}$	1.66e-5	1.66e-5	1.66e-5	1.66e-5	1.66e-5	1.66e-5
$\|\mathbf{u} - \mathbf{u}_h\|_{\mathbf{L}^2(\Omega)}$	1.59e-7	1.59e-7	1.59e-7	1.59e-7	1.59e-7	1.59e-7
$\|p - p_h\|_{L^2(\Omega)}$	3.45e-7	3.45e-7	3.19e-7	3.19e-7	3.19e-7	3.19e-7

Table 3: Instability of conservative 2-D Taylor-Hood discretizations for increasing Re

$\mathbf{Q}_2/Q_1$ velocity/pressure pair, $h = 1/16$

Re	0	1	10	100	1000	10000
$\|\mathbf{u} - \mathbf{u}_h\|_{\mathbf{H}^1(\Omega)}$	6.78e-4	6.78e-4	7.11e-4	2.26e-3	2.16e-2	2.16e-1
$\|\mathbf{u} - \mathbf{u}_h\|_{\mathbf{L}^2(\Omega)}$	6.54e-6	6.54e-6	6.79e-6	1.97e-5	1.86e-4	2.35e-3
$\|p - p_h\|_{L^2(\Omega)}$	1.96e-4	1.96e-4	1.96e-4	1.96e-4	1.96e-4	1.96e-4

polynomial degree. Furthermore, we have computed rates for a variety of Reynolds numbers

$$Re = \frac{UL}{\nu}$$

where U is a velocity scale parameter and L is a length scale parameter. We take $U = 1$ and $L = 1$. In Table 1, we have plotted our numerically computed convergence rates for $Re = 1$. First, note that our theoretically derived error estimates are confirmed. Second, note that the L^2-norm of the pressure error optimally converges like $O(h^{k'+1})$, which is an improvement over our theoretically derived estimate. Third, note that the results in Table 1 are identical to the Stokes results appearing in Table 2 of [19]. Hence, the introduction of convection has not affected our numerical error.

While our theoretically derived error estimates only cover flows with "small" Reynolds number (and indeed uniqueness is only guaranteed under a smallness condition), we have investigated the effectiveness of our discretization for larger Reynolds number flows and the two-dimensional forcing prescribed above. To compute these flow solutions, we used a Newton-Raphson nonlinear solver in conjunction with continuation. The results of this investigation are included in Table 2 for meshes with 16×16 elements. Note that the velocity numerical errors in the tables appear independent of the Reynolds number. Moreover, the pressure numerical errors seem to improve with increasing Reynolds number. Hence, we are able to recover the desired flow solution $(\mathbf{u}, p)$ for large Reynolds numbers. This observation attests to the enhanced stability properties of our discretization for nonlinear flow problems even in the absence of any external stabilization mechanisms. To contrast our methodology with standard mixed finite element discretizations, we have repeated the above computations for conservative Taylor-Hood [24] finite element approximations, using again a continuation method in conjunction with a Newton-Raphson nonlinear solver. The results of these computations are included in Table 3. Note that while the pressure error is well-behaved, the velocity error diverges with increasing Reynolds number. We believe that this divergence is inherently tied to the fact the Taylor-Hood approximations only satisfy the divergence-free constraint approximately.

8.2 Three-dimensional Manufactured Solution

As a second numerical experiment, we consider a three-dimensional manufactured solution representing a single vortical filament. Let

$$\Omega \equiv (0,1)^3$$

and

$$\mathbf{f} \equiv \nabla \cdot (\bar{\mathbf{u}} \otimes \bar{\mathbf{u}}) - \nabla \cdot (2\nu \nabla^s \bar{\mathbf{u}}) + \nabla \bar{p}$$

with

$$\bar{\mathbf{u}} = \mathbf{curl}\, \bar{\boldsymbol{\phi}},$$

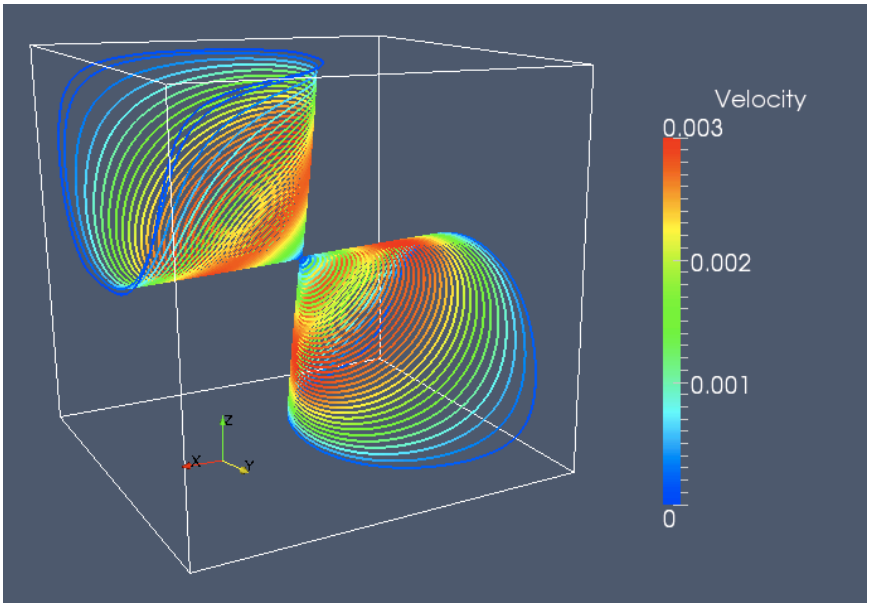

Figure 3: Vortex manufactured solution in 3-D: Flow velocity streamlines colored by velocity magnitude.

$$\bar{\boldsymbol{\phi}} = \begin{bmatrix} x(x-1)y^2(y-1)^2z^2(z-1)^2 \\ 0 \\ x^2(x-1)^2y^2(y-1)^2z(z-1) \end{bmatrix},$$

and

$$\bar{p} = \sin(\pi x)\sin(\pi y) - \frac{4}{\pi^2}.$$

Again, homogeneous boundary conditions are applied along the boundary $\partial\Omega$, and the pressure is enforced to satisfy $\int_\Omega p d\mathbf{x} = 0$. A solution to the steady Navier-Stokes equations with the prescribed forcing is then clearly $(\mathbf{u}, p) = (\bar{\mathbf{u}}, \bar{p})$, and for sufficiently small data, this solution is unique. Streamlines associated with the exact solution are plotted in Figure 3.

For $Re = 1$ flow (with $Re = 1/\nu$), we have computed convergence rates for divergence-conforming B-spline discretizations of varying mesh size and polynomial degree. In Table 4, we have listed our numerically computed convergence rates. First, note that our theoretically derived error estimates are confirmed. Second, note that the L^2-norm of the pressure error optimally converges like $O(h^{k'+1})$, which is an improvement over our theoretically derived estimate. Third, note that, as in the two-dimensional setting, the results in Table 4 are identical to the Stokes results appearing in Table 5 of [19]. Hence, the introduction of convection has not affected our numerical error.

Again, while our theoretically derived error estimates only cover flows with "small" Reynolds number, we have investigated the effectiveness of our discretization for larger

Table 4: Steady vortex flow convergence rates in 3-D: $Re = 1$.

Polynomial degree $k' = 1$

h	1/2	1/4	1/8	1/16	1/32
$\|\mathbf{u} - \mathbf{u}_h\|_h$	1.83e-2	8.98e-3	4.18e-3	1.99e-3	9.62e-4
order	-	1.03	1.10	1.07	1.05
$\|\mathbf{u} - \mathbf{u}_h\|_{\mathbf{H}^1(\Omega)}$	1.51e-2	7.64e-3	3.77e-3	1.87e-3	9.34e-4
order	-	0.98	1.02	1.01	1.00
$\|\mathbf{u} - \mathbf{u}_h\|_{\mathbf{L}^2(\Omega)}$	1.35e-3	3.68-4	1.03e-4	2.81e-5	7.40e-6
order	-	1.88	1.84	1.87	1.93
$\|p - p_h\|_{L^2(\Omega)}$	5.41e-2	1.48e-2	3.58e-3	8.85e-4	2.26e-4
order	-	1.87	2.05	2.02	1.97

Polynomial degree $k' = 2$

h	1/2	1/4	1/8	1/16	1/32
$\|\mathbf{u} - \mathbf{u}_h\|_h$	6.50e-3	1.54e-3	4.10e-4	9.51e-5	2.15e-5
order	-	2.08	1.91	2.11	2.15
$\|\mathbf{u} - \mathbf{u}_h\|_{\mathbf{H}^1(\Omega)}$	3.71e-3	9.90e-4	2.79e-4	6.59e-5	1.50e-5
order	-	1.91	1.83	2.08	2.14
$\|\mathbf{u} - \mathbf{u}_h\|_{\mathbf{L}^2(\Omega)}$	1.97e-4	4.25e-5	7.38e-6	8.67e-7	9.18e-8
order	-	2.21	2.53	3.09	3.23
$\|p - p_h\|_{L^2(\Omega)}$	1.50e-2	1.59e-3	2.00e-4	2.56e-5	3.26e-6
order	-	3.24	2.99	2.97	2.97

Table 5: Robustness of 3-D divergence-free B-spline discretizations for increasing Re

Polynomial degree $k' = 1$, $h = 1/16$

Re	0	1	10	100	1000	10000
$\|\mathbf{u} - \mathbf{u}_h\|_h$	1.99e-3	1.99e-3	1.99e-3	1.99e-3	1.99e-3	1.99e-3
$\|\mathbf{u} - \mathbf{u}_h\|_{\mathbf{H}^1(\Omega)}$	1.87e-3	1.87e-3	1.87e-3	1.87e-3	1.87e-3	1.87e-3
$\|\mathbf{u} - \mathbf{u}_h\|_{\mathbf{L}^2(\Omega)}$	2.81e-5	2.81e-5	2.81e-5	2.81e-5	2.81e-5	2.81e-5
$\|p - p_h\|_{L^2(\Omega)}$	8.84e-4	8.84e-4	8.84e-4	8.84e-4	8.84e-4	8.84e-4

Polynomial degree $k' = 2$, $h = 1/16$

Re	0	1	10	100	1000	10000
$\|\mathbf{u} - \mathbf{u}_h\|_h$	9.51e-5	9.51e-5	9.51e-5	9.51e-5	9.51e-5	9.51e-5
$\|\mathbf{u} - \mathbf{u}_h\|_{\mathbf{H}^1(\Omega)}$	6.59e-5	6.59e-5	6.59e-5	6.59e-5	6.59e-5	6.59e-5
$\|\mathbf{u} - \mathbf{u}_h\|_{\mathbf{L}^2(\Omega)}$	8.67e-7	8.67e-7	8.67e-7	8.67e-7	8.67e-7	8.67e-7
$\|p - p_h\|_{L^2(\Omega)}$	2.56e-5	2.56e-5	2.56e-5	2.56e-5	2.56e-5	2.56e-5

Reynolds number flows and the three-dimensional forcing prescribed above. We used a Newton-Raphson nonlinear solver in conjunction with continuation. The results of this investigation are included in Table 5 for meshes with $16 \times 16 \times 16$ elements. Note that the velocity and pressure numerical errors appearing in the tables are independent of the Reynolds number. Hence, we are able to recover the desired flow solution $(\mathbf{u}, p)$ for large Reynolds numbers.

8.3 Kovasznay Flow

As a third numerical experiment, we consider Kovasznay flow. Kovasznay flow refers to the flow behind an infinite two-dimensional grid, and it is often utilized as a convergence test for Navier-Stokes discretizations. The flow pattern is periodic and can be analytically derived [27]. Indeed, denoting $Re = \frac{1}{\nu}$, the flow solution satisfies

$$\mathbf{u} = \begin{bmatrix} 1 - e^{\lambda x}\cos(2\pi y) \\ \frac{\lambda}{2\pi} e^{\lambda x}\cos(2\pi y). \end{bmatrix}$$

and

$$p = \tfrac{1-e^{2\lambda x}}{2}.$$

where

$$\lambda = \frac{\mathrm{Re}}{2} - \sqrt{\frac{\mathrm{Re}^2}{4} + 4\pi^2}.$$

The streamlines and pressure contours associated with the Kovasznay flow solution at $Re = 40$ are plotted in Figure 4. Note that the streamlines closely resemble the streamlines associated with steady flow behind a cylinder.

To solve the Kovasznay flow problem numerically, we restrict ourselves to the domain $\Omega = (0, 1) \times (-1/2, 1/2)$. On the left, bottom, and top sides of the domain, we enforce Dirichlet boundary conditions. On the right side of the domain, we enforce a traction boundary condition. On the interior of the domain, we apply the usual forcing

$$\mathbf{f} \equiv \nabla \cdot (\mathbf{u} \otimes \mathbf{u}) - \nabla \cdot (2\nu \nabla^s \mathbf{u}) + \nabla p.$$

We have computed $Re = 40$ flow convergence rates for a variety of divergence-conforming B-spline discretizations. These rates are summarized in Table 6. Note that the convergence rates are approaching the optimal rates as $h \to 0$ for both the velocity and pressure field. However, it is apparent that even for $h = 1/64$ our computations still lie in the pre-asymptotic range.

8.4 Cylindrical Couette Flow

As a final convergence-rate experiment, we consider cylindrical Couette flow. Couette flow is often used as a "sanity check" for Navier-Stokes discretizations. Cylindrical

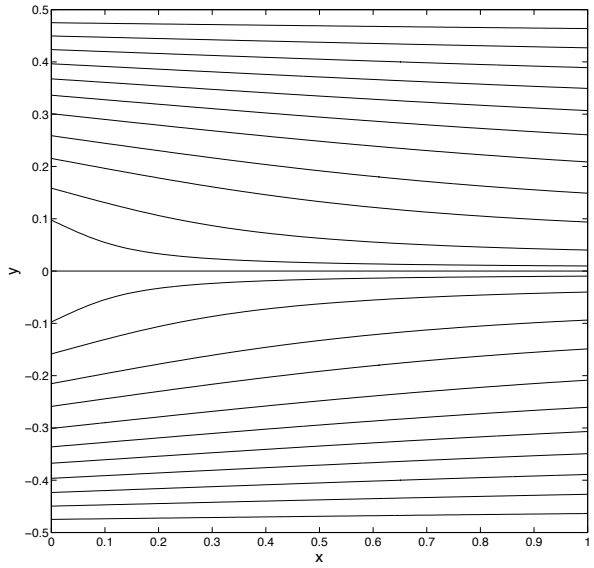

(a)

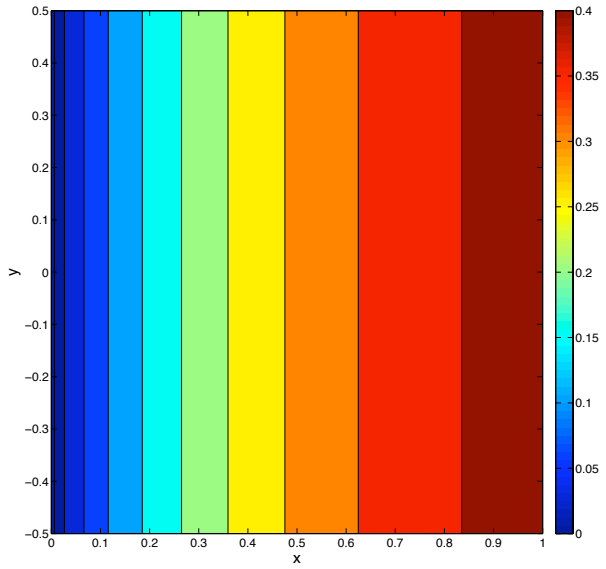

(b)

Figure 4: Steady Kovasznay flow: (a) Streamlines for $Re = 40$, (b) Pressure contours for $Re = 40$.

Table 6: Steady Kovasznay flow convergence rates: $Re = 40$

Polynomial degree $k' = 1$

h	1/4	1/8	1/16	1/32	1/64
$\lvert\mathbf{u} - \mathbf{u}_h\rvert_{\mathbf{H}^1(\Omega)}$	1.39e0	7.31e-1	3.69e-1	1.84e-1	9.19e-2
order	-	0.93	0.99	1.00	1.00
$\lVert\mathbf{u} - \mathbf{u}_h\rVert_{\mathbf{L}^2(\Omega)}$	5.31e-2	1.98e-2	6.78e-3	2.15e-3	6.34e-4
order	-	1.43	1.54	1.66	1.76
$\lVert p - p_h\rVert_{L^2(\Omega)}$	3.98e-2	1.49e-2	4.73e-3	1.35e-3	3.75e-4
order	-	1.42	1.65	1.81	1.85

Polynomial degree $k' = 2$

h	1/4	1/8	1/16	1/32	1/64
$\lvert\mathbf{u} - \mathbf{u}_h\rvert_{\mathbf{H}^1(\Omega)}$	4.59e-1	1.17e-1	2.78e-2	6.69e-3	1.64e-3
order	-	1.97	2.08	2.05	2.03
$\lVert\mathbf{u} - \mathbf{u}_h\rVert_{\mathbf{L}^2(\Omega)}$	1.44e-2	1.96e-3	2.41e-4	3.04e-5	2.83e-6
order	-	2.88	3.02	2.99	2.99
$\lVert p - p_h\rVert_{L^2(\Omega)}$	1.65e-2	3.55e-3	5.14e-4	7.05e-5	9.56e-6
order	-	2.22	2.79	2.87	2.88

Polynomial degree $k' = 3$

h	1/4	1/8	1/16	1/32	1/64
$\lvert\mathbf{u} - \mathbf{u}_h\rvert_{\mathbf{H}^1(\Omega)}$	1.29e-1	1.52e-2	1.94e-3	2.55e-4	3.31e-5
order	-	3.08	2.98	2.92	2.95
$\lVert\mathbf{u} - \mathbf{u}_h\rVert_{\mathbf{L}^2(\Omega)}$	2.95e-3	1.97e-4	1.64e-5	1.20e-6	8.51e-8
order	-	3.91	3.59	3.77	3.81
$\lVert p - p_h\rVert_{L^2(\Omega)}$	5.59e-3	6.48e-4	5.75e-5	5.28e-6	4.00e-7
order	-	3.11	3.49	3.45	3.72

Couette flow is a more realistic problem which describes the flow between two concentric rotating cylinders. Here, we consider flow between a fixed outer cylinder and a rotating inner cylinder. The problem setup is illustrated in Figure 5(a). No external forcing is applied. The velocity field for this flow assumes the form

$$\mathbf{u} = \begin{bmatrix} u_\theta(r)\sin(\theta) \\ u_\theta(r)\cos(\theta) \end{bmatrix}$$

where

$$u_\theta(r) = Ar + \frac{B}{r},$$

(r, θ) are polar coordinates with respect to the center of the cylinders, and

$$A = -\Omega_{in}\frac{\delta^2}{1-\delta^2}, \quad B = \Omega_{in}\frac{r_{in}^2}{(1-\delta^2)}, \quad \Omega_{in} = \frac{U}{r_{in}}, \quad \delta = \frac{r_{in}}{r_{out}}.$$

We have depicted this velocity field in Figure 5(b). The pressure field for cylindrical Couette flow is axisymmetric and satisfies the differential equation

$$\frac{\partial p(r)}{\partial r} = \frac{u_\theta(r)^2}{r}. \tag{101}$$

The above differential equation coupled with the constraint

$$\int_\Omega p d\mathbf{x} = 0$$

determines the pressure field uniquely. In what follows, we assume $r_{in} = 1$, $r_{out} = 2$, and $U = 1$.

We have computed convergence rates for a variety of divergence-conforming B-spline discretizations and for $Re = 40$. To represent the annular domain in our computations, we employed the polar mapping

$$\mathbf{F}(\xi_1, \xi_2) = \begin{bmatrix} ((r_{out} - r_{in})\xi_2 + r_{in})\sin(2\pi\xi_1) \\ ((r_{out} - r_{in})\xi_2 + r_{in})\cos(2\pi\xi_1) \end{bmatrix}, \forall (\xi_1, \xi_2) \in (0,1)^2 \tag{102}$$

and periodic B-splines of maximal continuity in the ξ_1-direction (see Section 2 of [17]). It should be emphasized that we do not use the polar form of the steady Navier-Stokes equations. Rather, we utilize the polar mapping to define our divergence-conforming B-splines in physical space and then employ the Cartesian-based variational formulation discussed in this chapter. The results of our computations are summarized in Table 7. Note from the table that all of our theoretically derived error estimates are confirmed. Furthermore, we have obtained axisymmetric velocity fields with zero radial components, and the discrete pressure field converges at optimal order. We have additionally simulated the cylindrical Couette flow problem using a multi-patch NURBS construction (see Subsection 8.4 of [19]) and obtained identical discrete velocity fields and slightly differing (yet still optimally convergent) discrete pressure fields.

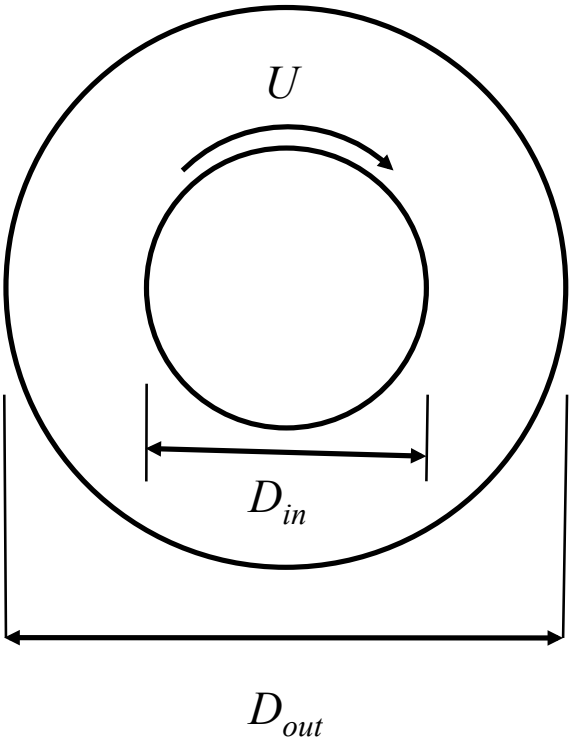

(a)

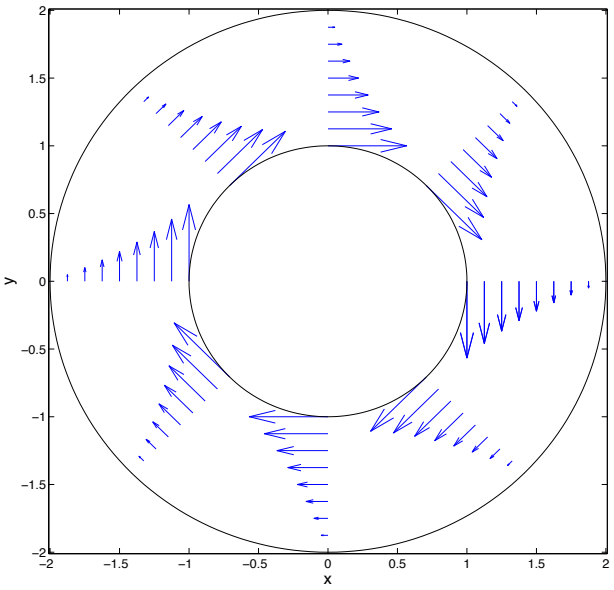

(b)

Figure 5: Cylindrical Couette flow: (a) Problem setup, (b) Flow velocity arrows.

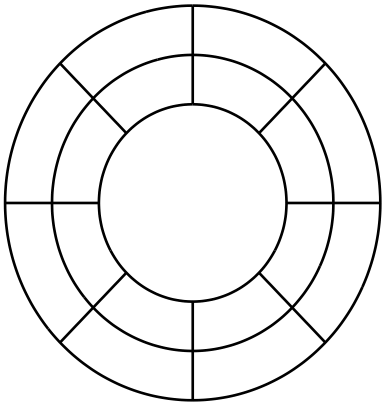

$h/h_0 = 1/2$

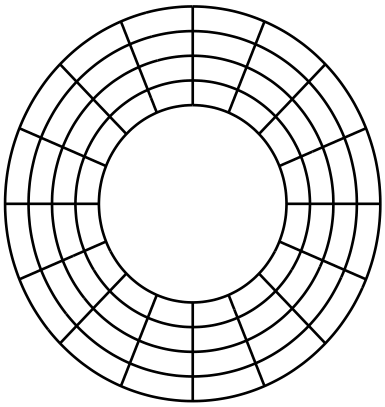

$h/h_0 = 1/4$

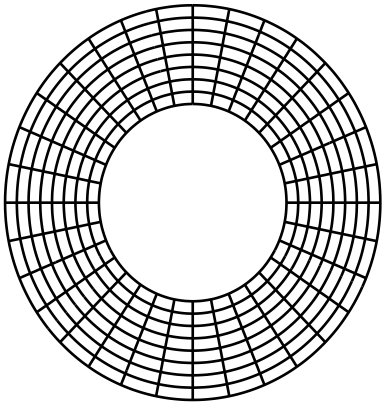

$h/h_0 = 1/8$

Figure 6: Cylindrical Couette flow: Sequence of polar meshes.

Table 7: Cylindrical Couette flow convergence rates: $Re = 40$

Polynomial degree $k' = 1$

h/h_0	1/2	1/4	1/8	1/16	1/32
$\|\mathbf{u} - \mathbf{u}_h\|_h$	5.42e-1	2.63e-1	1.26e-1	6.12e-2	2.99e-2
order	-	1.04	1.06	1.04	1.03
$\|\mathbf{u} - \mathbf{u}_h\|_{\mathbf{H}^1(\Omega)}$	4.48e-1	2.32e-1	1.17e-1	5.86e-2	2.93e-2
order	-	0.95	0.99	1.00	1.00
$\|\mathbf{u} - \mathbf{u}_h\|_{\mathbf{L}^2(\Omega)}$	5.00e-2	1.53-2	4.28e-3	1.14e-3	2.94e-4
order	-	1.71	1.84	1.91	1.96
$\|p - p_h\|_{L^2(\Omega)}$	2.36e-2	6.32e-3	1.62e-3	4.10e-4	1.03e-4
order	-	1.90	1.96	1.98	1.99
$\|u_r - (u_r)_h\|_{L^2(\Omega)}$	0	0	0	0	0

Polynomial degree $k' = 2$

h/h_0	1/2	1/4	1/8	1/16	1/32
$\|\mathbf{u} - \mathbf{u}_h\|_h$	9.77e-2	2.42e-2	5.64e-3	1.32e-3	3.14e-4
order	-	2.01	2.10	2.10	2.07
$\|\mathbf{u} - \mathbf{u}_h\|_{\mathbf{H}^1(\Omega)}$	7.68e-2	2.00e-2	4.92e-3	1.21e-3	2.99e-4
order	-	1.94	2.02	2.02	2.02
$\|\mathbf{u} - \mathbf{u}_h\|_{\mathbf{L}^2(\Omega)}$	4.43e-3	6.03e-4	8.13e-5	1.07e-5	1.38e-6
order	-	2.88	2.89	2.93	2.95
$\|p - p_h\|_{L^2(\Omega)}$	3.14e-3	4.46e-4	6.15e-5	8.23e-6	1.07e-6
order	-	2.82	2.86	2.90	2.94
$\|u_r - (u_r)_h\|_{L^2(\Omega)}$	0	0	0	0	0

Polynomial degree $k' = 3$

h/h_0	1/2	1/4	1/8	1/16	1/32
$\|\mathbf{u} - \mathbf{u}_h\|_h$	2.01e-2	2.67e-3	3.27e-4	4.01e-5	4.98e-6
order	-	2.91	3.03	3.03	3.01
$\|\mathbf{u} - \mathbf{u}_h\|_{\mathbf{H}^1(\Omega)}$	1.52e-2	2.13e-3	2.84e-4	3.72e-5	4.80e-6
order	-	2.84	2.91	2.93	2.95
$\|\mathbf{u} - \mathbf{u}_h\|_{\mathbf{L}^2(\Omega)}$	6.59e-4	5.69e-5	4.82e-6	3.50e-7	2.33e-8
order	-	3.53	3.56	3.78	3.91
$\|p - p_h\|_{L^2(\Omega)}$	3.86e-4	3.41e-5	2.98e-6	2.23e-7	1.51e-8
order	-	3.50	3.52	3.74	3.88
$\|u_r - (u_r)_h\|_{L^2(\Omega)}$	0	0	0	0	0

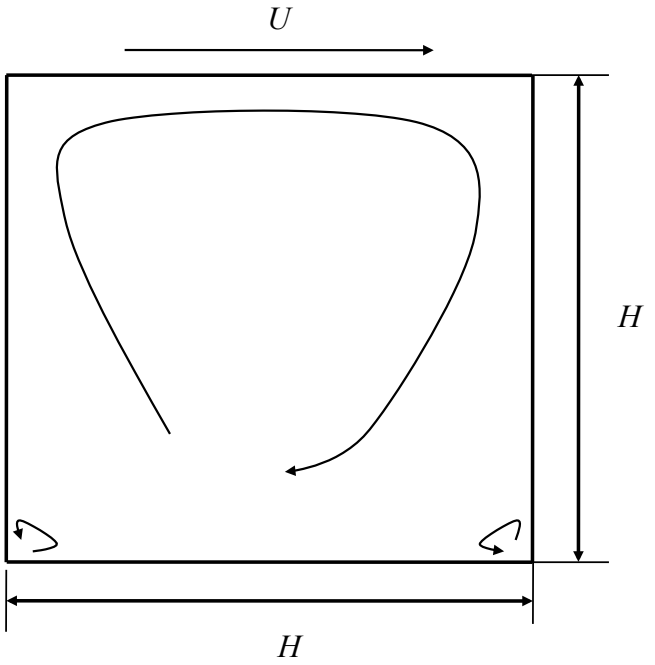

Figure 7: Lid-driven flow in a two-dimensional cavity: Problem setup.

9 Benchmark Problems

In this section, we investigate the effectiveness of our methodology as applied to two benchmark problems: two-dimensional lid-driven cavity flow and confined jet impingement. As previously, we choose Nitsche's penalty constant as $C_{pen} = 5(k'+1)$ for all of the following examples, and we employ uniform parametric meshes, linear parametric mappings, and B-spline spaces of maximal continuity.

9.1 Two-dimensional Lid-driven Cavity Flow

Two-dimensional lid-driven cavity flow is widely considered to be one of the classical test problems for the validation of numerical discretizations for incompressible flow simulation. In the presence of increasing Reynolds number, lid-driven cavity flow loses its symmetry and eventually becomes unsteady. The problem setup for lid-driven cavity flow is shown in Figure 7. For the computations here, H and U are defined to be 1. The Reynolds number associated with the flow is defined to be

$$Re = \frac{UH}{\nu}.$$

The left, right, and bottom sides of the cavity are fixed no-slip walls while the top side of the cavity is a wall which slides to the right with velocity magnitude U. The

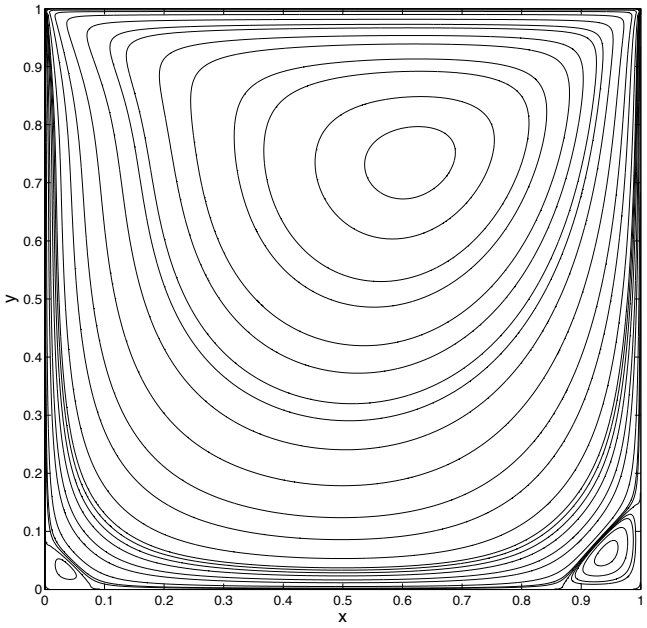

Figure 8: Lid-driven cavity flow: Streamlines for $Re = 100$.

forcing $\mathbf{f}$ is defined to be zero. The pressure and stress fields associated with this flow experience corner singularities which impede the convergence of numerical methods and expose unstable velocity/pressure pairs. Furthermore, the velocity boundary condition is discontinuous at the upper left and right corners of the domain. In classical finite element analysis, this boundary condition must be replaced with an approximate "smooth" boundary condition. Here, as the prescribed slip boundary condition is weakly enforced, we do not have to invoke such an approximation and can instead directly utilize the discontinuous boundary condition.

We have numerically simulated lid-driven cavity flow at $Re = 100$, $Re = 400$, and $Re = 1000$ using a variety of divergence-conforming B-spline discretizations. Streamlines computed using a mesh of degree $k' = 1$ and size $h = 1/128$ are plotted in Figures 8, 9, and 10 for $Re = 100$, $Re = 400$, and $Re = 1000$, respectively. These computed streamlines are visually indistinguishable from benchmark streamlines appearing in the literature.

We have compared our numerical results with the classical benchmark results of Ghia *et al.* [21] for three different polynomial degrees ($k' = 1$, $k' = 2$, $k' = 3$), three different mesh sizes ($h = 1/32$, $h = 1/64$, and $h = 1/128$), and the selected Reynolds numbers. The results of Ghia were obtained using a second-order upwind finite difference method on a stretched mesh with 129^2 grid points. In Figures 11(a), 12(a), and 13(a), we have compared our $k' = 1$, $Re = 100$ values for the horizontal

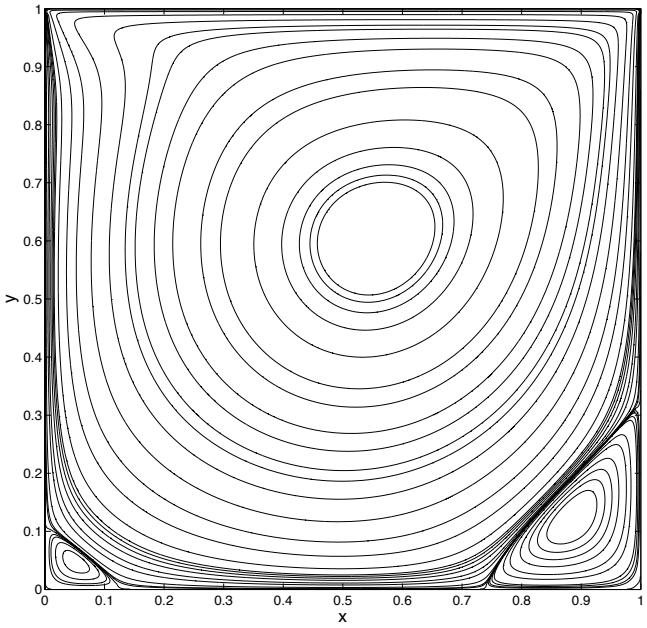

Figure 9: Lid-driven cavity flow: Streamlines for $Re = 400$.

component of the velocity field along the vertical center line with those of Ghia, and in Figures 11(b), 12(b), and 13(b), we have compared our $k' = 1$, $Re = 100$ values for the vertical component of the velocity field along the horizontal center line. Note that our centerline velocity results are roughly independent of the mesh size. Second, note that while our results ostensibly match those of Ghia, there are discernible quantitative differences between the two sets of results even for our finest mesh. To investigate these differences further, we have employed a set of converged pseudospectral results that were obtained via a subtraction method to remove the leading terms of the corner singularities [5]. In Table 8, we have compared our centerline results with these converged results as well as the results of Ghia. Note that our results are much more accurate than the results of Ghia for all mesh sizes and polynomial degrees. Furthermore, our results for $k' = 2$ and $k' = 3$ on a 64×64 element mesh are indistinguishable from the converged pseudospectral results. This attests to the effectiveness of our discretization with increasing k', even in the presence of singularities. We should also again remark that these results were obtained without stretched meshes and without stabilization. We believe that the combination of exact mass conservation and weak enforcement of the no-slip condition plays a pivotal role in the enhanced accuracy of our discretization scheme.

In Figures 14(a), 15(a), and 16(a), we have compared our $k' = 1$, $Re = 400$ values for the horizontal component of the velocity field along the vertical center line with

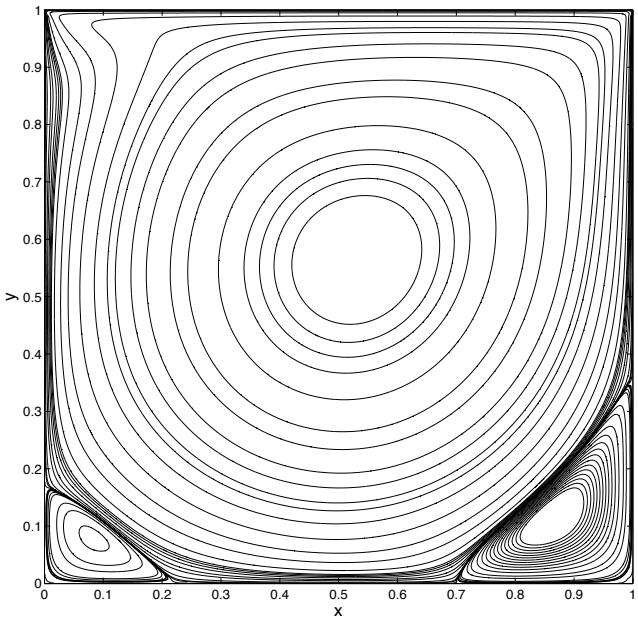

Figure 10: Lid-driven cavity flow: Streamlines for $Re = 1000$.

those of Ghia, and in Figures 14(b), 15(b), and 16(b), we have compared our $k' = 1$, $Re = 400$ values for the vertical component of the velocity field along the horizontal center line. Note that our $Re = 400$ results match the results of Ghia better than the $Re = 100$ results. In fact, our $Re = 400$ results are nearly indistinguishable from the benchmark results on the finest mesh. This is encouraging as the Ghia $Re = 400$ results match well with highly-accurate extrapolated results in the literature [34]. Moreover, our results for the coarsest mesh match the results of Ghia better than any comparable second-order results we have seen in the literature. In Table 8, we have compared our centerline results with the results of Ghia along with our results for $k' = 2$ and $k' = 3$ on a 64×64 element mesh. Note that our results appear to converge quickly with increasing k', despite the increased smoothness of our discrete spaces. By using our $k' = 3$ results as a benchmark, we see our $k' = 1$ results are considerably more accurate than Ghia's results for $h \leq 1/64$. Unfortunately, no pseudospectral results are available to use as comparison.

In Figures 17(a), 18(a), and 19(a), we have compared our $k' = 1$, $Re = 1000$ values for the horizontal component of the velocity field along the vertical center line with those of Ghia, and in Figures 17(b), 18(b), and 19(b), we have compared our $k' = 1$, $Re = 1000$ values for the vertical component of the velocity field along the horizontal center line. This is a more challenging test case than either the $Re = 100$ or $Re = 400$ flows, and the coarse 32×32 element mesh is not nearly fine enough to resolve the flow features. Nonetheless, our results for this coarse mesh better match the results

Table 8: Two-dimensional lid-driven cavity flow: Extrema of the velocity through the centerlines of the cavity.

$Re = 100$

Method	u_{min}	v_{max}	v_{min}
B-spline, $k' = 1$ and $h = 1/32$	-0.21551	0.18054	-0.25472
B-spline, $k' = 1$ and $h = 1/64$	-0.21443	0.17991	-0.25409
B-spline, $k' = 1$ and $h = 1/128$	-0.21414	0.17966	-0.25387
B-spline, $k' = 2$ and $h = 1/64$	-0.21404	0.17957	-0.25379
B-spline, $k' = 3$ and $h = 1/64$	-0.21404	0.17957	-0.25380
Pseudospectral (Ref. [5])	-0.21404	0.17957	-0.25380
Ghia *et al.* (Ref. [21])	-0.21090	0.17527	-0.24533

$Re = 400$

Method	u_{min}	v_{max}	v_{min}
B-spline, $k' = 1$ and $h = 1/32$	-0.33651	0.31039	-0.45768
B-spline, $k' = 1$ and $h = 1/64$	-0.33150	0.30605	-0.45659
B-spline, $k' = 1$ and $h = 1/128$	-0.32989	0.30471	-0.45470
B-spline, $k' = 2$ and $h = 1/64$	-0.32927	0.30415	-0.45406
B-spline, $k' = 3$ and $h = 1/64$	-0.32925	0.30413	-0.45401
Ghia *et al.* (Ref. [21])	-0.32376	0.30203	-0.44993

$Re = 1000$

Method	u_{min}	v_{max}	v_{min}
B-spline, $k' = 1$ and $h = 1/32$	-0.40140	0.39132	-0.54261
B-spline, $k' = 1$ and $h = 1/64$	-0.39399	0.38229	-0.53353
B-spline, $k' = 1$ and $h = 1/128$	-0.39021	0.37856	-0.52884
B-spline, $k' = 2$ and $h = 1/64$	-0.38874	0.37715	-0.52726
B-spline, $k' = 3$ and $h = 1/64$	-0.38857	0.37698	-0.52696
Pseudospectral (Ref. [5])	-0.38857	0.37694	-0.52707
Ghia *et al.* (Ref. [21])	-0.38289	0.37095	-0.51550

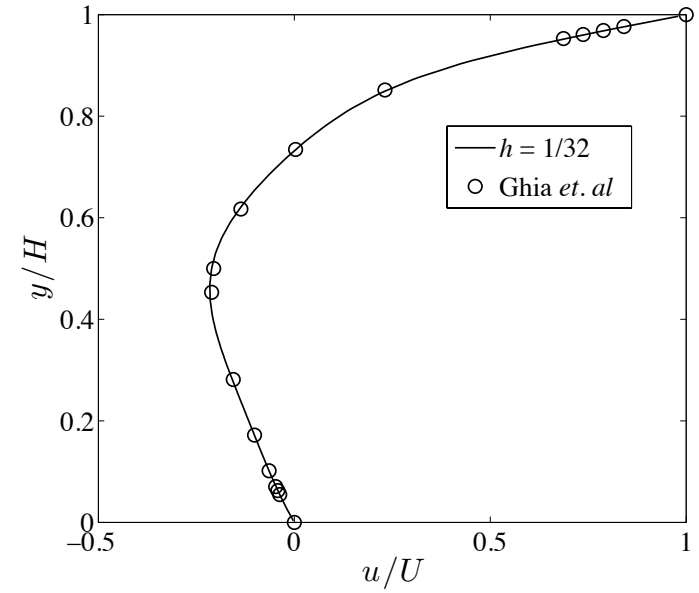

(a)

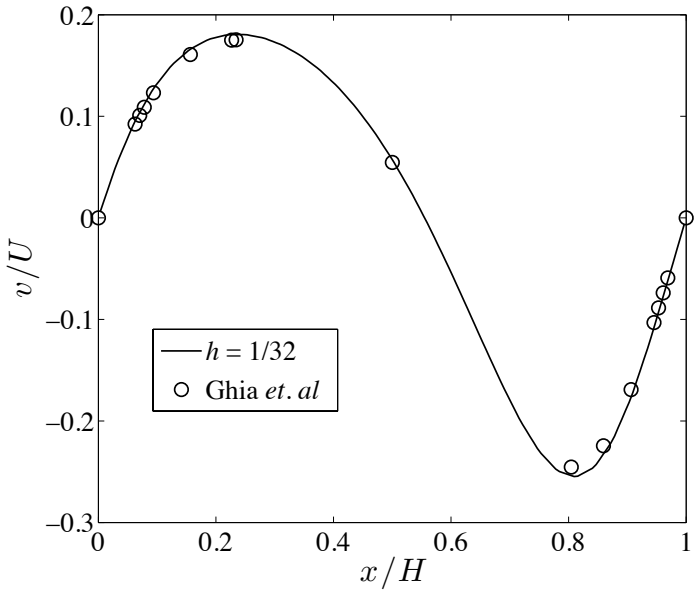

(b)

Figure 11: Lid-driven cavity flow: Velocity field for $k' = 1$, $h = 1/32$, and $Re = 100$. (a) Value of the horizontal component of the velocity field along the vertical center line, (b) Value of the vertical component of the velocity field along the horizontal center line.

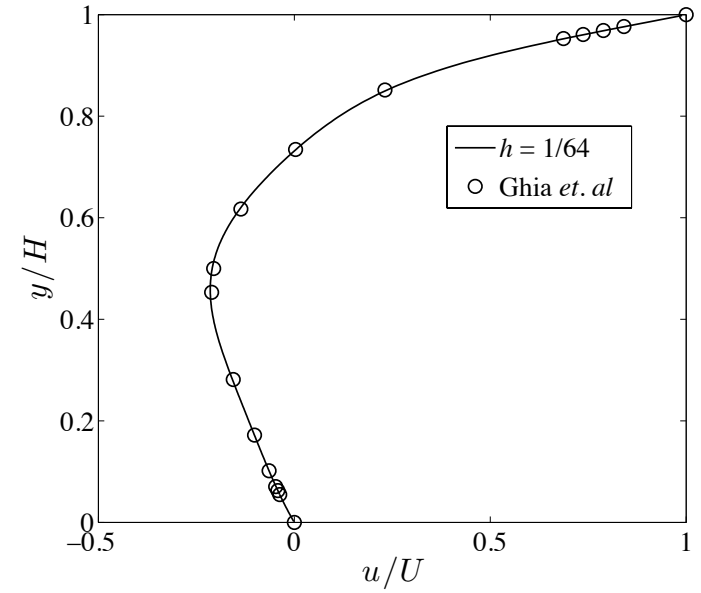

(a)

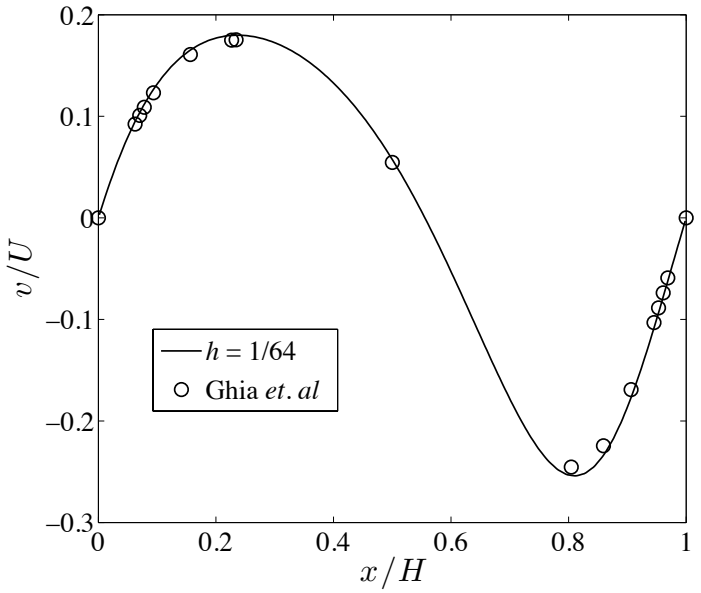

(b)

Figure 12: Lid-driven cavity flow: Velocity field for $k' = 1$, $h = 1/64$, and $Re = 100$. (a) Value of the horizontal component of the velocity field along the vertical center line, (b) Value of the vertical component of the velocity field along the horizontal center line.

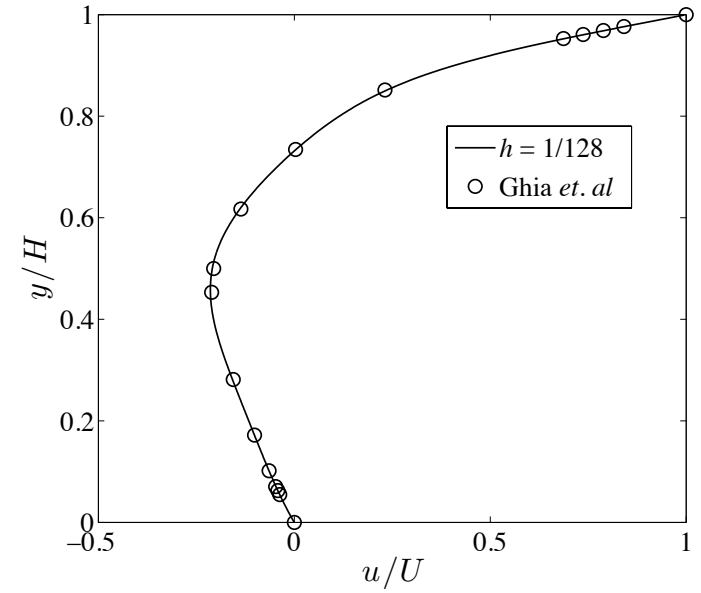

(a)

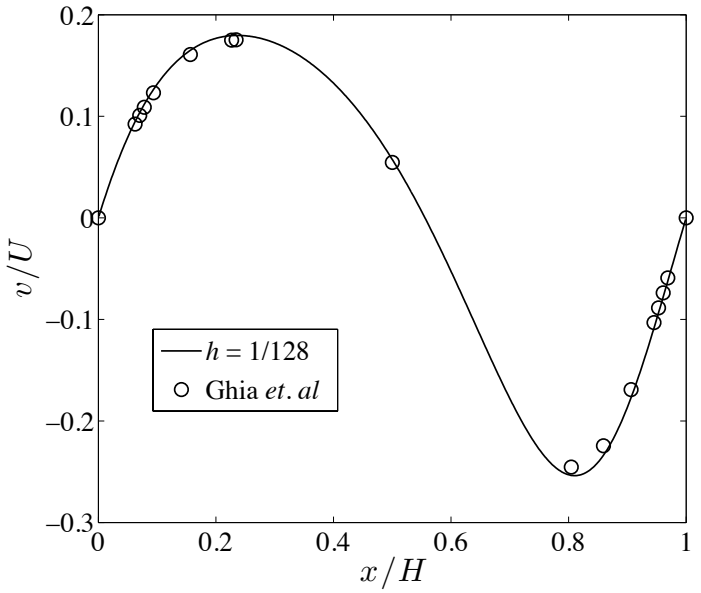

(b)

Figure 13: Lid-driven cavity flow: Velocity field for $k' = 1$, $h = 1/128$, and $Re = 100$. (a) Value of the horizontal component of the velocity field along the vertical center line, (b) Value of the vertical component of the velocity field along the horizontal center line.

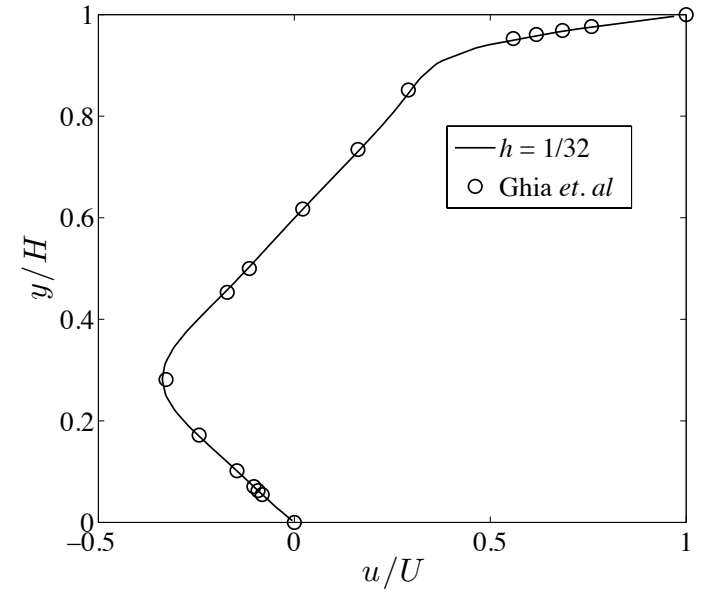

(a)

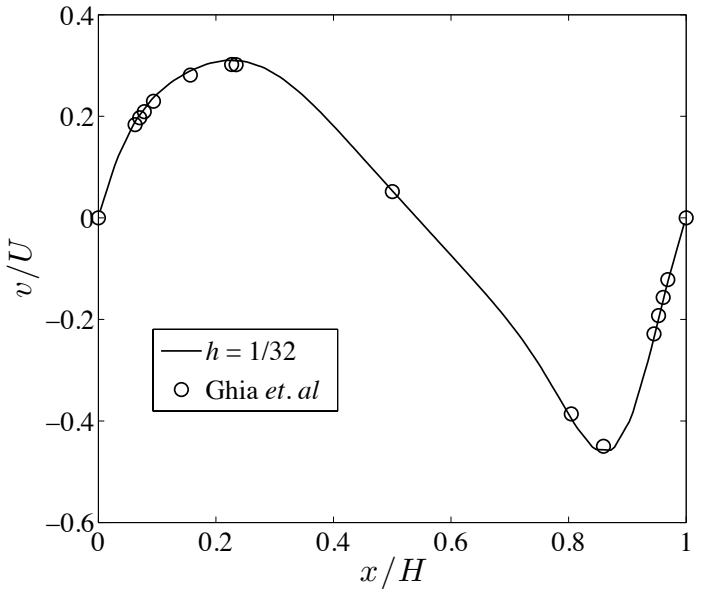

(b)

Figure 14: Lid-driven cavity flow: Velocity field for $k' = 1$, $h = 1/32$, and $Re = 400$. (a) Value of the horizontal component of the velocity field along the vertical center line, (b) Value of the vertical component of the velocity field along the horizontal center line.

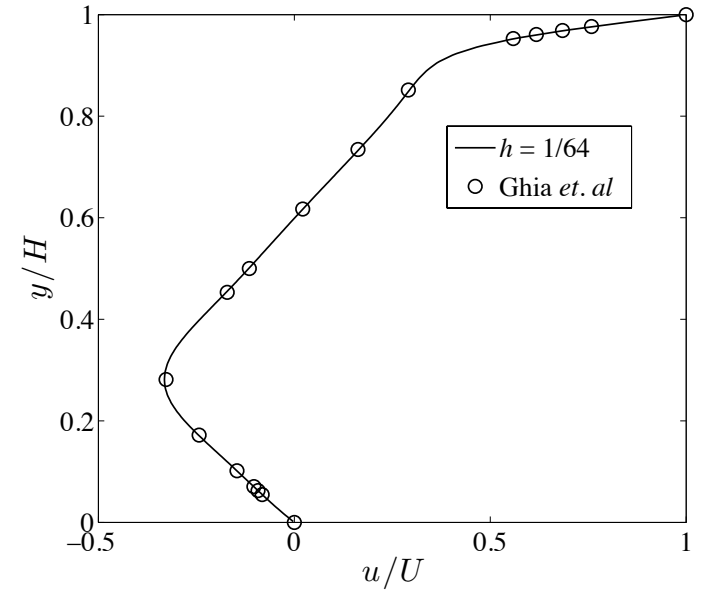

(a)

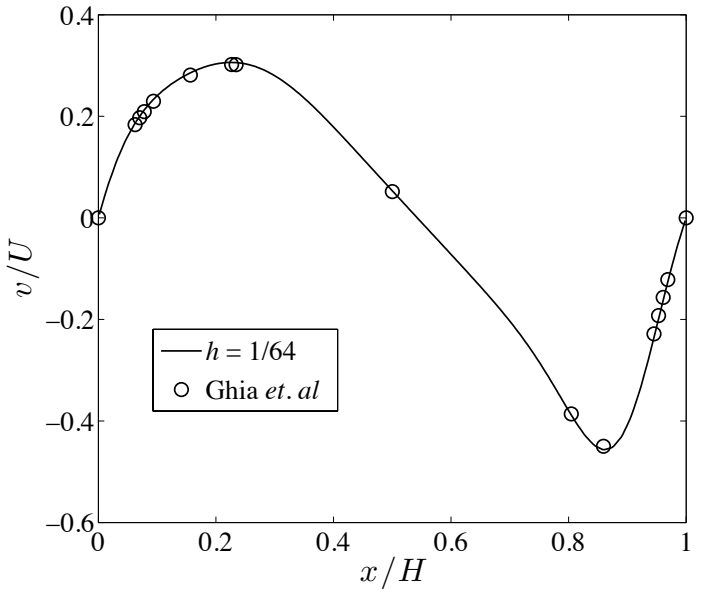

(b)

Figure 15: Lid-driven cavity flow: Velocity field for $k' = 1$, $h = 1/64$, and $Re = 400$. (a) Value of the horizontal component of the velocity field along the vertical center line, (b) Value of the vertical component of the velocity field along the horizontal center line.

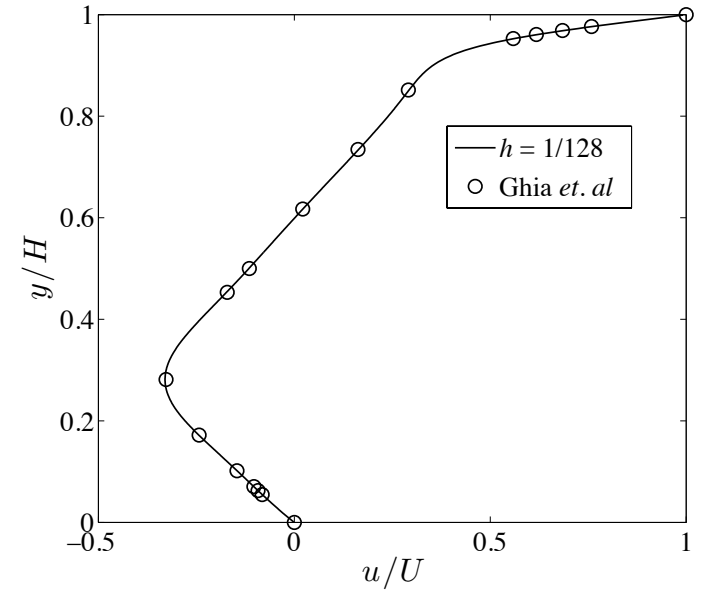

(a)

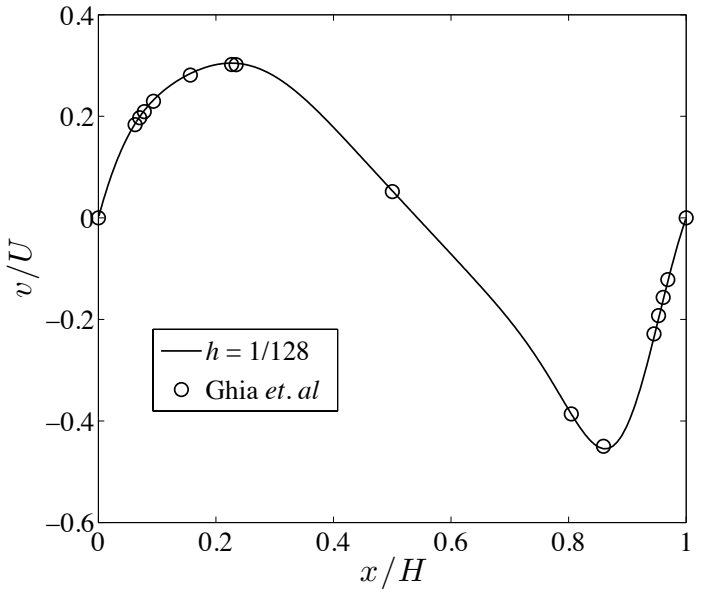

(b)

Figure 16: Lid-driven cavity flow: Velocity field for $k' = 1$, $h = 1/128$, and $Re = 400$. (a) Value of the horizontal component of the velocity field along the vertical center line, (b) Value of the vertical component of the velocity field along the horizontal center line.

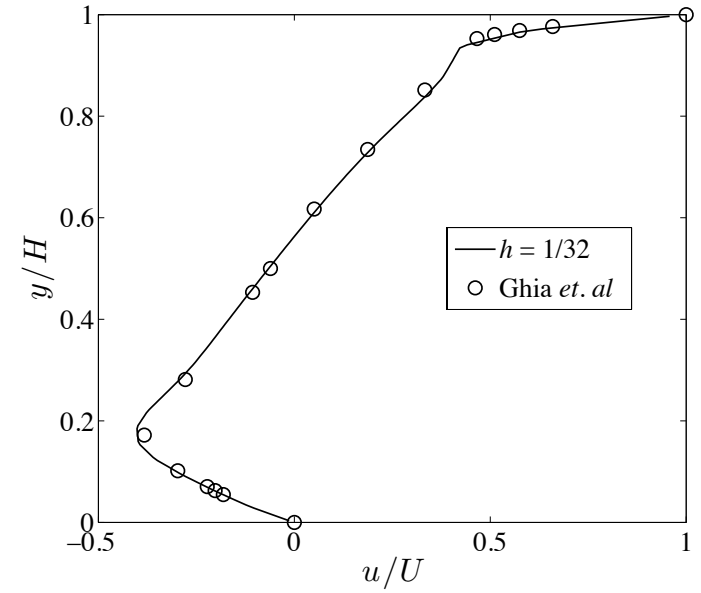

(a)

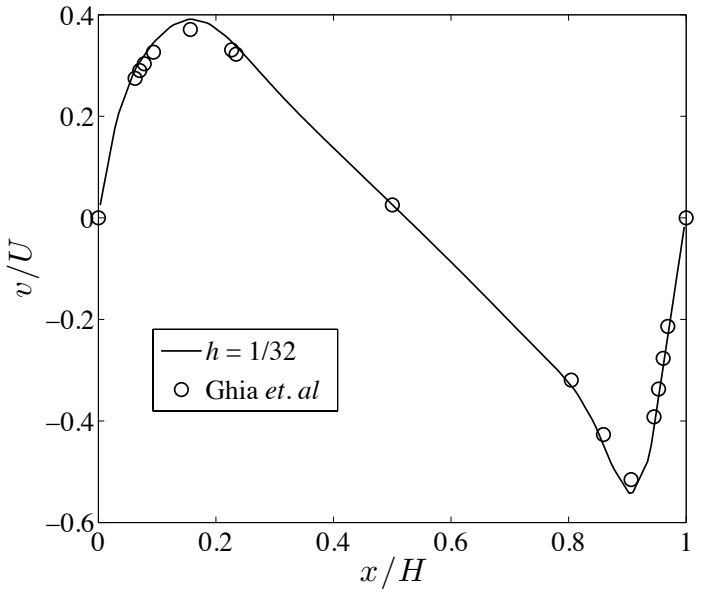

(b)

Figure 17: Lid-driven cavity flow: Velocity field for $k' = 1$, $h = 1/32$, and $Re = 1000$. (a) Value of the horizontal component of the velocity field along the vertical center line, (b) Value of the vertical component of the velocity field along the horizontal center line.

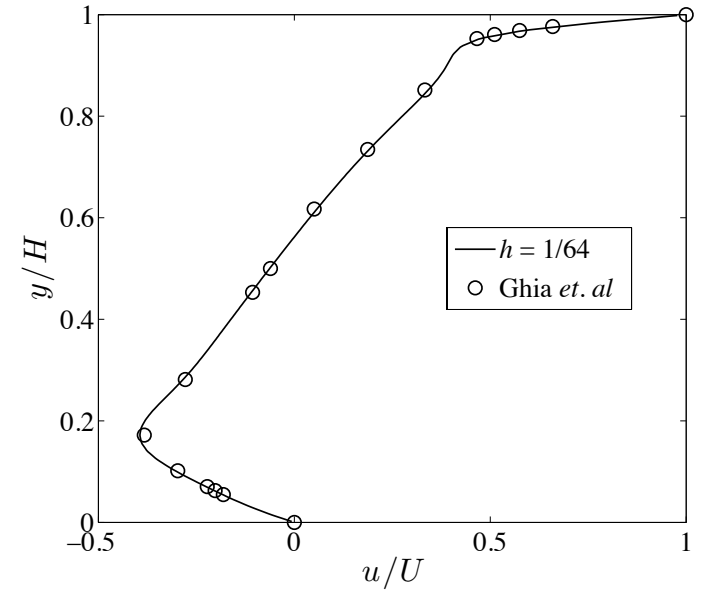

(a)

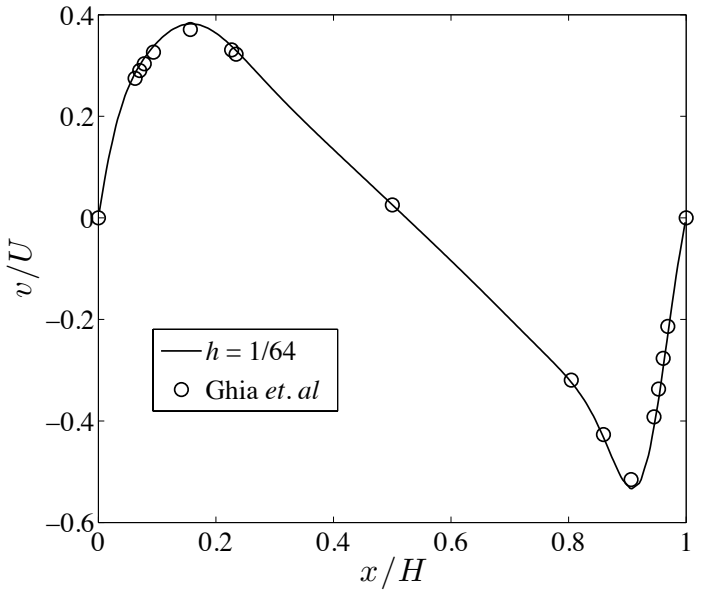

(b)

Figure 18: Lid-driven cavity flow: Velocity field for $k' = 1$, $h = 1/64$, and $Re = 1000$. (a) Value of the horizontal component of the velocity field along the vertical center line, (b) Value of the vertical component of the velocity field along the horizontal center line.

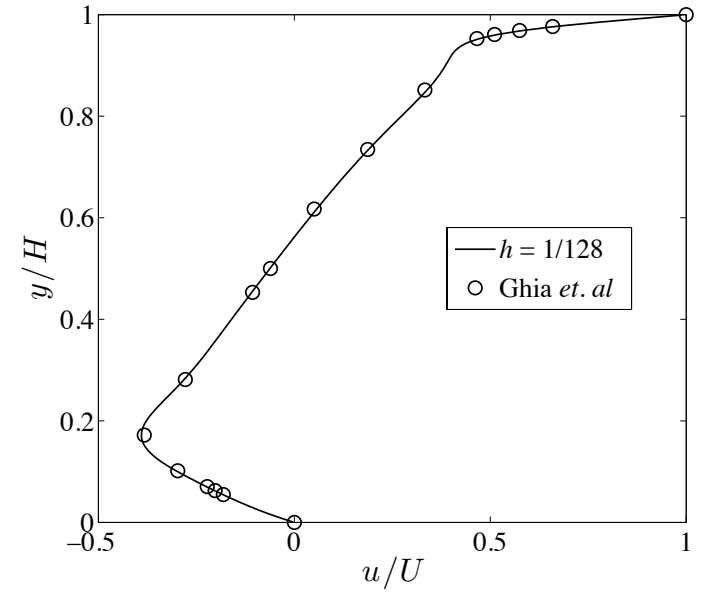

(a)

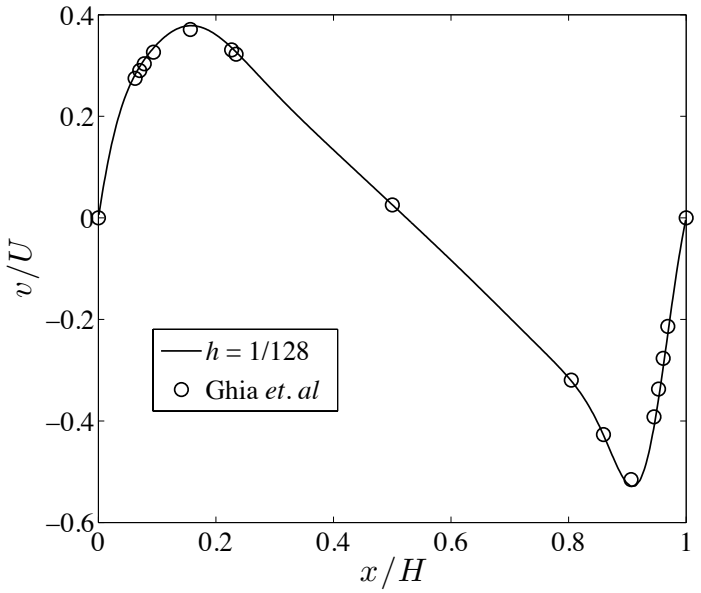

(b)

Figure 19: Lid-driven cavity flow: Velocity field for $k' = 1$, $h = 1/128$, and $Re = 1000$. (a) Value of the horizontal component of the velocity field along the vertical center line, (b) Value of the vertical component of the velocity field along the horizontal center line.

of Ghia than any comparable second-order results we have seen in the literature. Our results for the 64×64 and 128×128 element meshes match Ghia's results even better. In Table 8, we have compared our centerline results with the results of Ghia along with a set of converged pseudospectral results with singularity subtraction [5]. As expected, the results of Ghia are more accurate than our coarse mesh results, but our results for the 64×64 element mesh are comparable in accuracy and our results for the 128×128 element mesh are considerably more accurate. We also computed results for the 64×64 element mesh for polynomial degrees $k' = 2$ and $k' = 3$ and found our results quickly improved with increasing polynomial degree. Indeed, our results for $k' = 3$ are nearly indistinguishable from the converged pseudospectral results.

To compute all of these flow examples, we utilized the Newton-Raphson method in conjunction with continuation. Specifically, for the $Re = 100$ simulations, we employed Newton-Raphson using the results of a corresponding Stokes simulation as an initial guess. For the $Re = 400$ simulations, we employed Newton-Raphson using the results of the $Re = 100$ simulations as an initial guess, and so on. We found a maximum of four Newton-Raphson steps were required to achieve a sufficiently accurate solution for each nonlinear solve. Using this procedure, we have been able to successfully simulate flows upwards of $Re = 3200$ on relatively coarse meshes. We have also been able to reproduce all of the results presented here by a more expensive dynamic approach in which the solution is evolved from an initial condition by the unsteady Navier-Stokes equations.

9.2 Confined Jet Impingement

Impinging jets are commonly used in engineering applications due to their enhanced heat and mass transfer characteristics. Impinging jets even occur in blood vessels and are believed to play a role in atherogenesis [20]. Many discretization schemes yield a velocity field with spurious nonzero divergence when applied to the simulation of incompressible jet impingement, even at small and moderate Reynolds numbers. As our proposed discretization satisfies the divergence-free constraint exactly, it does not suffer from this non-physical behavior.

The physical problem of confined jet impingement is illustrated in Figure 20. Fluid flows from one pipe into a second pipe lying perpendicular to the first. To simulate this flow, we use a two-dimensional mathematical idealization which is illustrated in Figure 21. Along the left hand side of the domain, a symmetry condition is applied as we only model half of the jet system. Along the bottom side of the domain, no-slip and no-penetration boundary conditions are enforced. Along the top side of the domain, two different sets of boundary conditions are applied. Along the first $D/2$ length of the top side, an inflow boundary condition is applied. Along the remainder of the top side, no-slip and no-penetration boundary conditions are enforced. Along the right hand side of the domain, a zero-traction boundary condition is enforced. The height of the domain is set as H, and the length of the domain, L, is chosen long

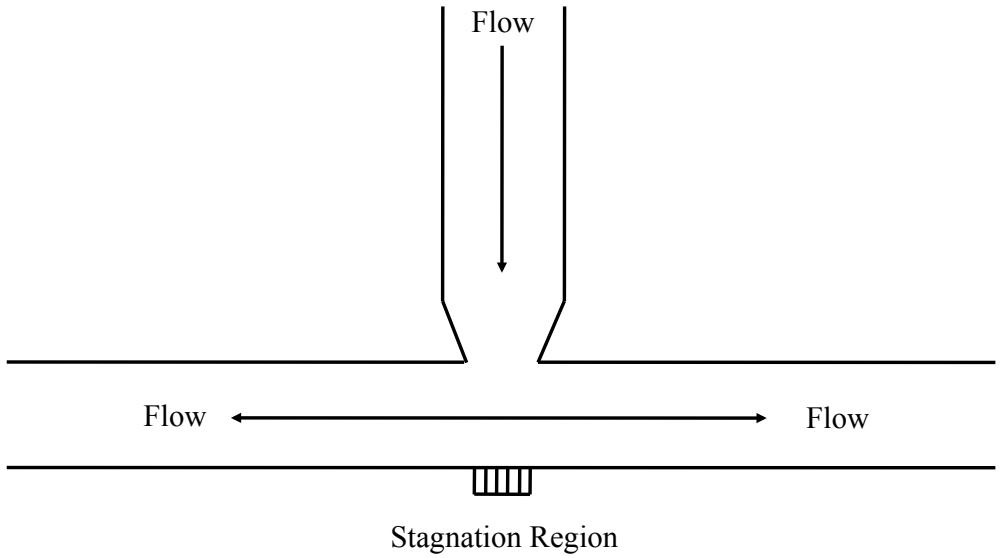

Figure 20: Confined jet impingement: Physical setup.

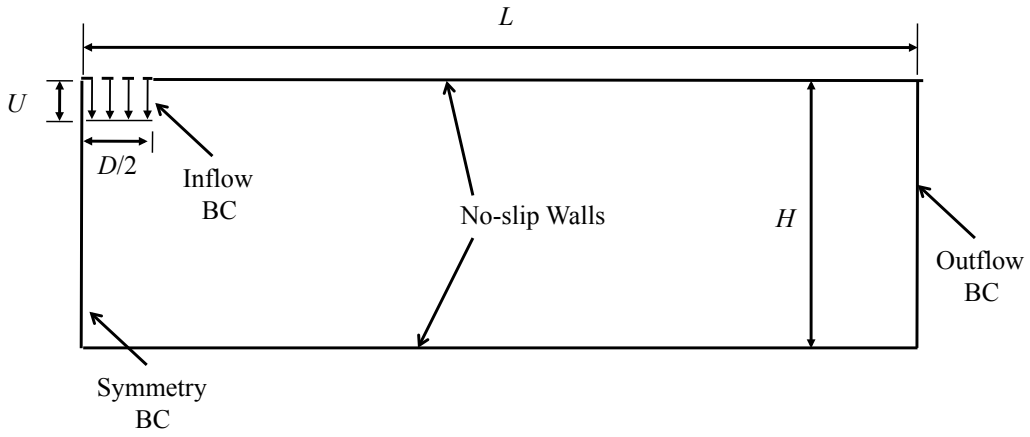

Figure 21: Confined jet impingement: Model problem description.

enough such that the flow exiting the pipe is parallel to the outflow plane. For the computations here, $D = H = 1$ and $L = 8$. The inflow speed is set to be $U = 1$. The Reynolds number for the flow is defined as $Re = UH/\nu$.

We have simulated $Re = 50$ confined jet impingement for two divergence-conforming B-spline discretizations of polynomial degree $k' = 1$ corresponding to mesh lengths of $h = 1/16$ and $h = 1/32$. The resulting velocity fields are plotted in Figures 22 and 23. First, note that the computed streamlines for the two meshes are indistinguishable. Second, note that the velocity fields are smooth and free from spurious oscillations. To compare our simulation results with those of a classical mixed method, we have simulated the impingement problem for a conservative Taylor-Hood finite element discretization with mesh length $h = 1/8$. This discretization contains approximately the same number of velocity degrees of freedom as the preceding coarse B-spline discretization. The velocity field resulting from the Taylor-Hood discretization is plotted in Figure 24. Note that the contours of the velocity field roughly match the velocity contours resulting from the divergence-conforming B-spline discretizations. However, the velocity field resulting from the Taylor-Hood discretization exhibits significant non-physical compressibility. We have conducted numerical investigations of confined jet impingement at other Reynolds numbers and obtained similar results to those reported here.

10 Conclusions

In this paper, divergence-conforming B-spline discretizations have been presented for the steady Navier-Stokes equations utilizing a variational formulation written in conservation form. Tangential velocity boundary conditions are implemented weakly using Nitsche's method. The formulation yields velocity fields that are pointwise divergence-free on general mapped geometries. A collection of stability and error estimates have been derived for flows subject to a smallness condition, and these theoretical results have been confirmed and supplemented by numerical simulations of problems with known analytical solutions. In fact, these numerical simulations have revealed that the proposed discretizations are robust with respect to Reynolds number, a property not shared by classical finite elements such as the Taylor-Hood element. The new discretizations have also been applied to a selection of benchmark problems where the advantages of the new methodology over classical methods have been highlighted. In future work, we plan to extend the present developments to the unsteady Navier-Stokes equations and generalize to locally-refined meshes.

Acknowledgements

We thank Annalisa Buffa and Giancarlo Sangalli for their useful discussions regarding this work. The authors were partially supported by the Office of Naval Research under

contract number N00014-08-0992. John A. Evans was additionally partially supported by the Department of Energy Computational Science Graduate Fellowship, provided under grant number DE-FG02-97ER25308. This support is gratefully acknowledged.

References

[1] D N Arnold. An interior penalty finite element method with discontinuous elements. *SIAM Journal on Numerical Analysis*, 19:742–760, 1979.

[2] Y Bazilevs and T J R Hughes. Weak imposition of Dirichlet boundary conditions in fluid mechanics. *Computers and Fluids*, 36:12–26, 2007.

[3] Y Bazilevs, C M Michler, V M Calo, and T J R Hughes. Weak Dirichlet boundary conditions for wall-bounded turbulent flows. *Computer Methods in Applied Mechanics and Engineering*, 196:4853–4862, 2007.

[4] Y Bazilevs, C M Michler, V M Calo, and T J R Hughes. Isogeometric variational multiscale modeling of wall-bounded turbulent flows with weakly-enforced boundary conditions on unstretched meshes. *Computer Methods in Applied Mechanics and Engineering*, 199:780–790, 2010.

[5] O Botella and R Peyret. Benchmark spectral results on the lid-driven cavity flow. *Computers and Fluids*, 27:421–433, 1998.

[6] S C Brenner. Korn's inequalities for piecewise H^1 vector fields. *Mathematics of Computation*, 73:1067–1087, 2003.

[7] A.N. Brooks and T.J.R. Hughes. Streamline upwind/Petrov-Galerkin formulations for convection dominated flows with particular emphasis on the incompressible Navier-Stokes equations. *Computer Methods in Applied Mechanics and Engineering*, 32:199–259, 1982.

[8] A Buffa, C de Falco, and R Vázquez. Isogeometric analysis: Stable elements for the 2D Stokes equation. *International Journal for Numerical Methods in Fluids*, 65:1407–1422,20–30, 2011.

[9] A Buffa, J Rivas, G Sangalli, and R Vázquez. Isogeometric discrete differential forms in three dimensions. *SIAM Journal on Numerical Analysis*, 49:818–844, 2011.

[10] A Buffa, G Sangalli, and R Vázquez. Isogeometric analysis in electromagnetics: B-splines approximation. *Computer Methods in Applied Mechanics and Engineering*, 199:1143–1152, 2010.

[11] B Cockburn, G Kanschat, and D Schötzau. A locally conservative LDG method for the incompressible Navier-Stokes equations. *Mathematics of Computation*, 74:1067–1095, 2004.

[12] B Cockburn, G Kanschat, and D Schötzau. A note on discontinuous Galerkin divergence-free solutions of the Navier-Stokes equations. *SIAM Journal on Scientific Computing*, 31:61–73, 2007.

[13] J A Cottrell, T J R Hughes, and Y Bazilevs. *Isogeometric Analysis: Toward Integration of CAD and FEA*. Wiley, 2009.

[14] C R de Boor. *A Practical Guide to Splines*. Springer-Verlag, 1978.

[15] J Douglas and T Dupont. Interior Penalty Procedures for Elliptic and Parabolic Galerkin Methods. *Lecture Notes in Physics*, 58, 1976.

[16] J A Evans. *Divergence-free B-spline Discretizations for Viscous Incompressible Flows*. PhD thesis, The University of Texas at Austin, 2011.

[17] J A Evans, Y Bazilevs, I Babuška, and T J R Hughes. n-widths, sup-infs, and optimality ratios for the k-version of the isogeometric finite element method. *Computer Methods in Applied Mechanics and Engineering*, 198:1726–1741, 2009.

[18] J A Evans and T J R Hughes. Explicit trace inequalities for isogeometric analysis and parametric finite elements. Technical report, ICES Report 11-17, 2011.

[19] J A Evans and T J R Hughes. Isogeometric divergence-conforming B-splines for the Darcy-Stokes-Brinkman equations. Technical report, ICES Report 12-03, 2012.

[20] D L Fry. Atherogenesis: Initiating factors. *CIBA Foundation Symposium*, 12:93–125, 1973.

[21] U Ghia, K N Ghia, and C T Shin. High-Re solutions for incompressible flow using the Navier-Stokes equations and a multigrid method. *Journal of Computational Physics*, 48:387–411, 1982.

[22] V Girault and P A Raviart. *Finite Element Methods for Navier-Stokes Equations. Theory and Algorithms*. Springer-Verlag, 1986.

[23] K Höllig. *Finite Element Methods with B-splines*. Society for Industrial and Applied Mathematics, 2003.

[24] P Hood and C Taylor. Navier-Stokes equations using mixed interpolation. In J T Oden, R H Gallagher, O C Zienkiewicz, and C Taylor, editors, *Finite Element Methods in Flow Problems*, pages 121–132. University of Alabama in Huntsville Press, 1974.

[25] T J R Hughes, L P Franca, and M Balestra. A new finite element formulation for computational fluid dynamics: V. Circumventing the Babuška-Brezzi condition: A stable Petrov-Galerkin formulation of the Stokes problem accomodating equal-order interpolations. *Computer Methods in Applied Mechanics and Engineering*, 59:85–99, 1986.

[26] T J R Hughes and G N Wells. Conservation properties for the Galerkin and stabilised forms of the advection-diffusion and incompressible Navier-Stokes equations. *Computer Methods in Applied Mechanics and Engineering*, 194:1141–1159, 2005.

[27] L I G Kovasznay. Laminar flow behind a two-dimensional grid. *Mathematical Proceedings of the Cambridge Philosophical Society*, 44:58–62, 1948.

[28] R J Labeur and G N Wells. Energy stable and momentum conserving hybrid finite element method for the incompressible Navier-Stokes equations. *SIAM Journal on Scientific Computing*. To appear.

[29] N C Nguyen, J Peraire, and B Cockburn. An implicit high-order hybridizable discontinuous Galerkin method for the incompressible Navier-Stokes equations. *Journal of Computational Physics*, 230:1147–1170, 2011.

[30] J A Nitsche. Über ein Variationspringzip zur Lösung von Dirichlet-Problemem bei Verwendung von Teilräumen, die keinen Randbedingungen unterworfen sind. *Abhandlungen aus dem Mathematischen Seminar der Universit at Hamburg*, 36:9–15, 1971.

[31] S B Pope. *Turbulent Flows*. Cambridge University Press, 2003.

[32] P A Raviart and J M Thomas. A mixed finite element method for second order elliptic problems. *Lecture Notes in Mathematics*, 606:292–315, 1977.

[33] H-G Roos, M Stynes, and L Tobiska. *Numerical Methods for Singularly Perturbed Differential Equations. Convection-Diffusion and Flow Problems*. Springer, 1996.

[34] R Schreiber and H B Keller. Driven cavity flows by efficient numerical techniques. *Journal of Computational Physics*, 49:310–333, 1983.

[35] L L Schumaker. *Spline functions: Basic theory*. Cambridge Mathematical Library, Cambridge University Press, 2007.

[36] D B Spalding. A single formula for the law of the wall. *Journal of Applied Mechanics*, 28:444–458, 1961.

[37] T E Tezduyar, M Behr, S Mittal, and J Liou. A new strategy for finite element computations involving moving boundaries and interfaces - The deforming-spatial-domain/space-time procedure: II. Computation of free-surface flows, two-liquid flows, and flows with drifting cylinders. *Computer Methods in Applied Mechanics and Engineering*, 94:353–371, 1992.

[38] H Triebel. *Interpolation Theory, Function Spaces, Differential Operators, Second Edition*. Johann Ambrosius Barth, 1995.

[39] M F Wheeler. An elliptic collocation-finite element method with interior penalties. *SIAM Journal on Numerical Analysis*, 15:152–161, 1978.

[40] T A Zang. On the rotation and skew-symmetric forms for incompressible flow simulations. *Applied Numerical Mathematics*, 7:27–40, 1991.

[41] S Zhang. A new family of stable mixed finite elements for 3D Stokes equations. *Mathematics of Computation*, 250:543–554, 2005.

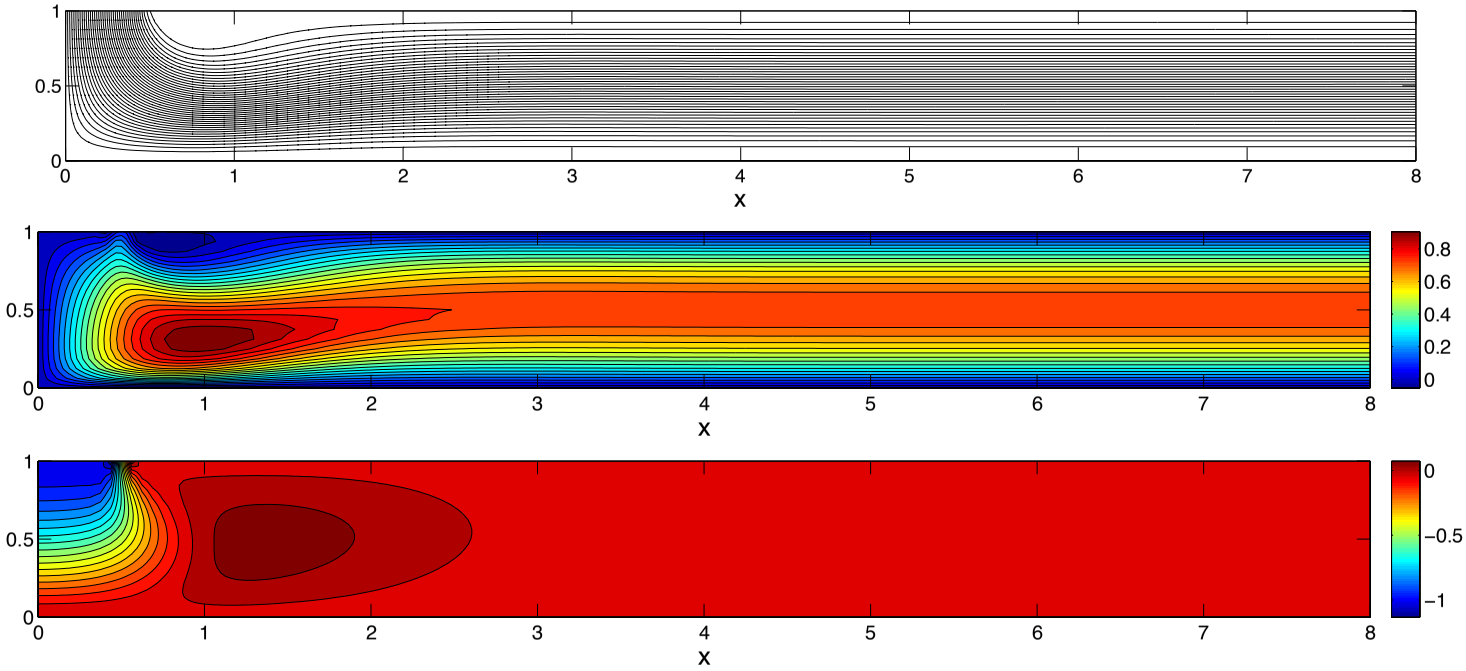

Figure 22: Confined jet impingement at $Re = 50$: Results for a coarse mesh. Top: Streamlines; Middle: Contours of u_1; Bottom: Contours of u_2.

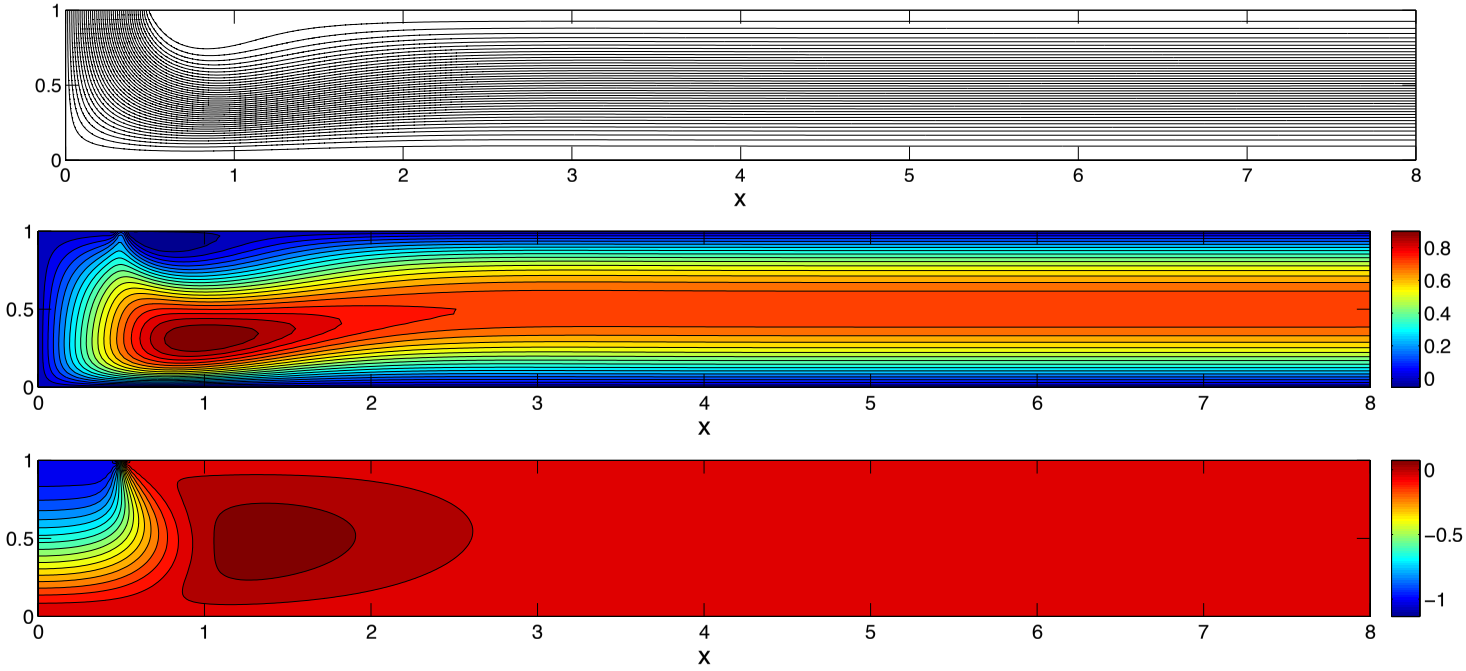

Figure 23: Confined jet impingement at $Re = 50$: Results for a resolved mesh. Top: Streamlines; Middle: Contours of u_1; Bottom: Contours of u_2.

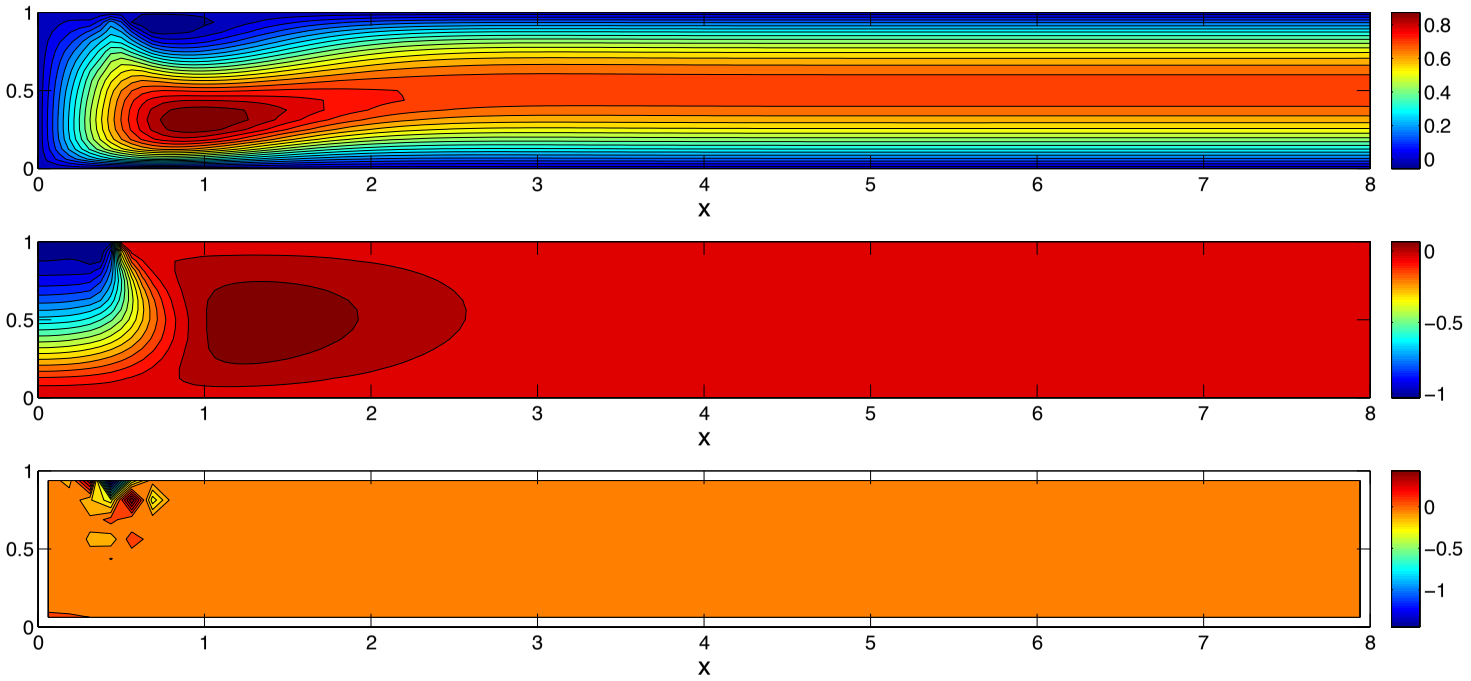

Figure 24: Confined jet impingement at $Re = 50$: Results for $\mathbf{Q}_2/Q_1$ velocity/pressure pair, $h = 1/8$. Top: Contours of u_1; Middle: Contours of u_2; Bottom: Divergence of velocity field (interpolated at element centers).